論文 / 著書情報
Article / Book Information

題目(和文)	
Title(English)	How much data rate is needed in V2X communications to ensure safe automated driving by cooperative perception
著者(和文)	深津龍一
Author(English)	Ryuichi Fukatsu
出典(和文)	学位:博士（工学）, 学位授与機関:東京工業大学, 報告番号:甲第11752号, 授与年月日:2022年3月26日, 学位の種別:課程博士, 審査員:阪口 啓,髙田 潤一,藤井 輝也,TRAN GIA KHANH,西尾 理志,村井 英志
Citation(English)	Degree:Doctor (Engineering), Conferring organization: Tokyo Institute of Technology, Report number:甲第11752号, Conferred date:2022/3/26, Degree Type:Course doctor, Examiner:,,,,,
学位種別(和文)	博士論文
Type(English)	Doctoral Thesis

Tokyo Institute of Technology School of Engineering
Department of Electrical and Electronic Engineering

Doctoral thesis

How much data rate is needed in V2X communications to ensure safe automated driving by cooperative perception

Supervisor Kei Sakaguchi Professor

Feb. 2022

Submitter

Name Ryuichi Fukatsu

Contents

Chapter 1

Introduction

1.1 Background

Vehicles play a key role in modern transportation systems and are indispensable in our daily life. Market research predicts a continuous growth of ownership rate of vehicles in the coming years, especially in developing countries. However, as a vehicle penetration rate increases, various social issues arise. Traffic accidents are one of the typical issues. It is said that 93% of traffic accidents are caused by human failure in the United States of America [1]. In Japan, it is reported that more than half of traffic fatalities are caused by violating the responsibility of safe driving, which deeply relates to human failure [2]. Moreover, it also says that more than half of victims are senior citizens. World Health Organization (WHO) also publishes key facts about road injuries [3]. The following items show important facts.

- Road traffic crashes cost most countries 3% of their gross domestic product.
- 93% of the world's fatalities on the roads occur in low- and middle-income countries, even though these countries have approximately 60% of the world's vehicles.
- Road traffic injuries are the leading cause of death for children and young adults aged 5-29 years.

It also mentions risk factors such as high-speed driving, driving under alcohol or other psychoactive substances, distracted driving, which is mainly due to drivers. To summarize these statistics and facts, it shows that human failure during driving often leads to traffic fatalities and economic loss. Lack of public transport for senior citizens in a rural area is also a typical social problem. In Japan, the service frequency of public transport gets halved after the elapse of 30 years [4]. Since a lack of drivers causes this problem, it is a severe problem in an aging society. Considering these facts, automated vehicles are expected to make car traffic safer because they are free from human failure and do not need human drivers in any area.

Current works in Japan are automated driving trials that are performed to realize level 2 and 3 automated driving defined by Society of Automotive Engineers (SAE) [5]. For example, Honda Motor company develops level 3 automated driving vehicles. This vehicle switches to automated driving when there are traffic jams on a highway. Another example is level 2 automated driving buses in Ibaraki prefecture. These automated driving buses are

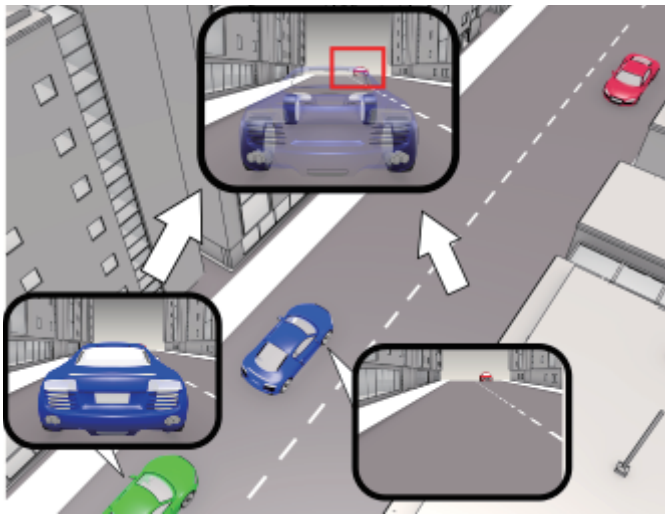

Figure 1.1: The concept of cooperative perception. Although the red oncoming vehicle is invisible from the green ego vehicle due to the blue blocking vehicle, cooperative perception between the ego vehicle and blocking vehicle changes it visible.

proposed to solve a lack of transportation in rural areas and are programmed to drive along a fixed path. In the United States of America, United States Department Of Transportation (USDOT) establishes a consistent approach to shaping policy for automated driving vehicles, based on the following six principles [6]. The six principles are prioritizing safety, remaining technology neutral, modernizing regulations, encouraging a consistent regulatory and operational environment, preparing actively for automation, and protecting and enhancing the freedoms enjoyed by Americans. Several National Highway Traffic Safety Administration (NHTSA) safety standards for motor vehicles assume a human occupant such as seating arrangements and the use of steering wheels, brakes, and accelerator pedals. However, some level 4 and 5 automated driving systems may be designed to be entirely controlled by the system and may not be equipped with human-machine interfaces such as brakes, which does not assume a human driver. Therefore, NHTSA starts to reconsider its current standards. USDOT also focuses on Vehicle-to-everything (V2X) communications because it will be an important complementary technology. Although V2X communications are expected, USDOT shows a cautious stance that V2X communications cannot be a precondition to the development of automated driving vehicles.

To realize the high level of automated driving, the concept called connected car society is planned. It is designed to connect vehicles to networks so that new services will be started and more advanced automated driving will be realized. The new services can be classified into four groups such as safety, car life support, agent, and infotainment. Among these services, this thesis focused on the cooperative or collective perception that is one of the applications of the safety service to improve the safety of automated driving. Cooperative perception is a technology that a vehicle can use sensor data obtained from other vehicles or Road

Side Units (RSUs) through wireless communications as shown in Fig. 1.1. The effect of cooperative perception comes from obtaining sensor data of other perspectives so that the receiving vehicle can see through blind spots. In other words, since dynamic maps that are used for navigation and avoiding obstacles of automated driving are made from sensor data, cooperative perception can be regarded as integrating dynamic maps, which will lead to a higher quality of automated driving.

There are two ways to realize cooperative perception that are sharing processed or raw sensor data. Processed sensor data includes information about recognized objects such as category and location. The main advantage of sharing processed sensor data is that complex processes such as object recognition can be performed in application servers and high performance of wireless communications is not required. On the other hand, when raw sensor data is shared, the receiving vehicle performs a recognition process in its system so that recognition results are free from errors due to the sender. Moreover, the receiving vehicle can use the sensor data without information loss. In order to guarantee safe automated driving by cooperative perception, it is important to clarify the shared amount of processed or raw sensor data rate for safe automated driving. For example, in [7], it publishes the requirements for sharing both processed and raw sensor data. On the other hand, in [8], it does not consider sharing raw sensor data due to the necessity of a large data rate.

1.2 Related works

This section summarizes the related works about V2X communications for cooperative perception and the details of each work are introduced in the corresponding section. The related works are classified into three categories. The first category is the derivation of the requirements for cooperative perception applications. These works analyze the requirements for the cooperative perception, or collective perception, applications through simulation or calculation [7, 8, 9, 10, 11, 12]. Their analysis of the requirements is based on sharing processed or raw sensor data, and the calculation is based on the sum of the output of installed automotive sensors. Since sharing processed sensor data is appropriate for the current V2X communications, the analysis based on sharing processed sensor data is discussed under a specific format. On the other hand, the analysis based on sharing raw sensor data is not as abundant as sharing processed sensor data.

The second category is the analysis through the demonstration of cooperative perception sharing processed sensor data. These works perform cooperative perception with processed sensor data and analyze the communication performance and the recognition results [13, 14, 15, 16]. The third category is the analysis through the demonstration of cooperative perception sharing raw sensor data. These works analyze the communication performance during the demonstration of sharing raw sensor data [17, 18, 19]. However, the works of the second and the third category do not discuss the relation between safety and communication performance.

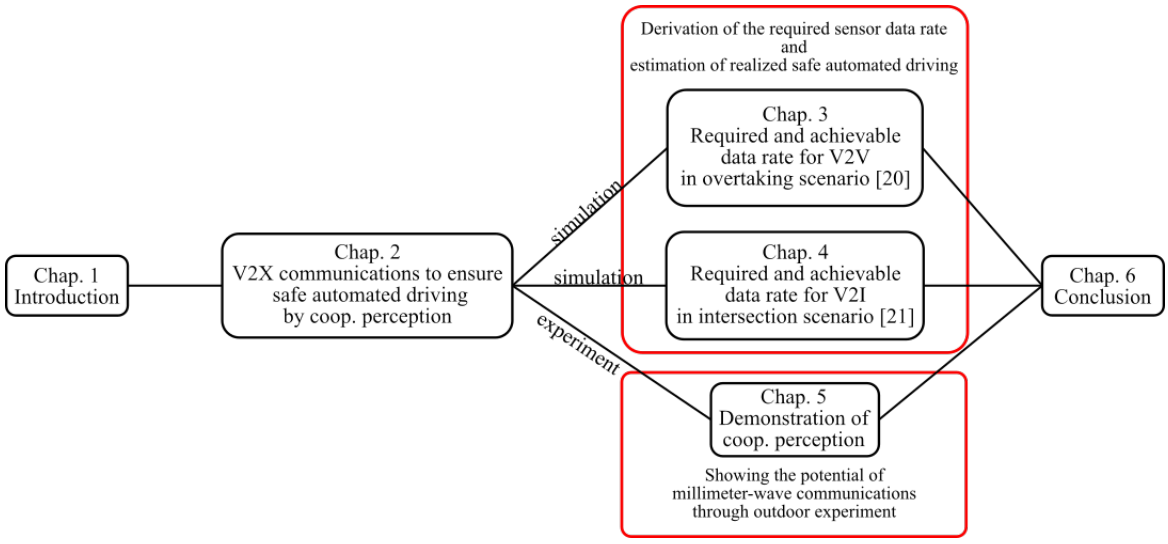

Figure 1.2: The structure and the brief contributions of this thesis.

1.3 Thesis contributions

Since the requirements for cooperative perception applications are needed, this thesis tackles the derivation of the requirements for safe automated driving with cooperative perception. It attempts to derive the requirements by comprehensive analysis that is not performed by the current researches and shows the requirements under fundamental driving scenarios. The contribution of this paper consists of two aspects [20, 21]. The first aspect is the derivation of the sensor data rate required for safe automated driving. This derivation is based on considering the minimum required braking to alleviate traffic congestion and the recognition process. There are some works that analyze the requirements for cooperative perception or safe driving, but their discussions are closed in one discipline such as wireless communication or automotive control. This thesis analyzes the requirements under multidiscipline such as vehicle behavior, recognition process, and wireless communications to derive the realistic requirements. Moreover, the derivation is divided into cases where cooperative perception is used and not used. The format of how to send sensor data in cooperative perception is assumed to send raw sensor data. Although sharing raw sensor data requires much larger communication resources than sharing processed sensor data, sharing raw sensor data is necessary to develop level 4 and 5 automated driving vehicles. The necessities come from liability reasons at car accidents, distributed verification of local and remote sensor data, and generating accurate maps, which cannot be achieved by sharing processed sensor data. Therefore, our derived requirements are not only realistic but also useful to realize high-level automated driving.

The second aspect is the discussion of the ability of millimeter-wave communications for safe automated driving. Since performing cooperative perception by sharing raw sensor data requires a large number of communication resources, millimeter-wave communications that have larger channel capacity than the conventional V2X communications are expected to have a great synergy with sharing raw sensor data. In order to prove this expectation, this thesis

compares the safe automated driving realized by the conventional and the millimeter-wave V2X communications, and the results show the potential of millimeter-wave V2X communications.

1.4 Thesis structure

The rest of this paper is organized as shown in Fig. 1.2. Chapter 2 introduces related technologies such as dynamic maps and cooperative perception and shows related works about the requirements for cooperative perception. Moreover, it shows the current V2X communications and the next generation of V2X communications that are necessary to realize cooperative perception. It also introduces the current idea about safe driving and selects scenarios to analyze safe automated driving. Chapter 3 and 4 derive the required sensor data rate for safe automated driving and discuss the realized safe automated driving by the conventional and the millimeter-wave V2X communications. Chapter 5 shows the demonstration of cooperative perception using millimeter-wave Vehicle-to-Infrastructure (V2I) communications. Chapter 6 concludes this paper.

Chapter 2

V2X communications to ensure safe automated driving by cooperative perception

2.1 Taxonomy of driving automation

Before starting the discussion and the analysis, this section introduces the category of driving automation. The category of driving automation can be roughly classified into driving support and automated driving. Dynamic Driving Task (DDT) and Operational Design Domain (ODD) are key factors to explain the difference between driving support and automated driving. DDT describes all of the real-time operational and tactical functions required to operate a vehicle in on-road traffic. In other words, operational functions include basic vehicle motion control and tactical functions include planning and execution for event/object avoidance. ODD describes operating conditions under which a given driving automation system is designed to function, including, for example, environmental, geographical, and time-of-day restrictions. Fig. 2.1 shows the definition of each level of automated driving, and it is based on the following five points [5].

- Whether the driving automation system performs either the longitudinal or the lateral vehicle motion control subtask of DDT.
- Whether the driving automation system performs both the longitudinal and the lateral vehicle motion control subtasks of the DDT simultaneously.
- Whether the driving automation system also performs the OEDR subtask of the DDT.
- Whether the driving automation system also performs DDT fallback.
- Whether the driving automation system is limited by an ODD.

From level 3, driving automation is regarded as automated driving.

From more than level 2, the driving automation system mainly controls the entire DDT, but the driver is expected to take over the DDT in emergency cases at level 3. Moreover, different conditions are imposed on ODD among automated driving levels. Automated driving

SAE level	Name	Narrative Definition	Execution of Steering and Acceleration/ Deceleration	*Monitoring* of Driving Environment	Fallback Performance of *Dynamic Driving Task*	System Capability *(Driving Modes)*
***Human driver* monitors the driving environment**						
0	**No Automation**	the full-time performance by the *human driver* of all aspects of the *dynamic driving task*, even when enhanced by warning or intervention systems	Human driver	Human driver	Human driver	n/a
1	**Driver Assistance**	the *driving mode*-specific execution by a driver assistance system of either steering or acceleration/deceleration using information about the driving environment and with the expectation that the *human driver* perform all remaining aspects of the *dynamic driving task*	Human driver and system	Human driver	Human driver	Some driving modes
2	**Partial Automation**	the *driving mode*-specific execution by one or more driver assistance systems of both steering and acceleration/ deceleration using information about the driving environment and with the expectation that the *human driver* perform all remaining aspects of the *dynamic driving task*	**System**	Human driver	Human driver	Some driving modes
***Automated driving system* ("system") monitors the driving environment**						
3	**Conditional Automation**	the *driving mode*-specific performance by an *automated driving system* of all aspects of the dynamic driving task with the expectation that the *human driver* will respond appropriately to a *request to intervene*	System	**System**	Human driver	Some driving modes
4	**High Automation**	the *driving mode*-specific performance by an automated driving system of all aspects of the *dynamic driving task*, even if a *human driver* does not respond appropriately to a *request to intervene*	System	System	**System**	Some driving modes
5	**Full Automation**	the full-time performance by an *automated driving system* of all aspects of the *dynamic driving task* under all roadway and environmental conditions that can be managed by a *human driver*	System	System	System	**All driving modes**

Figure 2.1: The definition of each level of automated driving [5].

levels other than level 5 limit ODD, and level 5 performs driving automation systems in all driver-manageable on-road operating situations. In this paper, more than level 3 is assumed in a discussion.

2.2 Dynamic maps

As human drivers use map applications or car navigation to access destinations, automated driving vehicles need similar functions to transport passengers or loads. Dynamic maps are key factors to navigate automated driving vehicles to destinations. Fig. 2.2 shows the structure of dynamic maps. Dynamic maps consist of four layers that are separated by transition time as follows.

- Highly dynamic data layer
  It takes one second to change the state of data, e.g. surrounding vehicles and pedestrians information, traffic light information.

- Transient dynamic data layer

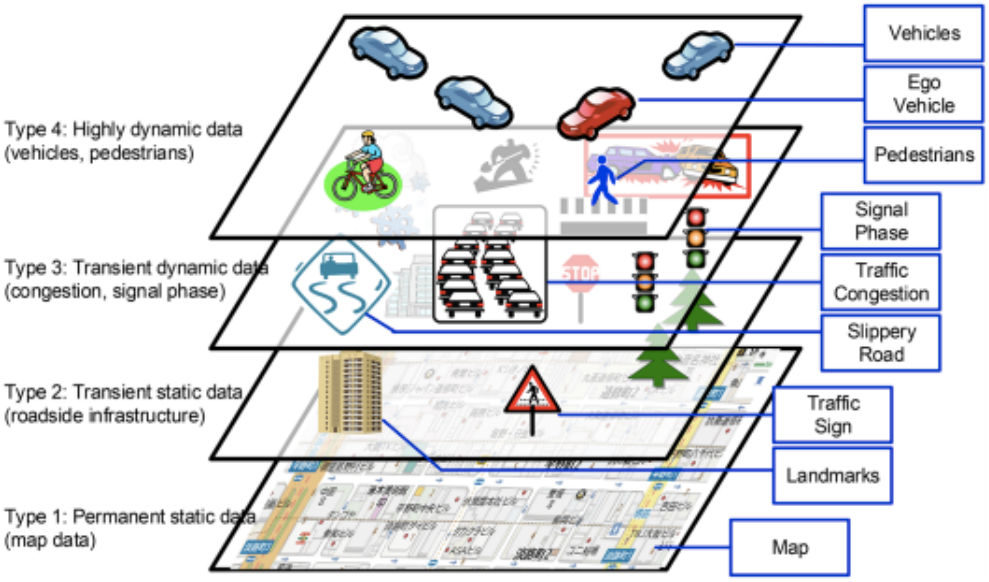

Figure 2.2: The information included in dynamic maps [22].

It takes about one minute to change the state of data, e.g. accident information, traffic jam information, narrow-area weather information.

- Transient static data layer
  It takes about one hour to change the state of data, e.g. traffic regulation information, wide-area weather information.

- Permanent static data layer
  It takes about one month to change the state of data, e.g. buildings, lane information, road information.

In [23], local dynamic map (LDM) is discussed to cooperate with Intelligent Transport Systems (ITS). The main idea of LDM comes from maintaining common information required in different applications. Common information is relevant to the safe and successful operation of ITS applications, which includes, for example, moving objects such as surrounding vehicles and stationary objects such as traffic road signs. LDM is located in an ITS station and is made by collecting sensor data from different sources. Fig. 2.3 shows the examples of data sources. In LDM, data describing real-world objects is categorized into four different types as same as the beforementioned four data layers.

2.3 Automotive sensors

In order to generate dynamic maps, automotive sensors are indispensable. Since dynamic maps are used not only for navigation but also for the perception of the surrounding environment and the localization of the surrounding objects, automotive sensors in automated

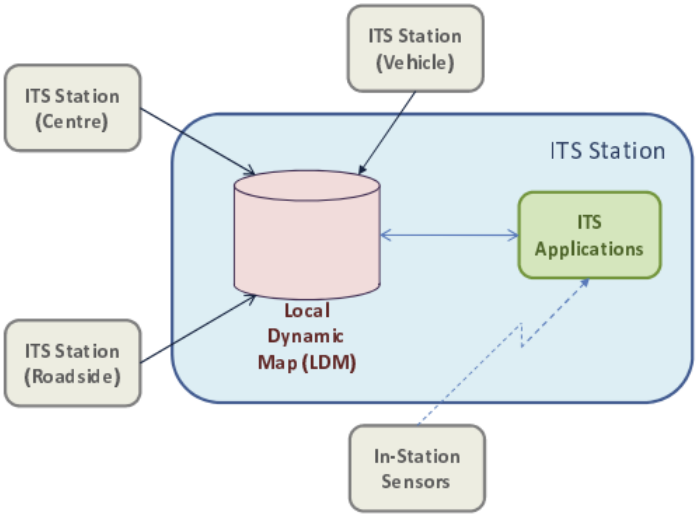

Figure 2.3: Relationship between LDM and its information sources [23].

driving play a more critical role than in human driving. This section will introduce what kind of automotive sensors are used in automated driving vehicles to generate dynamic maps. Sensors can be classified into proprioceptive sensors, or internal state sensors, and exteroceptive sensors, or external state sensors [24]. Proprioceptive sensors capture the dynamical state and measure the internal values of a dynamic system such as angular rate, wheel load. Inertia measurement units, gyroscopes, and global navigation satellite system receivers are examples of proprioceptive sensors. Exteroceptive sensors sense and acquire the information of the surrounding environment such as distance, light intensity. Camera, Radio Detection and Ranging (Radar), and Light Detection and Ranging (LiDAR) are examples of exteroceptive sensors. Multiple sensors are usually combined to obtain adequate information for safe driving. The following paragraphs introduce major automotive sensors.

Cameras are one of the most popular automotive sensors to perceive the surrounding environment. Cameras perceive the surrounding environment by detecting lights emitted from surrounding objects and provide images of the surrounding environment. Categories of cameras can be classified into monocular cameras, stereo cameras, or binocular cameras, and fisheye cameras. In order to support automated driving, both monocular cameras and stereo cameras can be equipped on automated driving vehicles. The main reason why both of the cameras are used comes from obtaining depth information. Conventional monocular cameras provide only RGB information, but some applications or advanced monocular cameras can provide depth information by using complex algorithms [25]. Stereo cameras, or binocular cameras, measure depth by capturing images from different image sensors. Fisheye cameras can capture more wide range than stereo cameras so that only four fisheye cameras can cover 360° view of the surrounding environment. Although sensor data obtained by fisheye cameras has strong radial distortion, it is shown that fisheye cameras can also help automated driving to detect objects [26]. Examples are shown in Fig. 2.4.

(a) Intel RealSense Depth camera D455

(b) Multi function monocular camera - MFC500 sold by Continental Automotive corporation.

(c) 180 degree fisheye lens car camera sold by Wskyfook

Figure 2.4: Examples of cameras.

LiDAR sensors are originally used in the mapping of aeronautical and aerospace terrain, but now LiDAR sensors are also used for perception in Advanced Driver Assistance System (ADAS). LiDAR sensors perform remote sensing by emitting lasers to the surrounding environment and detecting the reflected lasers. The wavelength of lasers is a key factor of LiDAR sensors. Near-Infrared (NIR) wavelengths, e.g. 905 nm, and Short Wave Infrared (SWIR) wavelengths, e.g. 1550 nm, are widely used by manufacturers ranging from known automotive Tier-1s to startups. Sensitivity to solar radiation, eye safety, environmental conditions, and cost are mainly discussed between different wavelengths as follows [27].

- Since there is about three times higher the amount of solar irradiance at 905 nm than at 1550 nm, NIR has to contend with more noise that can interfere with the sensor.
- NIR light can pass through the cornea and reach the retina in the human eye so that high power laser at 905 nm is not available from the viewpoint of eye safety. SWIR light is mostly absorbed within the cornea, and as a result, is able to be exposed at higher levels.
- When poor environmental conditions like rain or fog are introduced, the water absorption properties of SWIR light cause its performance to degrade more rapidly than a

(a) Velodyne LiDAR sensor VLS-128 that is mechanical LiDAR sensor.

(b) Ibeo LUX 4L that is solid state LiDAR sensor

Figure 2.5: Examples of different structure LiDAR sensors.

Figure 2.6: Advanced Radar Sensor - ARS441 sold by Continental Automotive corporation that uses 76-77 GHz.

NIR-based system. However, NIR still gets the effect of snow and fog [28].

- The cost of LiDAR sensors using SWIR system will be 10 to 100 times higher than using NIR system due to using new hybrid semiconductor technology.

The structure of LiDAR can be categorized into mechanical LiDAR sensor or solid-state LiDAR sensor as shown in Fig. 2.5. The mechanical LiDAR sensors use high-grade optics and rotary lenses driven by an electric motor to direct the lasers and capture the reflected lasers. On the other hand, solid-state LiDAR sensors do not use rotating lenses but use a multiplicity of micro-structured waveguides to direct the lasers. Therefore, solid-state LiDAR sensors can avoid mechanical failure. Although solid-state LiDAR sensors have robustness and reliability and is generally lower cost than mechanical LiDAR sensors, their horizontal field of view is more narrow than mechanical LiDAR sensors.

Radar sensors measure the targets of speed and relative position by radiating electromagnetic waves and using Doppler property for signal processing. Current automotive radar sensors operate mainly in the 77-81 GHz band and secondly in the 24 GHz band as an example is shown in Fig. 2.6. Since the 77-81 GHz band is defined by International Telecommunica-

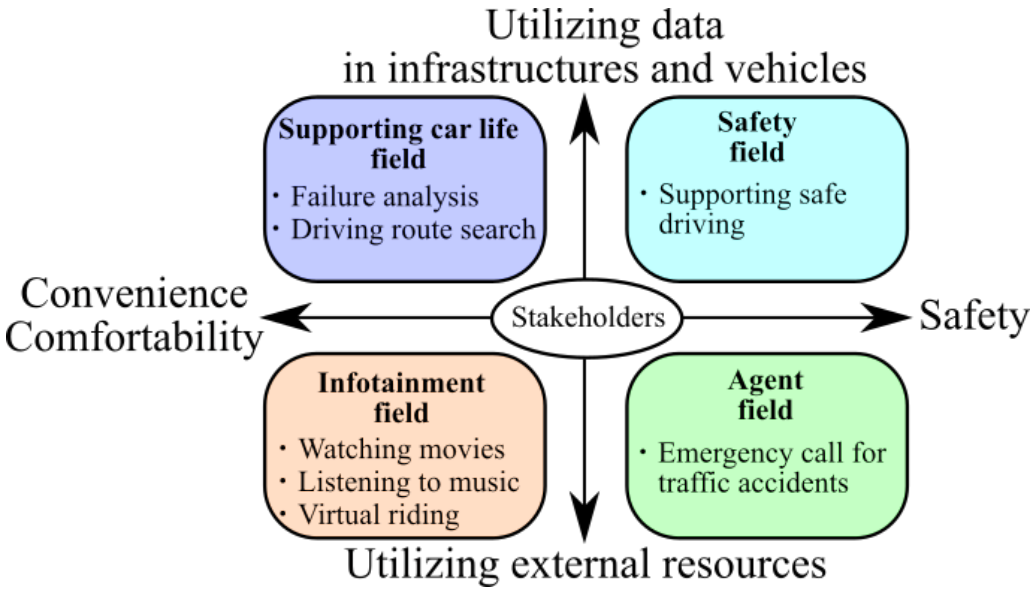

Figure 2.7: Services expected in connected car society [4].

tion Union-Radiocommunication sector (ITU-R), this band will be used for automotive radar sensors in the future. Since the propagation of electromagnetic waves is robust to adverse weather conditions and independent of environmental illumination, radar sensors can run at a day or a night or in foggy, snowy, or cloudy conditions.

2.4 Cooperative perception

Since using only one type of automotive sensor does not provide an automated driving vehicle with enough information, multiple automotive sensors are usually installed. However, there is a limitation for own automotive sensors to perceive the surrounding environment in every case. For example, buildings and vehicles can easily block the sensing of automotive sensors and make blind spots from the automated driving vehicle. In order to realize safe automated driving, automated driving vehicles must recognize the surrounding environment as few blind spots as possible. Cooperative perception is one of the connected car services and is expected to improve the driving quality. Connected cars indicate the group of cars that are connected via wireless communications as introduced in the next section. Fig. 2.7 shows the services in the connected car society. As shown, the services can be classified into safety, car life support, infotainment, and agent services. Cooperative perception, or collective perception, is the technology that shares sensor data obtained from different perspectives via wireless communications. In other words, automated driving vehicles receiving cooperative perception services can visualize blind spots.

There are two ways to realize cooperative perception, i.e., sharing processed or raw sensor data. Processed sensor data include information about the category and the location of the recognized objects. The main advantage of sharing processed sensor data is that complex

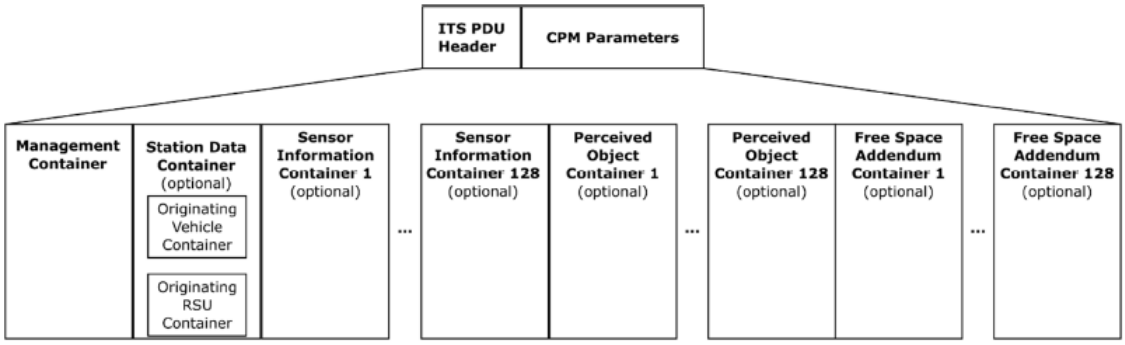

Figure 2.8: ETSI CPM format [8].

processes can be performed in a large number of computing resources and the high performance of wireless communications is not required. In [13], Shan et al. performed cooperative perception with an intelligent RSU in the real urban traffic environment that has an intersection. The intelligent RSU is equipped with a camera and a LiDAR sensor and the detection result is sent to vehicles in a European Telecommunications Standards Institute (ETSI) Collective Perception Message (CPM) format as shown in Fig. 2.8. The receiving vehicle not only receives the location of the shared perceived objects but also the uncertainty bounds of the objects. In [14], Tsukada et al. developed and conducted a roadside perception unit for automated driving. The developed cooperative perception sends Cooperative Awareness Messages (CAMs) encoded into CPMs to vehicles and the receiving vehicles know the location of the shared perceived objects. In [15], Dhawankar et al. proposed a framework for a cooperative platoon of autonomous vehicles. The cooperative platoon is controlled by sharing periodic safety information such as traffic information under a channel estimation model for V2I communication using IEEE 802.11p. The numerical results show that the purposed framework improves cooperative platoon driving. In [16], S. Kim et al. developed a cooperative system that provides camera and LiDAR sensor data and showed that the driving path of overtaking gets improved. The authors discussed the trade-off between communication delay and position error and showed that the average position error at 100 km/h can still be used for control purposes. However, communication delay becomes significantly uncertain, as the size of data increases.

On the other hand, when raw sensor data are shared, the receiving vehicle performs a recognition process in its system so that recognition results are free from errors due to the sender. However, in order to support sharing raw sensor data, large amounts of communication resources must be prepared to deal with the total sensor bandwidth from 3 to 40 Gbps [31]. Although sharing raw sensor data indeed gives a heavy channel load, it is necessary to guarantee distributed verification, which will be useful in emergency cases such as an infrastructure system error. Moreover, sharing raw sensor data can contribute to liability problems in the case of accidents and improving the accuracy of object localization [9]. In [24], it discusses sharing raw and processed sensor data from the viewpoint of sensor fusion. High-level fusion, which shares the results of detection and tracking algorithm carried

out by each sensor, can be realized under lower complexity and requires few communication resources. However, the process will cut off a part of the information in the raw sensor data. On the other hand, low-level fusion, which shares raw sensor data, can retain sensor information so that it has the potential to improve localization. Moreover, it can reduce the latency caused by the process and help to improve the performance of time-critical applications. However, it requires large amounts of computational resources and communication resources and needs precise calibration among sensors to fuse their data.

Realizing cooperative perception by sending raw sensor data has also been studied. In [17], raw LiDAR sensor data were exchanged through 60 GHz wireless communication, which was one of the millimeter-wave communications. The main characteristics of this work are that only point cloud data representing dynamic objects are shared in order to reduce redundant information sharing and the system is implemented. In the end, the authors compared transmitting full point cloud data and only dynamic objects from the viewpoint of throughput and latency. The results of experiments show that sharing full point cloud data is not realistic under IEEE 802.11ad communications. However, 700–900 Mbps was measured in the lab, which shows the potential of millimeter-wave communications. In [18, 19], a proof-of-concept of cooperative perception using millimeter-wave communications was shown by sharing raw LiDAR sensor data. At the measurement part, the authors showed that approximately 900 Mbps was achieved.

In order to guarantee safe automated driving by cooperative perception, the shared amount of processed or raw sensor data and the rate of sharing required by safe automated driving must be clarified. For example, in [7], the authors published the requirements for sharing both processed and raw sensor data. On the other hand, in [8], sharing raw sensor data was not considered due to the necessity of a large data rate.

The requirements for cooperative perception are actively studied by many groups. The 3rd Generation Partnership Project (3GPP) has published V2X service requirements which include use cases for low-level to high-level automated driving [7]. In the case of extended sensor services that are similar to cooperative perception services, 1 Gbps is required for high-level automated driving to prevent imminent collisions. Moreover, in the case of collective perception under raw sensor data transmission, 1 Gbps is required to visualize an all-around view [9]. On the other hand, 5G Automotive Association (5GAA), which develops end-to-end solutions for future mobility and transportation services, defines multiple groups based on 3GPP works, and presents requirements in multiple use cases for C-V2X (cellular-V2X) [10, 11, 12]. For example, cooperative perception corresponds to a use case of high-definition sensor data sharing that belongs to the group of autonomous driving. However, in high-definition sensor sharing, a specific data rate is not required.

By using millimeter-wave communications for sharing raw sensor data that provide large amounts of communication resources, one of the challenges in sharing raw sensor data can be solved. Therefore, the combination of sharing raw sensor data and millimeter-wave communications has a great synergy that can share raw sensor data without information loss and waiting time for the process.

In order to derive how much data rate is actually required to realize safe automated driving by sharing raw sensor data, this thesis analyzed the minimum required data rate for safe

automated driving. In [32], the overtaking scenario at a two-lane road is assumed and the required data rate is quantitatively derived by considering the recognition process based on using feature points. In [33], a safe crossing scenario at an intersection is assumed. However, using edge points for recognition is too primitive so that it is not used in practical recognition processes.

2.5 ITS and connected cars

The definition of ITS is a general term of new road traffic systems that regard people, vehicles, and roads as unified systems and aim to improve safety, transport efficiency, and comfortability of road traffic [34]. Electric Toll Collection (ETC), Vehicle Information and Communication System (VICS), Adaptive Cruise Control (ACC), and Cooperative ACC (CACC) are current underlying technologies of ITS. The following bullet points briefly introduce these technologies.

- ETC, or ETC2.0, enables vehicles installed with a dedicated onboard unit to drive through a toll gate without having to stop. It uses a 5.8 GHz band to communicate with onboard units. In advanced ETC, which is ETC 2.0, it starts to provide new services such as safe driving assistance and traffic congestion information. The installation of ETC decreases the frequency of traffic congestion at toll gates in a year from 3974 times to 60 times and also decreases the amount of CO2 emissions from 531 kt to 314 kt [35].

- VICS provides traffic regulation information and traffic congestion information through car navigation systems. It makes a profit six times as much as the installation cost of VICS [36].

- ACC and CACC are implemented to alleviate traffic congestion at road sags where more than half of traffic congestion occurs. In the case of CACC, it measures the surrounding environment not only by own sensors but also by obtained sensor data from surrounding vehicles.

Since the target of the current ITS is human-driven vehicles, future ITS that can support automated driving vehicles should be redesigned. In [37], cross-discipline cooperation of data, social issues about mobility, mobility services for diverse lifestyles, and environmental issues are mainly highlighted for future ITS. The vision of future ITS is set by the scale of a city such as rural areas, suburbs where private cars are mainly used for transfer, and urban areas where public transports are mainly used for transfer. High traffic efficiency, good balance of energy demand and supply, and high availability of services are set in common as goals among these three areas.

In order to achieve these goals, a Cyber-Physical System (CPS) is expected. CPS is a system that utilizes the synergy of a large amount and a wide variety of information collected by diverse sensors, which is performed in physical space, and a large scale of data processing that

yields new values, which is performed in cyber space. Since many obstacles block the measurement of sensors, in the case of adopting CPS to automated driving vehicles, surrounding information collected by own sensors cannot show the full potential of cyber space. Therefore, using sensor information obtained from different objects such as vehicles is planned to provide enough information for safe automated driving and yield new services. This concept is called connected cars. In this system, wireless communications play a role to send different sensor information. When vehicles communicate with each other, cooperative perception and CACC are major services that are mainly related to safety services as beforementioned. On the other hand, when vehicles communicate with infrastructures, traffic alert systems and driving monitoring are major services.

The required characteristics of wireless communications are different among ITS services and depend on coverage and data type. The following bullet points briefly summarize the characteristics.

- Coverage
  - Narrow area communications are mainly used in safety services. V2V and V2I communications are examples of narrow area communications, and exchanging highly dynamic data for updating dynamic maps is one of the services.
  - Wide area communications can be used in diverse services, and LTE and 5G are expected for this communications so that it can provide almost constant connection. Transient dynamic data, transient static data, and permanent static data are exchanged via this communication.
  - Spot communications are the communications that can access in specific areas. ETC2.0 is the expected system that provides spot communications. This communication can be used for services that broadcast traffic information in a specific area.
- Data type
  - A large amount of data that is exchanged at a high frequency, e.g. probe information, is used in safety services and car life support services.
  - Large data such as video is used in car life support services and infotainment services.

2.6 V2X communications

In order to meet different required characteristics of wireless communications, Dedicated Short Range Communications (DSRC) and cellular communications are listed as candidates. In the following subsections, the characteristics of the candidates are introduced.

Table 2.1: The standards of major DSRC [38].

Region	Japan	Europe	North America
Standard	ARIB STD-T55 ARIB STD-T75 ARIB STD-T88 ARIB STD-T110 etc.	ETSI EN 302 571 ETSI EN 302 665 ETSI EN 302 636-6-1 etc.	ASTM E2158-01 IEEE 1609.0 IEEE 802.11-2012 etc.
Band	755.5–764.5 MHz 5770–5850 MHz	5470–5725 MHz 5795–5815 MHz 5855–5925 MHz	902–928 MHz 5850–5925 MHz
Application	Toll collection Road conditions Emergent disaster	Safety applications Traffic telematics Future ITS applications	Toll collection Road safety Vehicle traffic optimization applications

2.6.1 DSRC

DSRC refers to a wireless technology that enables vehicles and ITS to exchange information via short-range communication. DSRC is utilized for many automotive applications and ITS applications such as toll collection and collision prevention. However, the reserved radio spectrum bands are different in the world as shown in Table. 2.1, which leads to incompatibility.

As shown in the table, DSRC plays an active role in the traffic environment so that many social issues are improved, and many collaborative efforts are made to improve the technology. However, DSRC still suffers from some limitations. The first limitation is its communication range. Since DSRC only works in small areas, it is difficult to provide constant Internet access during driving as cellular communications. If vehicles drive at a high velocity, the period of DSRC area becomes short so that this problem gets severe. One way to solve this problem is installing additional DSRC points and enabling multihop communications. In this case, it has to have the ability of highly dynamic network topology because the network path for a driving vehicle changes according to its located DSRC area. However, this function will deteriorate the latency of DSRC.

The second limitation is the scalability that is caused by Carrier Sense Multiple Access / Collision Avoidance (CSMA/CA) technique, which is the main contention-based Medium Access Control (MAC) scheme. In a high-density vehicle scenario or a high network load scenario, the performance of DSRC is significantly degraded due to a high transmission collision rate. In [39], the performance of Institute of Electrical and Electronics Engineers (IEEE) 802.11p is estimated by packet delivery ratio. The results show that when the value of packet

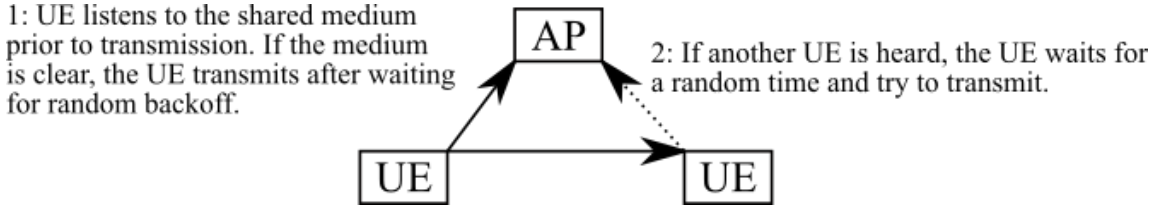

(a) The basic procedure of CSMA/CA.

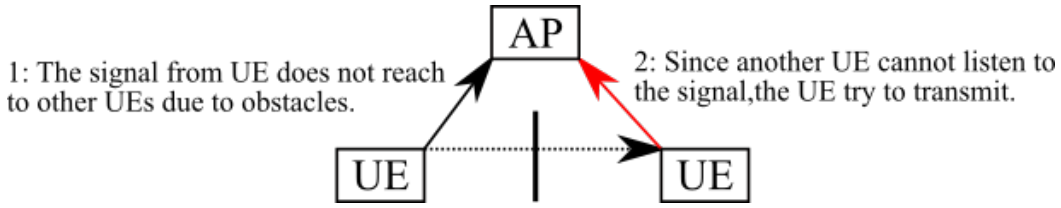

(b) A hidden terminal problem in CSMA/CA.

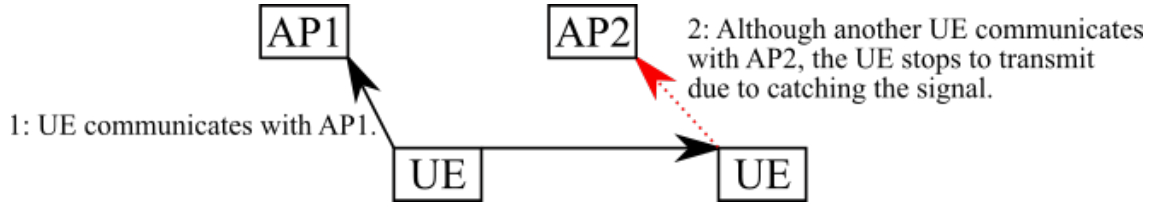

(c) A exposed terminal problem in CSMA/CA.

Figure 2.9: The basic procedure and the problems of CSMA/CA.

per second (pps) changes from 10 pps to 50 pps among 120 vehicles/km, the performance of packet delivery ratio gets significantly degraded due to high load.

Moreover, CSMA/CA systems have problems due to their procedure. Fig. 2.9a shows the basic procedure of CSMA/CA that describes a listen-before-talk mechanism. Fig. 2.9b and Fig. 2.9c show the typical problems caused in CSMA/CA systems. Firstly, Fig. 2.9b shows hidden terminal problems. These problems are mainly due to incomplete listening that is caused by obstacles so that transmission collisions are caused. Next, Fig. 2.9c shows exposed terminal problems. On the contrary to the cause of hidden terminal problems, exposed terminal problems are caused during a normal listening phase. In other words, the UE misunderstands that another UE is talking with the same AP despite another UE's talking with a different AP.

2.6.2 C-V2X

C-V2X communications are regulated by the 3rd Generation Partnership Project (3GPP). Supporting V2X applications starts from Rel. 14. The main problems of using cellular infrastructure are that vehicles cannot always establish a connection with cellular infrastructure. In order to solve these problems, C-V2X newly defines direct V2X communication modes

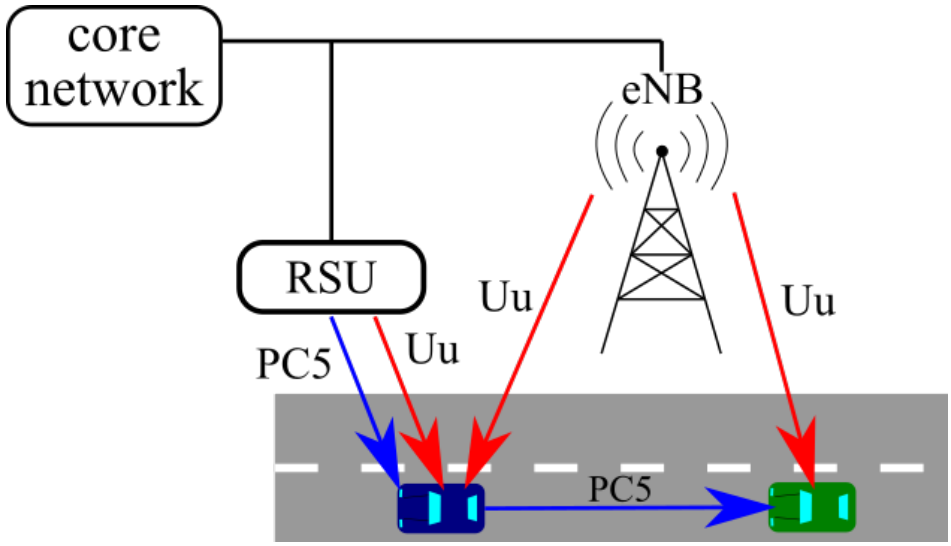

Figure 2.10: Two types of air interfaces.

that use sidelink channels over the PC5 interface [41]. Since C-V2X operates in both in-coverage and out-coverage, two types of air interfaces such as LTE-Uu interfaces and PC5 interfaces are developed as shown in Fig. 2.10 [42].

The LTE-Uu is the traditional air interface between an evolved Node Base station (eNB) and a User Equipment (UE). Using the LTE Uu interface, a UE can transmit a packet to the eNB in the uplink. In the case of downlink, the same or a different eNB can transmit this packet to a far away UE either using unicast downlink or enhanced Multimedia Broadcast Multicast Service (eMBMS). From this downlink function, the LTE Uu interface has the ability to increase the dissemination range, which is the result of utilizing the cellular core network. Another advantage to use the LTE Uu interface is that the eNB can use semi-persistent scheduling for UEs. Semi-persistent scheduling can reduce the scheduling overhead associated with uplink transmissions.

The PC5 air interface enables direct communications between UEs without passing through eNBs. Transmitted packets via the PC5 interface consist of not only the data component but also the sidelink control information. Using the PC5 interface, there are two modes for sidelink transmissions. In C-V2X sidelink mode 3, allocation of resources for sidelink transmissions is performed by the eNB. When the UE is in the coverage of the eNB, this mode is available, and some functions that can be used in the LTE Uu interface such as semi-persistent scheduling are also available. In C-V2X sidelink mode 4, it is available at outside eNB coverage. UEs reserve resources autonomously by using the resource reservation algorithm.

From the viewpoint of the performance of C-V2X, since C-V2X sidelink mode 3 can use resources efficiently by a central controller, the performance gets more gradually degraded than DSRC according to increasing vehicle density in a large awareness range [43, 44]. Moreover, in [39], it shows that the performance of C-V2X sidelink mode 4 is superior to DSRC in terms of a higher link budget. Although the degradation speed of C-V2X is lower than DSRC, increasing vehicle density still makes a great impact on the performance of C-V2X.

In order to solve this problem, redundant transmissions are also analyzed. The results show that the performance is improved under low loads while the performance gets degraded under high loads. In [45], the authors perform the experiment and compare the communication performance of IEEE 802.11p and LTE-V and show that a RSU that transfers V2V messages improves the communication performance.

2.6.3 IEEE 802.11bd

Since advanced PHY and MAC techniques are developed after the publication of IEEE 802.11p, the new evolved standard of IEEE 802.11p is expected for vehicular technology, which is called IEEE 802.11bd. The primary design objectives of this new standard are shown as follows [41, 46].

- At least one mode achieves twice the MAC throughput of 802.11p with relative velocities up to 500 km/h.
- At least one mode achieves twice the communication range of IEEE 802.11p.
- At least one form has vehicle positioning in affiliation with V2X communications.

The mechanisms of IEEE 802.11bd are renewed from IEEE 802.11p to support vehicular applications. The first new mechanism is midambles. Since relative Doppler spread gives effect to the communication performance under the 802.11 PHY layer at typical vehicle speeds, midambles are proposed to solve the trade-off between multi-path fading and relative Doppler spread. The form and the function of midambles are similar to preambles except for the location of midambles in the frame. In a fast fading channel, the channel estimation in preambles is only valid to the initial data components. Midambles are located between data components to track the channel state so that the probability of errors will be reduced.

Another way to increase reliability under a fast fading channel is a retransmission of one or more packets. This function can be used for both IEEE 802.11p and IEEE 802.11bd. Moreover, Dual Carrier Modulation (DCM) is also another way to reduce errors. DCM uses sufficiently far-apart sub-carriers that can achieve frequency diversity and sends the same symbols twice through the sub-carriers, which can improve block-error-rate performance. However, the modulation scheme must be doubled to maintain the throughput in no DCM.

In [47], it estimates the performance of IEEE 802.11bd under several factors such as urban, rural, and highway environments and Line-of-Sight (LoS) and NLoS. The first results show that Packet Error Rate (PER) among all scenarios is too high to support ultra-reliability. The second results show that midambles improve the PER performance in the worst scenario.

Other remarkable characteristics are the utilization of millimeter-wave frequency bands and the support of vehicle positioning. Although millimeter-wave communications have smaller coverage than cellular communications due to their propagation characteristics, millimeter-wave communications can achieve high throughput with low order modulation and coding scheme. Therefore, millimeter-wave frequency bands are effective in vehicular applications that require very high throughput in small distances such as video streaming and downloading

high-resolution dynamic maps. In the case of vehicle positioning, next generation positioning that is provided by IEEE 802.11ax is adopted.

2.6.4 NR-V2X

As beforementioned, C-V2X has still challenges and needs evolution to support advanced vehicular applications. NR-V2X is designed to support advanced vehicular applications that require severe requirements, and it does not aim to replace C-V2X but aims to support C-V2X [41]. Therefore, the coexistence of C-V2X and NR-V2X are planned and NR-V2X is expected to support both advanced vehicular applications and basic safety applications to provide unified support in the future.

NR-V2X will support many applications that require different requirements about latency, reliability, and throughput. Moreover, the number of receivers is also different among applications. Therefore, NR-V2X introduce two new communication types that are unicast and groupcast. As IEEE 802.11bd plans to use millimeter-wave communications for advanced vehicular applications, NR-V2X also considers using millimeter-wave communications. Other objectives in NR-V2X include enhanced sidelink design, Uu interface enhancements, RAT/Interface selection, and QoS management.

In NR-V2X, new mechanisms are introduced to support advanced vehicular applications. The first new mechanism is mini-slot scheduling that will be used for latency-critical messages. This mini-slot scheduling enables UEs to start their transmission from any of the 14 Orthogonal Frequency Division Multiplexing (OFDM) symbols in a subframe. Moreover, combining multiple slots, which is called multi-slot, is introduced to support exchanging large size packets.

In [47], it estimates the performance of NR-V2X compares its performance with IEEE 802.11bd. The first results show that NR-V2X performs equally well among different scenarios. The reason for this performance is that NR-V2X can provide dynamic configurations of Demodulation Reference Signals (DMRSs) according to the channel state.

In order to implement NR-V2X, it has to solve challenges. Since NR-V2X is not backward compatible with C-V2X, the coexistence of C-V2X and NR-V2X is the major problem. This incompatibility comes from the difference in subcarrier spacing. C-V2X operates at 15 kHz and cannot decode messages using 30 and 60 kHz spacing. Therefore, C-V2X and NR-V2X will use different channels for coexistence, and two approaches are considered. The advantages and the challenges of the two approaches are shown as follows [48].

- Frequency Division Multiplexing (FDM)
  - The advantages of this approach are that tight time synchronization between C-V2X.
  - The drawbacks are that, if the assigned channels are not sufficiently far apart, interference will occur at reception. Moreover, if the two communication systems use the same band, the total power radiated by the vehicle may be restricted by regulatory limits so that the required Quality of Service (QoS) may not be achieved.

- Time Division Multiplexing (TDM)
  - In TDM approach, the maximum permissible power can be used by both technologies. Moreover, there is no leakage across channels.
  - TDM approach is not appropriate to latency-critical use cases due to waiting for the assigned slot.

2.7 Overview about safety

This section introduces the current approaches toward safe automated driving. Firstly, qualitative discussion about safety is shown before starting the quantitative discussion. In [52], safety is discussed from the viewpoint of operation approval and a safety target. The basis of operation approval should meet the following RAMS to ensure safe and reliable transportation to passengers and identify that companies comply with the rules and the regulations from those that are unable to do.

- Reliability is the ability of product or system to perform a specific function and can be broken up into two parts, design reliability or operational reliability.
- Availability is the ability of a system to be kept in a fully functioning state.
- Maintainabilitiy is determined by the ease with which the product or system can be repaired or maintained.
- Safety is the requirement not to harm people, the environment, or any other assets during the life cycle of a system.

Although some accidents are caused by the failure of automated driving features such as the Tesla crash, it is said that automated driving vehicles are 1.5 times safer than traditional human driving vehicles. Considering this fact, many societies have different philosophies on safety targets. In [53], European countries discuss risk assessment for transport safety, and one of the discussions focuses on rail transport that is a more highly controlled transport than road transport. Since automated driving vehicles will be installed with highly controlled systems, the risk assessment for rail transport will be a good reference. It is obvious that there is no generally accepted criterion for deciding what railway safety measures are needed. However, there is a widespread view that current safety performance is reasonably good. The following items show general principles to measure safety.

- Globalement Au Moins Équivalent (GAME)
  The basic concept of GAME is that any change to a system must leave it at least as safe as it was beforehand. It is a formal adoption of the present level of safety as a benchmark and is an absolute criterion. France, Germany, and Norway explicitly adopt the GAME principle.

- As Low As Reasonably Practicable (ALARP)
  This is a legal requirement in the United Kingdom. It involves some trade-off between the costs and benefits of safety measures, though the terms of that trade-off remain subject to debate.

- Minimum Endogenous Mortality (MEM)
  Its basic concept is that the risk of death to individuals shall be less than a specified limit. This is also an absolute criterion. Germany and the UK adopt it, though the UK limit does not bind in practice, because it is higher than the risks that are actually encountered.

In [54], it shows a framework or guideline for the safety of automated driving systems for all companies in the automotive and mobility world to contribute to the industry-wide standardization. Moreover, it aims to develop guidance to tackle the risks introduced by automated driving vehicles. Its discussion starts from the positive risk balance. In other words, it is true that automated driving vehicles still have challenges to realize no traffic accidents, but they have a great potential to reduce the traffic accident rate, which is a great motivation to develop automated driving vehicles [55]. Its goal is to present a generic approach for tackling the risks introduced by automated driving vehicles. The generic approach is based on the twelve principles that are made by a collection of publications and recommendations from mainly public authorities or consumer associations. The principles consist of safe operation, operational design domain, vehicle operator-initiated handover, security, user responsibility, vehicle-initiated handover, interdependency between the vehicle operator and Automated Driving System (ADS), safety assessment, data recording, passive safety, behavior in traffic, and safe layer. This basis is supported by safety by design and Verification & Validation (V&V). Safety by design aims to describe how to combine safety of the intended functionality, functional safety, and cybersecurity to create a dependable system. V&V focuses on the main steps that are essential for the safe deployment and continued operation of SAE L3 or higher automated driving systems.

In [56], Japan Mobile Manufacturers Association Inc. (JAMA) has summarized the best practice on safety argumentation structuring, safety evaluation, and safety assessment methods needed to enable logical completeness, practicability, and transparency of autonomous driving safety on limited access highways. Firstly, it refers to the United Nations Economic Commission for Europe (UNECE) WP29 document [57]. In this document, safety vision is regarded as ”Automated vehicles shall not cause any non-tolerable risk meaning that automated vehicle systems, under their operational domain, shall not cause any traffic accidents resulting in injury or death that are reasonably foreseeable and preventable”. Fig. 2.11 shows a matrix of the contextualized safety philosophy of WP29 document based on foreseeability and preventability and the following itemizations. This work also follows this safety vision and focuses on the validation of system safety under foreseeable and preventable cases.

- foreseeable and preventable
  It accounts for all scenarios for which an accident is foreseeable and preventable and no accidents are acceptable.

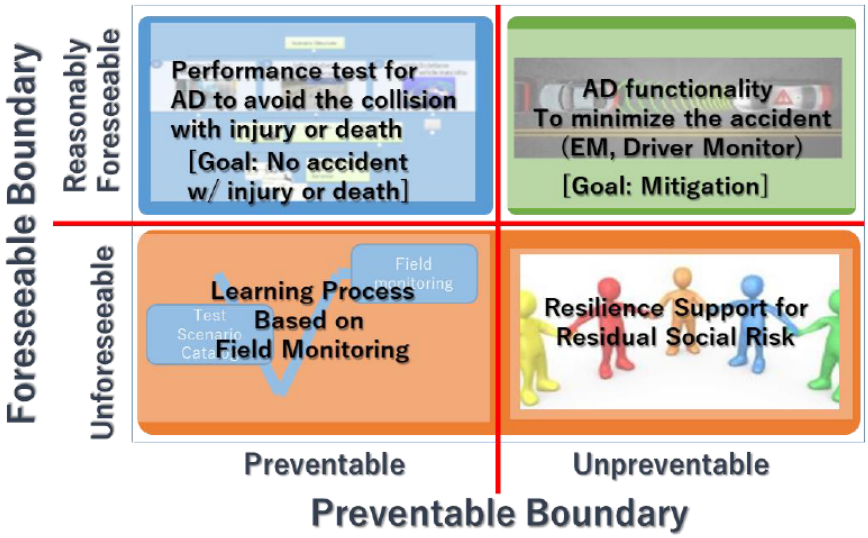

Figure 2.11: Safety approach in context with foreseeability and preventability matrix [56].

- foreseeable and unpreventable
  The situations that fall under this category are situations for which mitigation is the only option.

- unforeseeable and preventable
  It depicts the traffic situations that cannot be foreseen but that can be prevented. The cases that fall under this category form the basis for learning and serve as a precedent for future generation automated driving system developments.

- unforeseeable and unpreventable
  In these situations, resilience support in the form of legalities, the division of responsibilities, health support, insurance, and other such areas need to be the focus of attention.

The method to evaluate safety starts from defining quantified ranges of reasonable foreseeability and preventability for each assumed scenario. The preventability of an automated driving system refers to the collision avoidance performance that is equal to or better than the performance achieved by a competent and careful human driver. On the other hand, foreseeability is based on physics principles and extreme violation of traffic rules by an ego-vehicle driver and other drivers. After calculating the quantified ranges for each scenario, it additionally considers perception disturbance and vehicle stability disturbance. Perception disturbances are considered to avoid collisions in any of the traffic disturbance scenarios. The examples of perception disturbance are that a vehicle fails to detect existing objects, which is a false negative, and objects are falsely detected under no existing objects, which is a false positive. Vehicle stability disturbances are also considered to ensure that automated driving vehicles can stabilize themselves without halting driving under vehicle disturbances such as wet roads, frozen roads, and a gust of wind.

2.8 Scenario selection

This section discusses the safety of automated driving in this paper, but traffic environments depend on many factors such as road shape, the location of vehicles, and the distribution of velocity. Therefore, the discussion starts by specifying road shape. From [49], it summarizes the type and the location of traffic fatalities that occur between vehicles in Japan as shown in Fig. 2.12 and Fig. 2.13. The summarized statistics show that head-on collisions account for half of the traffic accidents on single roads. On the other hand, collisions and accidents at turning right account for more than half of the traffic accidents on intersections. Moreover, the total number of traffic accidents at intersections and at single roads are nearly the same number. From [50], it shows statistics about traffic fatalities that occur at unsignalized and signalized intersections in the United States of America. The sum of traffic fatalities at unsignalized and signalized intersections is about one-third of the total traffic fatalities in 2018. In detail, the total number of traffic accidents at unsignalized intersections is about twice as much as the total number of traffic accidents at signalized intersections. From [51], 43% of all road injuries occur at intersections in European Union (EU) 27. Summarizing all of the statistics of traffic accidents, target locations for the analysis of safe automated driving are set to single roads and unsignalized intersections.

After selecting the type of traffic accidents, the behaviors of automated driving vehicles have to be also assumed in the assumed traffic accidents. In [58], ADS is discussed to describe the identification of ADS features for level 3-5 ADS. The motivation of this analysis comes from identifying ODDs and Object and Event Detection and Responses (OEDRs), developing preliminary tests and/or evaluation methods, and assessing Fail-Safe (FS) and Fail-Operational (FO) mechanisms. Achieving these objectives helps to consider validation and verification approaches for ADS. A functional system architecture for ADS features was informed by SAE. The behaviors of automated driving vehicles are one of the ADS features and can be classified by the duration of the behavior as follows.

- Strategic/Mission Level (10+ sec)
  - Route planning
  - Follow driving laws
- Tactical Level (1-10 sec)
  - Maneuver planning, e.g., lane following, merging, etc.
  - Object and event response execution, e.g., cut-in by another vehicle
- Operational Level (0.01-0.1 sec)
  - Split-second adjustments to lateral and longitudinal control

Since the strategic/mission-level behaviors are not part of dynamic driving tasks, it summarizes tactical and operational behaviors that relate to ADS driving control. In the summarized list, maneuvers of overtaking and passing through an intersection are included. Therefore,

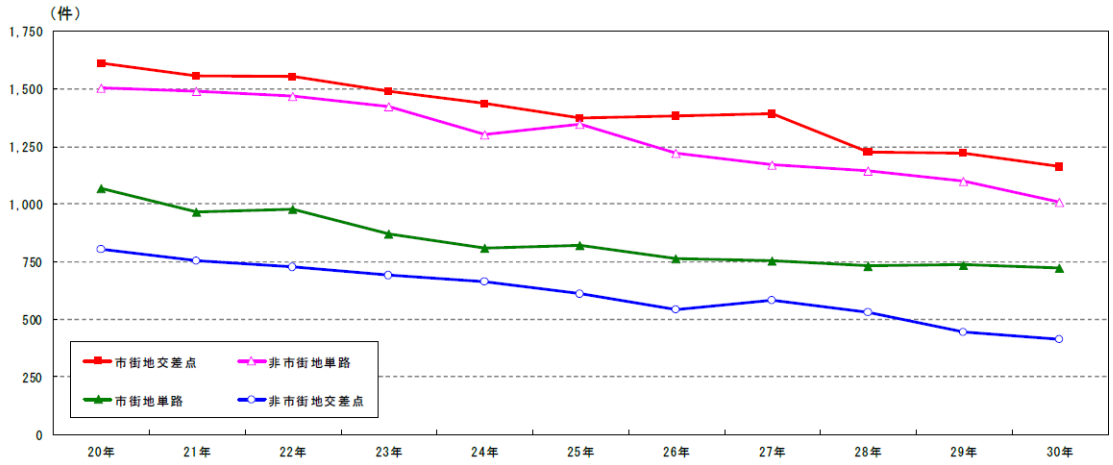

Figure 2.12: Traffic fatalities in Japan classified by road shapes [49]. The red line shows the transition of the number of traffic fatalities at urban intersections, the pink line shows the transition at rural single roads, the gree line shows the transition at urban single roads, and the blue line shows the transition at rural intersections.

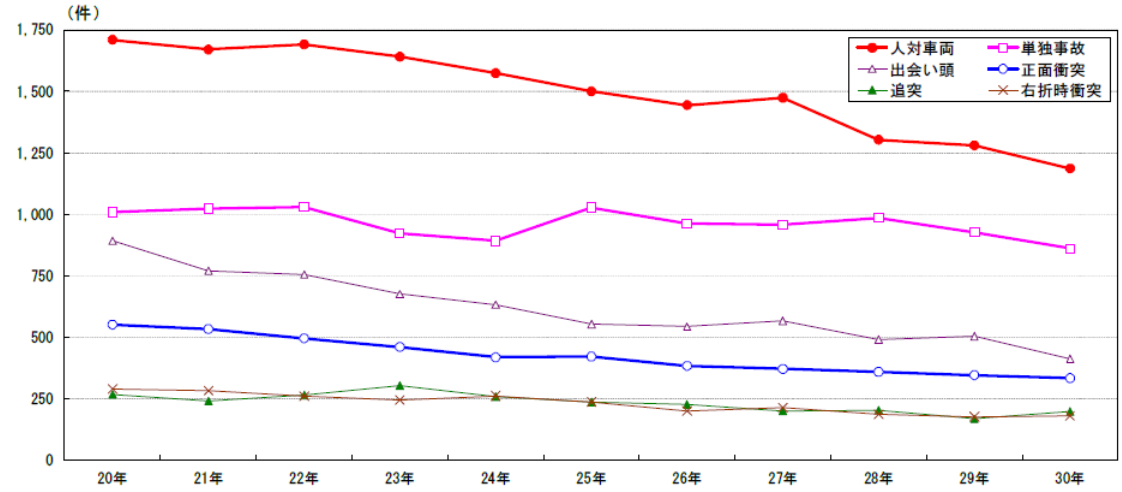

Figure 2.13: Traffic fatalities in Japan classified by accident types [49]. The red, pink, purple, blue, green, and brown lines show the transition of the number of traffic fatalities about vehicles and pedestrians accidents, one-car accidents, sudden meeting accidents.

this analysis focused on two scenarios of overtaking at a two-lane road and passing through an unsignalized intersection, where traffic accidents often occur.

Chapter 3

Required and achievable data rate for V2V in overtaking scenario

In this chapter, analysis of safety in the overtaking scenario is performed and cooperative perception is considered for improving safety. Cooperative perception is performed by sending raw sensor data. The analysis derives the requirements of sensor data rate for safe overtaking with and without cooperative perception. As introduced in chapter 3, the analysis of safe automated driving is discussed mainly in an automotive domain such as vehicle dynamics. This analysis and the following analysis of the intersection scenario consider not only vehicle dynamics but also recognition processes, which will lead to realistic requirements.

3.1 Scenario description

An overtaking scenario on a two-lane road is illustrated in Fig. 3.1. Since it takes a long time to transit from human driving vehicles to automated driving vehicles, this scenario focuses on a transition period that both automated vehicles and human driving vehicles drive on the road, which limits cooperative control. The driving scenario is that the green ego vehicle tries to overtake the blue leading vehicle while the red vehicle comes from the oncoming lane. The type of vehicles in this scenario is that the green ego vehicle and the blue leading vehicle are automated driving vehicles and the red oncoming vehicle is a human driving vehicle. Since frequent acceleration and deceleration do not occur on a straight road, the ego and the oncoming vehicles run with the same velocity V for simplicity. When the green ego vehicle tries to overtake, the blue leading vehicle drives slow enough for simplicity. Other factors in this scenario are also important. The conditions of other factors are summarized in the following bullets.

- The probability of the failure of automotive sensors and vehicle components is not considered. This assumption leads to no discussion about redundant structure.
- The delay of the recognition process that includes the perception by the LiDAR sensor and transmission of sensor data is regarded as negligible.
- The state of the weather is assumed to be dry and sunny weather and no wind. This assumption simplifies vehicle behavior, the performance of wireless communications,

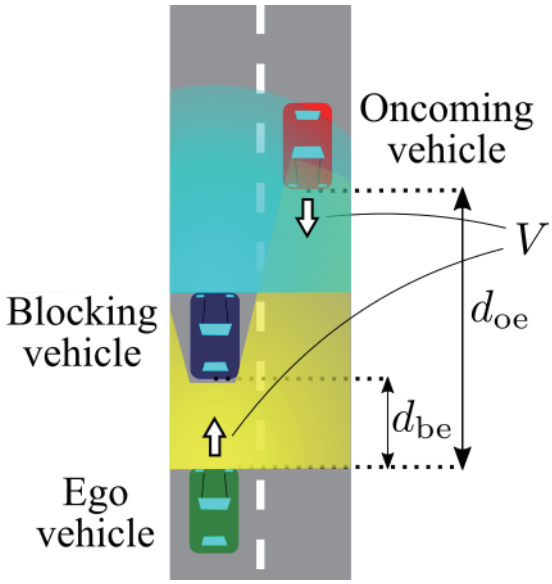

Figure 3.1: Illustration of the ego vehicle equipped with a 3D LiDAR sensor trying to execute overtaking on a two-lane road. The yellow (blue) region is the sensing region of the ego (blocking) vehicle. The red vehicle is coming from the oncoming lane.

and the perception by the LiDAR sensors. For example, when the road surface is wet or frozen due to snow or rain or sudden gust occurs, the ego vehicle may lose its control due to sliding. Snow and rain also have an effect on wireless communications and degrade their performance, especially on millimeter-wave communications [59]. Since remaining water caused by rain or melting snow leads to missing returned lasers, dry weather ensures a normal measurement of the LiDAR sensor.

It is necessary to select automotive sensors that are used for the recognition process. There are 2D and 3D object detection methods in the current detection methods. 2D object detection is good at detecting the categories and the bounding boxes of objects, but it is not good at providing depth information. On the other hand, 3D object detection can provide spatial information that is essential for navigation and avoiding obstacles, but it needs to estimate more parameters than 2D object detection. Since this analysis considers driving paths and avoiding obstacles, 3D object detection methods are required. Current methods for 3D object detection mainly use cameras and LiDAR sensors and are divided into image-based methods, point cloud-based methods, and multimodal fusion-based methods. As introduced in the automotive sensors section, cameras can provide texture information and are cheap, but they are not good at providing depth information and are sensitive to weather conditions such as very high and low luminosity, rain, and snow. LiDAR sensors can provide accurate 3D spatial information and are robust to weather conditions, but the information is nonuniform and sparse at a far place. Moreover, although the price of LiDAR sensors gets cheaper, their price is still more expensive than cameras. Considering these characteristics, cameras and

LiDAR sensors have complementary relations so that using both cameras and LiDAR sensors will be indispensable to ensure safe automated driving. However, multimodal fusion-based methods are less mature than image-based methods and point cloud-based methods.

These three object detection methods have advantages and disadvantages due to their sensors [60, 61]. Image-based methods can be classified by whether depth information also is used or not. 3D object detection based on RGB information starts to detect 2D candidates and estimate 3D space localization and size. Since it does not use depth information, there is a limitation to the accuracy of 3D localization. On the other hand, current sensors such as Microsoft Kinect can provide RGBD information, but large computation resources are required.

Point cloud-based methods can be classified into projection base, volumetric representations, and point-nets. The following bullets explain the characteristics of each method.

- Projection-based methods utilize object detection in 2D images that is mature technologies in the computer vision community. These methods project 3D points into 2D images to utilize 2D object detection methods. However, all information in 3D points cannot be included in the 2D images so that the accuracy of object detection gets low, but a real-time detection can be achieved.

- Volumetric methods assume that all objects and all scenes are represented in a voxel representation. One advantage of these methods is that sharp information can be explicitly encoded. However, most of the voxel is empty so that computational efficiency gets degraded and 3D data of the voxels requires large computational resources.

- Point-nets methods attempt to input raw point cloud to traditional feed-forward deep neural networks. Raw data is used to avoid information loss through preprocesses that are performed in projection-based methods and volumetric methods. However, there is a gap between object classification and detection.

Multimodal fusion-based methods are proposed to utilize both texture information and depth information. Texture information is useful for discrimination in object detection and classification and can provide a means of detecting far objects, but it is not good at estimating 3D spatial values. Depth information can accurately estimate 3D localization and size, but the density of point clouds gets sparse at a far place and the ability of object discrimination is not as good as texture information. Considering both characteristics of texture information and depth information, multimodal fusion-based methods can compensate for each disadvantage. Multimodal fusion-based methods can be classified into early fusion, late fusion, and deep fusion. Early and late fusion differ in the order of combining the sensor data and detection process, and deep fusion is the method of utilizing neural networks for multimodal fusion. Although multimodal fusion-based methods estimate 3D spatial values better than image-based methods, the accuracy of 3D spatial values still depends on the density of LiDAR sensor data.

Since the ego vehicle needs the accurate distance between the vehicles in this scenario, point cloud-based methods are adopted. The reason why this analysis chooses not multimodal fusion-based methods but point cloud-based methods is not only for simplifying the

recognition process but also comes from three aspects. The first aspect relates to the sensor information that the ego vehicle prioritizes. As beforementioned, the ego vehicle needs accurate 3D spatial values for the decision-making of path planning. Moreover, the ego vehicle does not have to detect many types of objects but has to detect only vehicles in this scenario so that advanced performance of object classification is not required. The second aspect is the robustness to weather conditions. In [63], the effect of weather conditions on image-based methods and point cloud-based methods is analyzed. The results show that the percentage of recognition accuracy in image-based methods is more affected than point cloud-based methods even if the threshold for the recognition is configured as ±10 m. Although the weather in this scenario is fixed to be dry and sunny weather as beforementioned, robustness to weather conditions will be useful at extending the environment of the scenario. The third aspect is the amount of output data rate. The output data rate of LiDAR sensors is dominant among automotive sensors, which has a great effect on the required performance of wireless communications for cooperative perception. For example, Velodyne LiDAR VLS-128 requires a 1 Gbps Ethernet connection.

In human driving, overtaking at a high velocity is very dangerous especially on a road without a lane separator for the oncoming traffic like on a highway. The basic behavior of overtaking in human driving is to slow down, make space behind the leading vehicle, obtain a clear view of traffic to observe the curvature of the road, and move closer to the center of the neighbor lane. Once the road ahead is considered safe for overtaking, the driver accelerates and starts the maneuver. However, there can be miss judgments because the leading vehicle prevents the ego vehicle from seeing the oncoming vehicle directly. On the other hand, automated vehicles with cooperative perception can obtain traffic information beyond the limitations of a view from a driver seat, which leads to less acceleration and deceleration and drive more safely than human driving vehicles. Considering many level 4 automated vehicles are equipped with the feature of lane centering, it is assumed that all vehicles run on the center of the road [58]. Using this lane centering function, this analysis assumes that beam alignment used in the V2V communication for cooperative perception is ideally performed. The problem is that many beams from the LiDAR sensor are blocked by the leading vehicle. From this point, the blue leading vehicle is called the blocking vehicle. Since the ego vehicle and the blocking vehicle are automated driving vehicles, the ego vehicle can communicate with the blocking vehicle, and compensate for blind spots by cooperative perception.

When cooperative perception is performed, important points about automotive sensors are not only the selection of the types of automotive sensors but also how to send sensor data. This analysis chooses sharing not processed sensor but raw sensor data in order to achieve the benefit of no loss information and no need of the verification of correct result that sharing processed sensor data cannot provide. Although reshaping raw sensor data is not utilized for cooperative perception or V2X communications in the current research, it is a key factor to reduce the amount of sharing raw sensor data. To the best of the author's knowledge, semantic segmentation, resampling, and non-linear sampling can be used for reshaping raw sensor data. The following bullets explain the characteristics of each method.

- Semantic segmentation is a process that separates point cloud into object groups such

as car and road. In [64, 65], authors performed semantic segmentation for automated driving. They show that the accuracy of their proposed segmentation is better than conventional methods. Although there is a trade-off relation between accuracy and processing time, their methods can be performed in real-time computation with high accuracy. However, all segmentation method does not well segment objects other than cars and roads.

- Resampling is a method that selects only feature points from a measured point cloud. In [66], it proposed a method that mainly extracts feature points. However, as the amount of point cloud increases, its processing time linearly increases.

- Non-linear sampling is a measurement method that a LiDAR sensor samples points non-linearly. For example, Velodyne VLS-128-AP and Velodyne VLP-32C can perform non-linear sampling. This sampling tackles the problem that the density of point cloud becomes sparse at a far place. However, the density of point cloud at a near place becomes sparser than linear sampling.

The above methods are expected to reduce the amount of sharing point cloud with high accuracy of recognition, but there are several problems. Semantic segmentation and resampling can specify an important part of raw sensor data such as an object group and feature points. However, adding a new process before a transmission makes discussion complicated, which has to consider processing time and the effect on the recognition process. On the other hand, non-linear sampling needs help to perceive a near place, which may result in a larger or equal sensor data rate of high-resolution linear sampling Considering this trade-off relation, sharing the whole raw sensor data is chosen in order to avoid this complicated discussion.

3.2 Vehicle behavior

In this section, a condition for safe overtaking is discussed from the viewpoint of vehicle behavior. In [67], it is said that preventable accidents that can be predicted rationally must not be caused in ODD of automated vehicles. Moreover, in [57], it also says that automated driving vehicles should prevent foreseeable and preventable accidents under their ODD as beforementioned. From these rules, collision with the oncoming vehicle that can be predicted by LiDAR sensors should be prevented in this overtaking scenario. To achieve this goal from the viewpoint of vehicle behavior, firstly, this analysis focused on overtaking movement and braking. The braking movement is considered for an emergency case where the ego vehicle and the oncoming vehicle have to brake during the overtaking to prevent the collision. The overtaking movement is considered to check whether the ego vehicle ensures a driving path for safe overtaking or not. This movement ensures no collision with the blocking and the oncoming vehicles during the overtaking. The following paragraphs explain the details.

To ensure no collision in an emergency case, a braking model is defined .

$$l_{\text{brake}} = \frac{V^2}{2 \times g \times (\mu_{\text{brake}} + s) \times 3.6^2}. \tag{3.1}$$

Eq. 3.1 is a braking distance calculated from a vehicle velocity. V is velocity (km/h), g is acceleration due to gravity (9.81 m/s^2)、 μ_{brake} is mean coefficient of friction, s is roadway grade. The friction values are obtained from measurements on a wet, but clean road surface. the coefficient of friction is not constant in that it increases during braking as velocity decreases. Therefore, a mean value is applied for the given velocity. Moreover, the coefficient of friction is also dependent on whether the road is curved or straight. Considering the expense of determining the coefficient of friction, a calculation method of braking distance is changed to the traditional calculation method based on behavioral recordings and measurements from braking trials. From a large-scale measurement program, the following method is adopted for calculating braking distance along a level road [68].

$$d_0 = 0.039 \times \frac{V^2}{a} \tag{3.2}$$

where V is velocity (km/h), a is deceleration (m/s^2). Generally, this braking distance can be classified into the emergency type and comfortable type by changing deceleration. When a driver notices an unexpected object on a road, emergency braking occurs with a deceleration of more than 4.5 m/s^2. In usual cases, almost all drivers execute braking with a deceleration of more than 3.4 m/s^2. This deceleration enables a driver to keep the vehicle in a lane without losing control when braking on a wet roadway. Therefore, 3.4 m/s^2 is regarded as being a comfortable rate of deceleration. Since comfortable braking is desirable to provide comfortable driving in automated vehicles, the braking model is described by substituting $a = 3.4\text{m/s}^2$ in Eq. 4.3.

The reaction time from noticing the oncoming vehicle to braking the ego vehicle is also an important factor in the braking model. When drivers expected to apply their brakes, several works showed that the median reaction time was 0.66 sec with 10% using 1.5 sec or longer, 0.64 sec as the average reaction time with 5% using 1 sec or longer, and the values of brake reaction time ranged from 0.4 to 1.7 sec [69, 70, 71, 72]. On the other hand, when drivers did not expect their brakes, the response times got increased by 1 sec or more [70]. However, in automated driving vehicles, electronic control units can control in milliseconds. Therefore, the brake reaction time is regarded as negligible in this scenario. For simplicity, The braking model of the oncoming vehicle is assumed to be the same braking model. Since both the ego vehicle and the oncoming vehicle have to avoid the collision in this scenario, the required braking distance becomes $2d_0$.

Ensure the braking distance is not enough to overtake the blocking vehicle because the space for the driving path of overtaking is not considered. Therefore, a driving path for overtaking is defined. The driving path is shown in Fig. 3.2 as a black arrow. This driving path is designed to avoid the collision with the blocking vehicle so that the ego vehicle has to turn two times. For example, if we wanted to describe this driving path very simply, it can be described by four quadrants. However, this curve design does not consider vehicle dynamics and the following paragraphs introduce the design of the driving path.

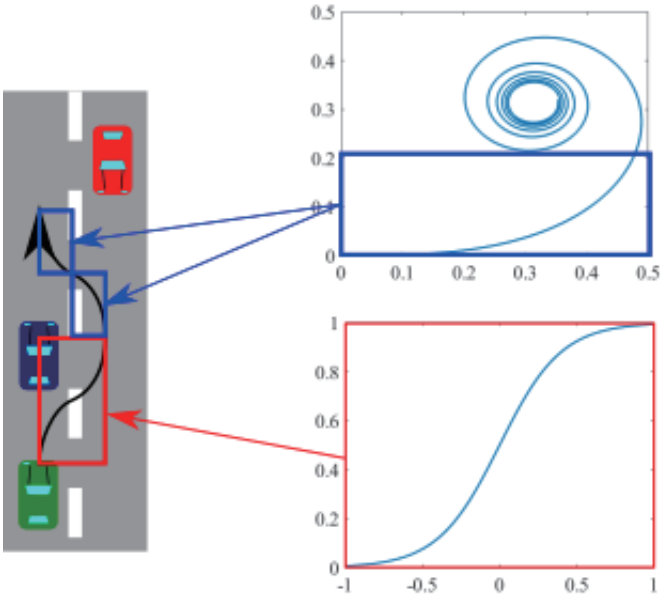

Figure 3.2: The driving path of overtaking and the two types of curves for approximation.

$$\begin{aligned} x(t) &= \int_0^t \cos \frac{A\theta^2}{2} d\theta, \\ y(t) &= \int_0^t \sin \frac{A\theta^2}{2} d\theta. \end{aligned} \tag{3.3}$$

The clothoid described as Eq. (3.3) is one of the curves which considers vehicle dynamics and is appropriate for curving driving paths, where A is the clothoid parameter. The clothoid is defined as a trajectory that meets $RL = A^2$, where R is a radius of curvature and L is the length of the curve. Curvature κ of the clothoid at t can be calculated as $\kappa = At$. The reason why the clothoid is appropriate is that the curvature of the clothoid reflects comfortable vehicle handling. In general, when a vehicle enters into a curve, a driver has to turn a steering wheel along the curve. If the curving driving path is generated as four quadrants, a vehicle entering this driving path has to turn a steering wheel quickly. This is because there is a curvature gap between a straight line and a quadrant, which is not friendly to drivers. On the other hand, if a part of the clothoid from $t = 0$ is used as shown in Fig. 3.2, a driver does not have to turn a steering wheel quickly because curvature at $t = 0$ is 0. Moreover, since κ increases linearly from $\kappa = 0$ it is enough to turn at a constant rotation. For example, in Japan, if there is a sharp curve, it is recommended to put the clothoid before the sharp curve [73].

Although the clothoid is appropriate to design curving driving paths in terms of linearly increasing curvature, it is hard to handle analytically. Therefore, the sigmoid curve is used to analyze the driving path easily in our simulation. The characteristics of the sigmoid curve

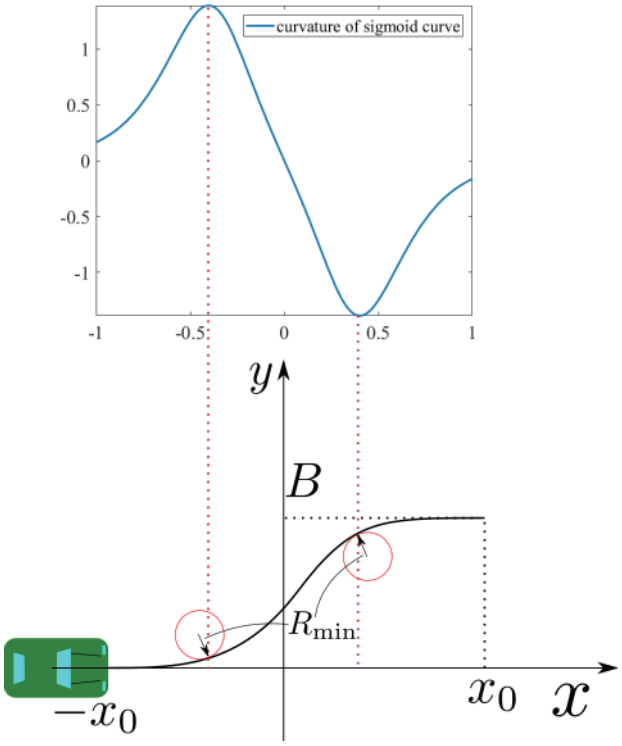

Figure 3.3: The parameters x_0, B, R in the sigmoid curve under $a = 5$ and the location of the minimum curvature radius.

are that it is easier to configure and compute than the clothoid [74].

$$y(x) = \frac{B}{1 + \mathrm{e}^{-ax}}. \tag{3.4}$$

The function of the sigmoid curve and its parameters B, a are shown in Eq. (3.4). The way to construct the driving path with the sigmoid curve is shown in Fig. 3.2. In other words, the driving path consists of two sigmoid curves that are mirror symmetry.

In order to configure the sigmoid curve, it is necessary to determine B, a, x_0 parameters. The parameter B depends on road width. In this driving path, the ego vehicle is assumed to move from the center of the lane to the center of the neighbor lane by using the function of lane centering, and returns to the first lane. From this assumption, B is equal to the width of a single lane. The parameter a determines the curvature of the sigmoid curve. In order to determine a, this analysis considers a slip and constructs the sigmoid curve that does not cause slip at a minimum curvature radius that is the sharpest point in the curve as shown in Fig. 3.3. The judgment of the slip is based on the following formula.

$$\frac{mv^2}{R} \lessgtr \mu mg \begin{cases} \text{slip: } \dfrac{mv^2}{R} > \mu mg \\ \text{safe: otherwise} \end{cases} \tag{3.5}$$

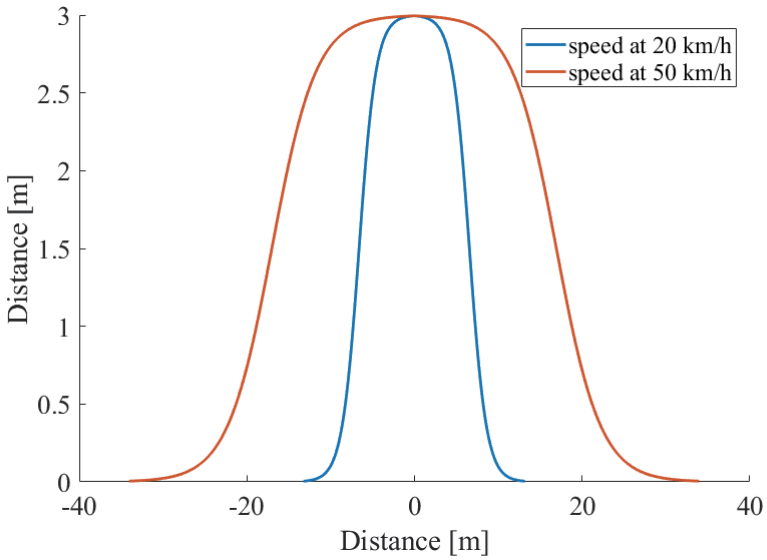

Figure 3.4: The examples of two driving paths where the duration to complete the overtaking is 5 sec.

where m is the mass of a vehicle, v is the velocity of a vehicle, R is a curvature radius at a point where a vehicle places, μ is a coefficient of static friction and g is gravity acceleration. Since it is assumed that the ego vehicle drives along the path at a constant velocity v, the minimum curvature radius that does not make the ego vehicle slipping is $R_{\text{min}} = v^2/\mu g$ from Eq. (3.5). The final parameter x_0 in Fig. 3.3 determines the length of the sigmoid curve. The length is determined by the duration to complete the overtaking that is set in advance. Fig. 3.4 shows the examples of the 5 sec driving path at 20 km/h and 50 km/h. From the figure, it is shown that when vehicle velocity gets low, the slope of the driving path gets steep. This can be explained by the definition of R_{min}. In other words, a vehicle driving at a low velocity can turn sharply without the slip.

To compare with the distance required by the braking, it is necessary to derive the distance required for the overtaking driving path. Since the oncoming vehicle drives on the neighbor lane, the ego vehicle has to finish overtaking by the time when the oncoming vehicle arrived at the collision point. Fig. 3.5 shows both driving paths from the start point to the collision point, where V is the velocity of the vehicle, t_{o} is the duration to complete the overtaking and x_0 is shown in Fig. 3.3. In this collision discussion, the vehicles are regarded as points. The collision occurs when the ego vehicle moves to the center of the neighbor lane to overtake the blocking vehicle. Since the driving path is a mirror symmetry curve, when the ego vehicle arrives at the center of the neighbor lane, the oncoming vehicle moves for $t_{\text{o}}/2$. Therefore, the distance required for the overtaking driving path becomes $Vt_{\text{o}}/2 + 2x_0$.

The above discussion leads to combining the distance required for the driving path and the comfortable braking. Fig. 3.6 shows the distance required for the comfortable braking and for the three driving path cases. It is shown that the driving path requires a larger distance

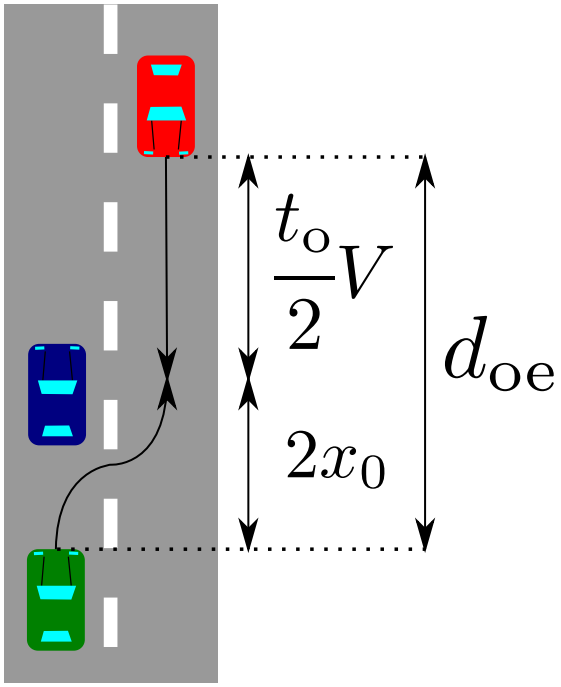

Figure 3.5: The distance that the ego and the oncoming vehicle have moved by the collision of both vehicles.

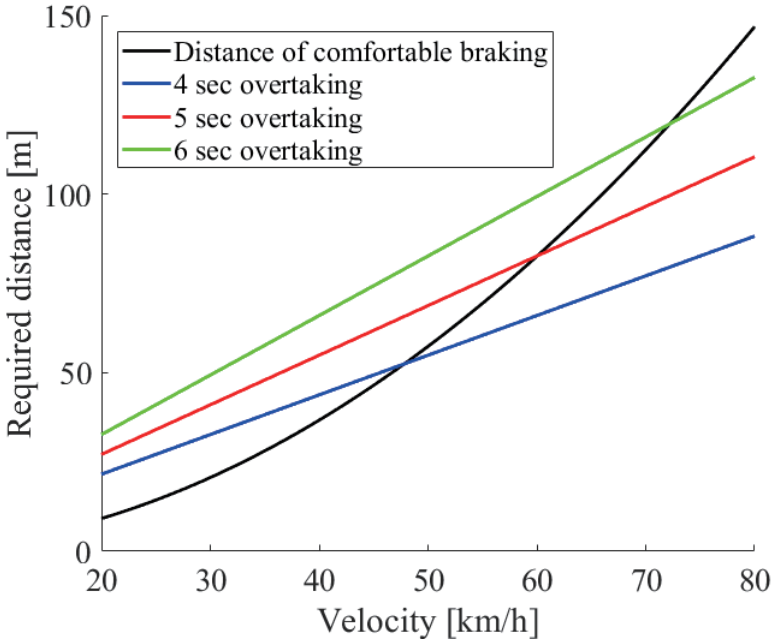

Figure 3.6: The distance required for the driving path and the comfortable braking.

than the comfortable braking distance at a low velocity, and it is reversed at a high velocity. Therefore, considering the driving path is important especially at the low velocity. Namely, the required distance d_{req} can be formulated as follows.

$$d_{\mathrm{req}} = \max\left(2 \times 0.039 \times \frac{V^2}{3.4},\ \frac{Vt_{\mathrm{o}}}{2} + 2x_0\right). \tag{3.6}$$

3.3 Recognition process and derivation of required sensor data rate

This section shows the details of the recognition process and the required sensor data rate by integrating the vehicle behavior and recognition process. In general, object recognition can be classified into two cases. One is specific object recognition. This recognition tries to classify an object into a specific object. The other is general object recognition. In contrast to the former recognition, this recognition tries to classify an object into a generic object. Since there are only vehicles in the assumed scenario, specific object recognition is adopted, and the recognition target is called the target vehicle. In this case, the ego vehicle wants to prevent collision with the oncoming vehicle so that the oncoming vehicle becomes the target vehicle. The recognition part consists of three phases. The first phase is the simulation of LiDAR sensor data in the virtual environment, and clustering point cloud about the target vehicle. The second phase is the extraction of feature points from the clustered points. The final phase is the decision of recognition. The following paragraphs explain the details of each phase.

In the first phase, regarding lasers from a LiDAR sensor as geometric optics, ray-tracing simulation of LiDAR sensor data is adopted. In order to implement ray tracing easily, objects such as vehicles, buildings, and roads consist of triangle meshes. From this setting, a point $\mathbf{p}$ on a triangle mesh can be described with three-position vectors $\mathbf{p}_1$, $\mathbf{p}_2$ and $\mathbf{p}_3$ and two parameters u, v as the following formula.

$$\mathbf{p} = (1 - u - v)\mathbf{p}_1 + u\mathbf{p}_2 + v\mathbf{p}_3. \tag{3.7}$$

Furthermore, the point $\mathbf{p}$ can be also described by a normalized direction vector $\mathbf{d}$ departing from the laser source $\mathbf{O}$ to $\mathbf{p}$.

$$\mathbf{p} = \mathbf{O} + t\mathbf{d}. \tag{3.8}$$

The direction of $\mathbf{d}$ is determined by the departure angle from the LiDAR sensor. Since the laser propagates three-dimension space, the departure angle can be described by azimuth angle ϕ and elevation angle θ.

$$\mathbf{d} = \begin{bmatrix} \cos\phi\cos\theta \\ \sin\phi\cos\theta \\ \sin\theta \end{bmatrix} \tag{3.9}$$

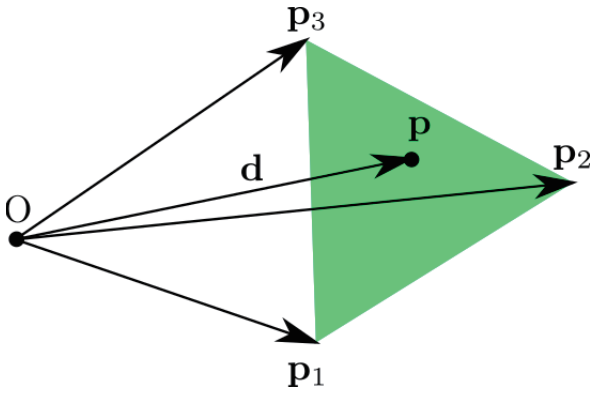

Figure 3.7: A point on a triangle mesh and the relation of position vectors and a direction vector.

The relation of these vectors are shown in Fig. 3.7.

When a point is on the mesh, parameter u and v have to meet $0 \leq u,\ v \leq 1$ and $0 \leq u+v \leq 1$. On the other hand, parameter t has to meet $0 \leq t$. In order to confirm whether these conditions are met or not, these parameters are solved by combining Eq. (3.7) and Eq. (3.8) and adopting Cramer's rule.

$$
\begin{aligned}
(1-u-v)\mathbf{p}_1 + u\mathbf{p}_2 + v\mathbf{p}_3 &= \mathbf{O} + t\mathbf{d}, \\
\begin{bmatrix} -\mathbf{d} & \mathbf{p}_2 - \mathbf{p}_1 & \mathbf{p}_3 - \mathbf{p}_1 \end{bmatrix} \begin{bmatrix} t \\ u \\ v \end{bmatrix} &= \mathbf{O} - \mathbf{p}_1.
\end{aligned} \tag{3.10}
$$

Replacing $\mathbf{p}_2 - \mathbf{p}_1$ with $\mathbf{p}_{21}$, $\mathbf{p}_3 - \mathbf{p}_1$ with $\mathbf{p}_{31}$, and $\mathbf{O} - \mathbf{p}_1$ with $\mathbf{p}_{01}$, parameters $t,\ u,\ v$ can be solved by adopting Cramer's rule to Eq. (3.10).

$$
\begin{bmatrix} t \\ u \\ v \end{bmatrix} = \frac{1}{\left| -\mathbf{d} \quad \mathbf{p}_{21} \quad \mathbf{p}_{31} \right|} \begin{bmatrix} \left| \mathbf{p}_{01} \quad \mathbf{p}_{21} \quad \mathbf{p}_{31} \right| \\ \left| -\mathbf{d} \quad \mathbf{p}_{01} \quad \mathbf{p}_{31} \right| \\ \left| -\mathbf{d} \quad \mathbf{p}_{21} \quad \mathbf{p}_{01} \right| \end{bmatrix} \tag{3.11}
$$

where $|\cdot|$ is the determinant of a matrix.

As mentioned above, before extracting the feature points only from the target vehicle points for recognition, clustering is needed to remove irrelevant points. In this simple ray tracing algorithm, the function of linking the hit object to the laser is implemented. As a result, the LiDAR sensor in our simulation knows which object the laser is reflected from so that it is possible to select the points of the target vehicle and perform clustering easily.

In the second phase, feature points from the clustered points are extracted . When we want to describe features of point cloud data, or LiDAR sensor data, a feature descriptor is often used. Signature of Histogram of OrienTation (SHOT) and Point Feature Histogram (PFH) are the typical feature descriptors. These descriptors use a histogram to describe features around a point. In general, the calculation time of a feature descriptor depends on the

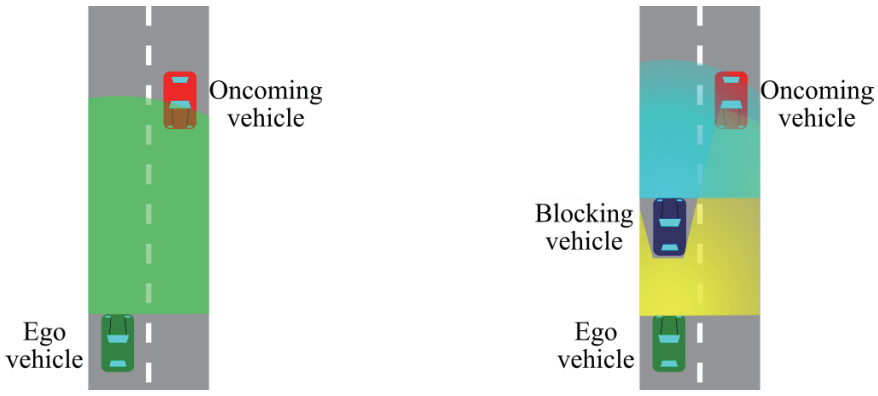

(a) Simulation with the target vehicle.

(b) Simulation with all objects

Figure 3.8: The two configurations for the recognition score.

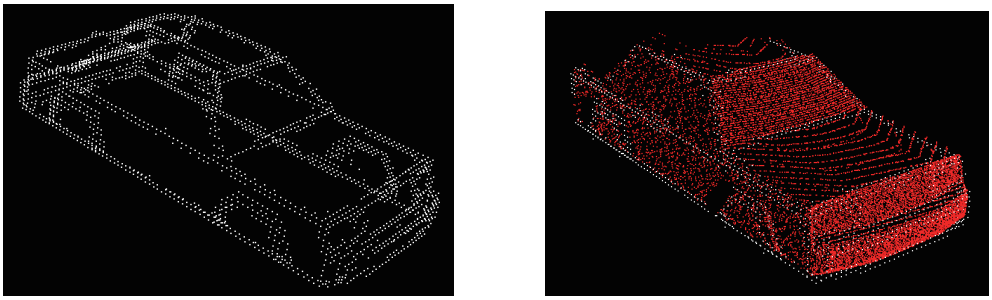

(a) The edge points extracted from the model points.

(b) The white points show the LoS edge points, and the red points show the points emitted on the target vehicle with cooperative perception.

Figure 3.9: Examples of point cloud used in the recognition process.

dimension of the descriptor. In order to avoid this complicated discussion, edge points that are a basic feature are used. Extracting edge points is performed by Principal Component Analysis (PCA) [75]. This PCA method is faster to extract edge points and more robust to noise than using Gauss map. The key point of this process is that edge points are extracted by the eigenvalues of a covariance matrix. The quantity made of the eigenvalues is called surface curvature, and it is calculated for each point. When the surface curvature exceeds a threshold, the point is regarded as an edge point. The threshold is tuned by observing the distribution of surface curvature.

The final phase is the decision of recognition. This simulation adopted model-based recognition. This recognition method is a matching problem between scene and model points. Scene points are obtained from the output of the LiDAR sensor. On the other hand, model points are prepared in advance and have enough points to describe the target vehicle and extract feature points. The process of this recognition consists of calculating feature points of the model and scene points and searching the correspondence of the feature points between

the model and scene points. If there are corresponding points, clustering with regard to corresponding points is performed.

Two points are simplified through this model-based recognition process. The first point is using not the entire scene points but the points clustered from the scene points. This extraction is performed in the first phase of ray tracing and this leads to ideal input data for recognizing the target vehicle. The second point is the decision way of recognition. A recognition score S is defined as a ratio of the number of the edge points shown in Eq. (3.12). N_{get} and N_{LOS} are the number of edge points calculated from the two configurations as shown in Fig. 3.8.

$$S = \frac{N_{\text{get}}}{N_{\text{LOS}}}. \tag{3.12}$$

The difference between these configurations is that the right configuration includes all objects, but the left configuration only includes the target vehicle as shown in Fig. 3.8. In the Fig. 3.8a case, the sensing range of the LiDAR sensor on the ego vehicle is described by the green range. This environment enables the ego vehicle to sense the target vehicle with Line-of-Sight (LoS). In Fig. 3.8b case, there are two LiDAR sensors. One is on the ego vehicle, but, on the contrary to the former case, the blue vehicle blocks the sensing as shown by the yellow range. The other is on the blue blocking vehicle that senses with LoS as same as the former case. The edge points obtained in Fig. 3.8a case are regarded as the maximum number of edge points of the target vehicle that the ego vehicle can obtain. On the other hand, the edge points in Fig. 3.8b can be obtained in two ways, that is using cooperative perception or not. Using cooperative perception, the edge points calculation is based on the yellow and blue sensing range while, without cooperative perception, it is only based on the yellow sensing range. Fig. 3.9a shows the entire edge points in the model points. Fig. 3.9b shows two points. One is the white edge points obtained under Fig. 3.8a configuration, and the other is the red points obtained under Fig. 3.8b configuration using cooperative perception. Since the red points are also obtained from a LoS place, the red and white points distribution is similar.

Counting the number of edge points is different between the two configurations. N_{LOS} in Eq. (3.12) is the number of the LoS edge points obtained in the Fig. 3.8a case. In detail, firstly, the LoS edge points of the model points are calculated by PCA edge extraction and voxelized. The resolution of the voxelization is based on an error range of a LiDAR sensor. Secondly, the edge points are moved and aligned with the target vehicle. Finally, the voxelized edge points that are LoS from the ego vehicle are extracted, and these points are called voxelized LoS edge points. On the other hand, the first process for N_{get} is the simulation of the LiDAR sensor data under the Fig. 3.8b configuration. Since this recognition focused on how much scene points have information about voxelized LoS edge points, it extracted a part of these edge points that match with the model points. As a result, N_{get} is the total number of the voxelized LoS edge points that are near to the scene points. After the calculation of N_{LOS} and N_{get}, the ratio and threshold are compared, and, when the ratio is more than the threshold, it is defined that the ego vehicle recognizes the target vehicle.

The vehicle movement part derived the required distance d_{req} to avoid a collision. Furthermore, the recognition process gives a judgment that the ego vehicle recognizes the target vehicle at a given distance. Therefore, the combination of the required distance d_{req} in

Eq. (3.6) and the recognition process derives the required sensor data rate R_{req} to avoid the collision as follows.

$$\{\overline{r_\phi},\ \overline{r_\theta}\} = \underset{\{r_\phi,\ r_\theta\}}{\arg\min}\, S\left(r_\phi,\ r_\theta \mid d_{\mathrm{req}},\ d_{\mathrm{be}}\right) > 0.9, \tag{3.13}$$

$$R_{\mathrm{req}} = \left(\left\lfloor \frac{A_\phi}{\overline{r_\phi}} \right\rfloor + 1\right) \times \left(\left\lfloor \frac{A_\theta}{\overline{r_\theta}} \right\rfloor + 1\right) \times F_{\mathrm{scan}} \times D_{\mathrm{symbol}}, \tag{3.14}$$

where S is the recognition score in Eq. (3.12), A_ϕ and A_θ are the scanning range in the azimuth and the elevation angle (degree), $r_\phi,\ r_\theta$ are the resolution of the azimuth and the elevation angle (degree), F_{scan} is scan frequency (Hz) of the LiDAR sensor, and D_{symbol} is the amount of information per one laser point (bits). Note that the required sensor data rate depends on the velocity V of the ego vehicle and the distance d_{be}. Finally, the realized maximum overtaking velocity is derived by obtaining the minimum outage capacity that exceeds the required sensor data rate, which will be introduced in the simulation section.

Fig. 3.10 shows the required sensor data rate with the two options such as cooperative perception and driving path. The solid (dotted) line with square markers shows the minimum required sensor data rate to overtake with (not) using cooperative perception and not considering the driving path. The solid (dotted) line with circle markers considers the driving path with (without) cooperative perception. From the figure, firstly, it is shown that all required sensor data rates rapidly increase. This rapid increase is due to the laser density, or the resolution of the LiDAR sensor, which gets rapidly sparse at a far place. This means that the required resolution of the LiDAR sensor gets exponentially increased as the target vehicle goes far. In the case of no cooperative perception, since the blocking vehicle interrupts the sensing, a much higher resolution is required so that the required sensor data rate increases further rapidly. Secondly, there is a difference in the curves between considering the driving path or not. This reflects the result of 5 sec overtaking shown in Fig. 3.6 so that no difference is seen at more than 60 km/h. Fig. 3.11 shows the required sensor data rate with $d_{\mathrm{be}} = 5,\ 10,\ 15$ m and 5 sec overtaking. In the case of using cooperative perception, as d_{be} gets larges, the required sensor data rate gets small at a fixed velocity. When d_{be} is large, the blocking vehicle gets near to the target vehicle. This allows the blocking vehicle to recognize the target vehicle with a low-resolution LiDAR sensor. On the other hand, the required sensor data rate in no cooperative perception depends on two factors, which leads to a complicated result. One is the distance d_{oe}. When d_{oe} is large with the presence of the blocking vehicle, it is easy for a high-resolution LiDAR sensor on the ego vehicle to see the shape of the whole target vehicle under a small sensing range, which obviously has a limit for the recognition. The other is distance d_{be}. As the blocking vehicle gets near to the ego vehicle, the blocking vehicle blocks a large part of the range that sees the target vehicle. When the target vehicle is very close to the ego vehicle, the ego vehicle can see the target vehicle with LoS. Since the LiDAR sensor is on the roof, a large part of the blocking vehicle does not block the sensing in the case of a very near location. From Fig. 3.11, the required sensor data rate gets high from $d_{\mathrm{be}} = 15$ m to $d_{\mathrm{be}} = 10$ m, but it gets low from $d_{\mathrm{be}} = 10$ m to $d_{\mathrm{be}} = 5$ m. This result tells us that sensing with no cooperative perception on a two-lane road heavily depends on

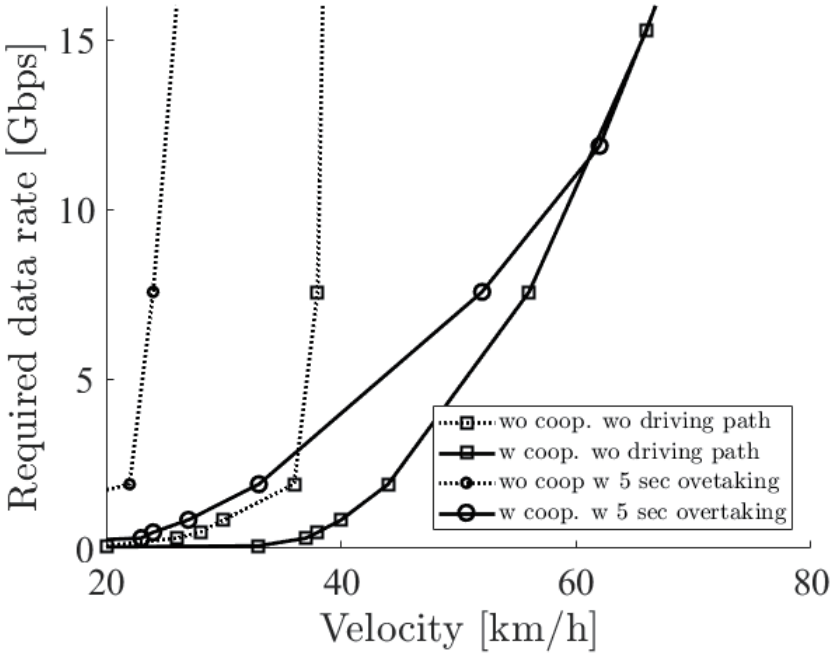

Figure 3.10: The required sensor data rate with the options of cooperative perception and driving path when the distance between the ego vehicle and the blocking vehicle is 5 m.

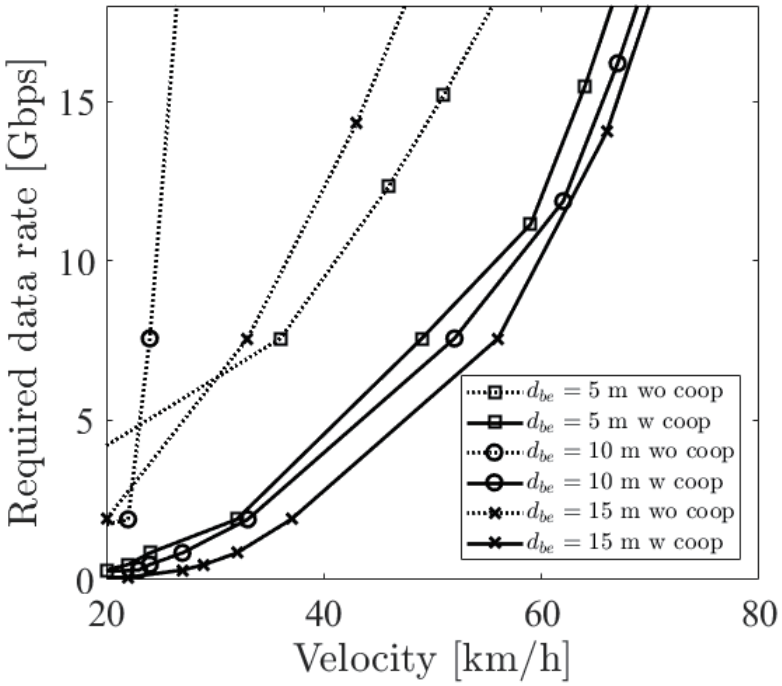

Figure 3.11: The required sensor data rate with the options of cooperative perception and 5 sec overtaking when the distance between the ego vehicle and the blocking vehicle is 5, 10, and 15 m.

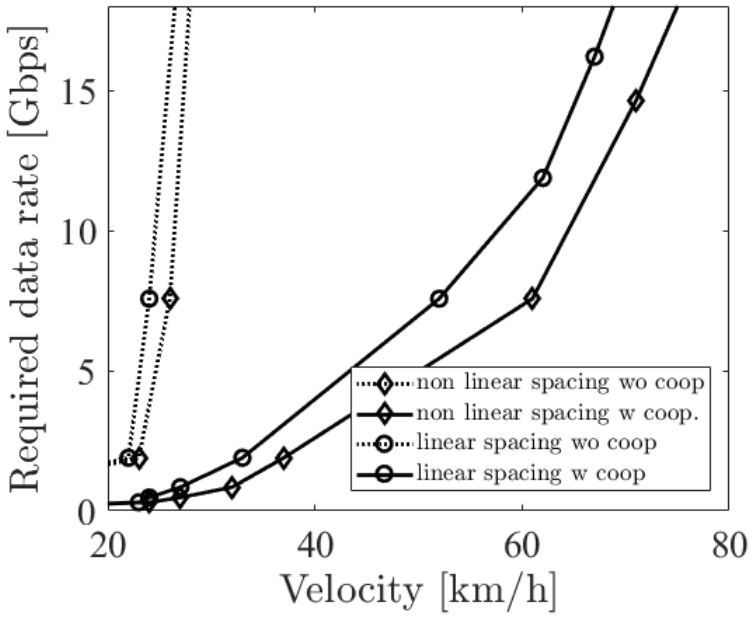

Figure 3.12: The required sensor data rate with the options of linear and non-linear spacing LiDAR sensor at $d_{\text{be}} = 10$ m.

many factors such as the size and the location of vehicles, which will make the requirements complicated. On the other hand, sensing with cooperative perception simply depends on d_{be}.

Fig. 3.12 shows the required sensor data rate using two different LiDAR sensors. One is a linear spacing LiDAR sensor and the other is a non-linear spacing LiDAR sensor. In the case of linear spacing, the LiDAR sensor has an equally spaced elevation angle resolution such as Velodyne VLP-16. On the other hand, a non-linear spacing LiDAR sensor such as Velodyne VLP-32 has a dense and sparse spacing part. This analysis fixed the number of lasers between the two LiDAR sensors. The details of non-linear spacing are shown in Table. 3.1. The figure shows that a non-linear spacing LiDAR sensor has a better ability to recognize a far object. However, notice that non-linear spacing provides sparse information about a near object.

3.4 Millimeter-wave V2V communications with height diversity

Since cooperative perception needs wireless communication, this section discusses Vehicle-to-Vehicle (V2V) communications. Firstly, V2V channel models for both conventional and millimeter-wave communications under moving vehicles are introduced. In [76] and [77], the authors measured 5 and 60 GHz and performed modeling of the measured data. As a result, it is shown that the two-ray ground reflection model is suited for the V2V channel. Therefore, the two-ray ground reflection model is adopted as a large-scale path loss model in the sim-

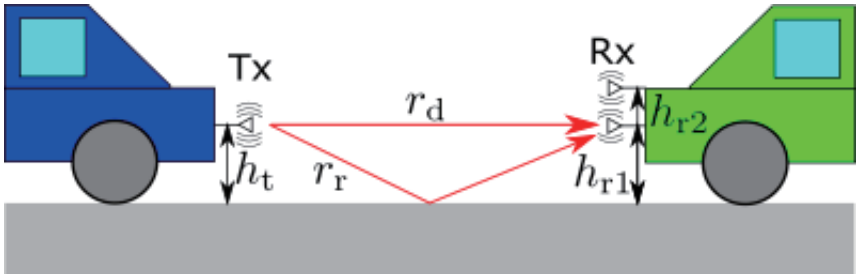

Figure 3.13: V2V two-ray ground reflection channel model.

ulation as shown in Fig. 3.13. The additional characteristics of this model are that vibrating of both transmitter and receiver due to vehicle movement have an effect on a small scale fading [77]. To avoid the fading in the driving environment, in [78], it is shown that, when one vehicle with multiple receivers is chasing the other vehicle with a transmitter, diversity gain is maximized by a vertically displaced antenna rather than a horizontally displaced antenna. In [79], the authors analyzed the outage capacity under the 60 GHz two-rays ground reflection model that follows the Rayleigh and the Rice distribution. They derived theoretically that height diversity provides large improvements rather than horizontal space diversity. In [80], the author derived that the antenna space for height diversity should be more than 10 cm. Considering these works, this analysis assumed height diversity at the receiver and discussed how much height diversity improves the outage capacity. Since 99.99% reliability is required in the cooperative perception, the improvement is estimated by 0.01% outage capacity [9]. Moreover, the best antenna space is derived to improve the outage capacity among 5, 30, and 60 GHz. The reason why 30 GHz and 60 GHz are chosen is due to allocated frequency bands for millimeter-wave communications. 27, 37, 39, 60, 70, 80, and 90 GHz bands are candidates for millimeter-wave communications. Although the 60 GHz band has oxygen absorption that severely limits communication range, the 60 GHz band is attractive in terms of a global unlicensed band among these bands [81]. On the other hand, 28 GHz is allocated for 5G and 28 GHz is approximated as 30 GHz for simplicity.

Firstly, the basic characteristics of this channel model are analyzed . As described above, this channel model can be separated into the effect of two-ray ground reflection and antenna vibration. The received power P_{r} under the two-rays ground reflection is formulated as follows.

$$P_{\mathrm{r}} = \frac{P_{\mathrm{t}}}{L(r_{\mathrm{d}})} \left| \sqrt{G_{\mathrm{d}}} \left(\frac{\lambda}{4\pi r_{\mathrm{d}}} \right) + \sqrt{G_{\mathrm{r}}} \left(\frac{\lambda}{4\pi r_{\mathrm{r}}} \right) \Gamma \mathrm{e}^{-\mathrm{j}\{k(r_{\mathrm{d}} - r_{\mathrm{r}})\}} \right|^2, \tag{3.15}$$

$$\text{where} \quad r_{\mathrm{d}} = \sqrt{d_{\mathrm{be}}^2 + (h_{\mathrm{r}} - h_{\mathrm{t}})^2},$$
$$r_{\mathrm{r}} = \sqrt{d_{\mathrm{be}}^2 + (h_{\mathrm{r}} + h_{\mathrm{t}})^2},$$

where P_{t} is transmission power, G_{d} and G_{r} are the antenna gains for direct and reflected wave, r_{d} and r_{r} are the optical path length for direct and reflected waves, $L(r_{\mathrm{d}})$ is the absorption

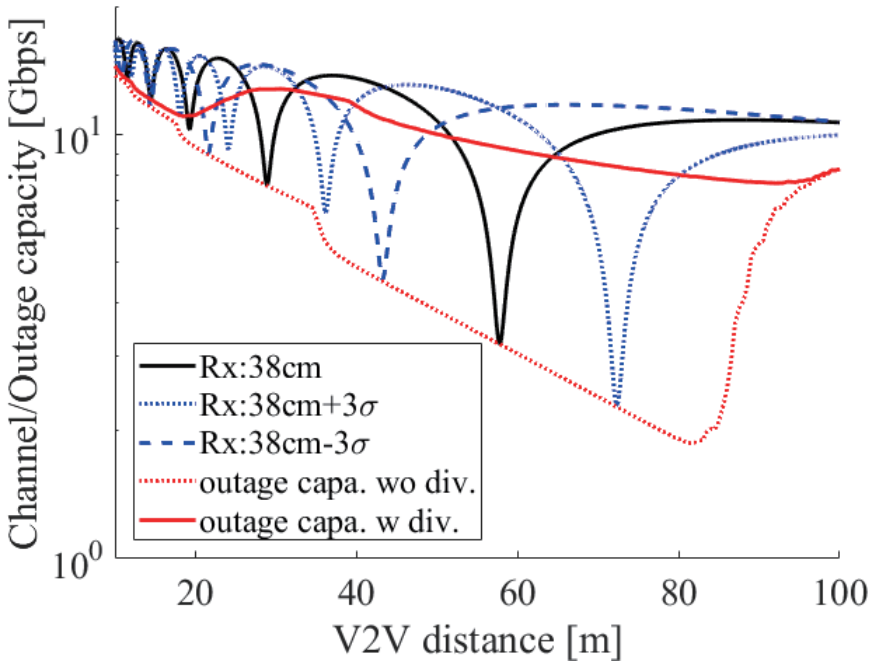

Figure 3.14: The channel capacity under the two-ray ground reflection model with and without the antenna vibration and the 0.01% outage capacity with and without height diversity at 60 GHz.

factor at 60 GHz by oxygen as 15 dB/km, λ is wavelength, k is $2\pi/\lambda$, Γ is the complex reflection coefficient. When the antenna vibration caused by the motor on the vehicle is adopted to this channel model, it changes r_d and r_r. In [77], the authors modeled this antenna vibration by Gaussian distribution $\mathcal{N}_\mathrm{r}\left(0,\ \sigma_0^2\right)$ where σ_0 is 0.0319 m. This vibration causes a shift of all fading points, and all receiving places have a possibility to encounter strong fading. To avoid strong fading, height diversity that uses selection diversity is adopted. In this case, the receivers vibrate by the same motor so that they follow the same distribution as Eq. (3.16) and (3.17).

$$h_\mathrm{tv} = h_\mathrm{t} + \delta_\mathrm{t} \quad \text{where} \quad \delta_\mathrm{t} \sim \mathcal{N}_\mathrm{t}\left(0,\ \sigma_0^2\right). \tag{3.16}$$

$$\begin{aligned} h_\mathrm{rv1} &= h_\mathrm{r1} + \delta_\mathrm{r} \\ h_\mathrm{rv2} &= h_\mathrm{r2} + \delta_\mathrm{r} \end{aligned} \quad \text{where} \quad \delta_\mathrm{r} \sim \mathcal{N}_\mathrm{r}\left(0,\ \sigma_0^2\right). \tag{3.17}$$

Finally, the 0.01% outage capacity C_out is calculated under the height diversity.

$$\begin{aligned} P(c(h_\mathrm{r}) < C_\mathrm{out}(h_\mathrm{r})) &= 0.01\%, \\ \text{where} \quad c &= W \log\left(1 + P_\mathrm{r}/N\right). \end{aligned} \tag{3.18}$$

W is bandwidth and N is the total received power of noise.

Fig. 3.14 shows the above discussion in the case of 60 GHz. The black solid line shows the basic characteristic of the two-ray ground reflection model that there is no vibration. The

blue dotted and dashed lines show the moment of vibrating to 3σ and -3σ. The lines show that the strong fading points are shifted to the left and the right. The red dotted line shows the 0.01% outage capacity under no height diversity, and shows that the fading occurs at an arbitrary V2V distance. In particular, there are sharp drops at 18 and 35 m and there is a sharp rise at 84 m. These sharp changes are due to antenna vibration. For example, the fading point at 57 m moves ±21 m and at 28 m moves ±10 m in the case of $\pm 3\sigma$ vibration. Considering that a shift of $\pm 3\sigma$ happens at around 99.7% and the shift in 0.01% outage capacity is larger than the shift of $\pm 3\sigma$, the sharp drop and rise are a reasonable result. The red solid line shows the outage capacity with height diversity. Although it is improved from no diversity, the outage capacity gradually changes up and down. The main reason for this change is that there are some places where both receivers encounter strong fading.

To improve this outage capacity with height diversity, it is necessary to solve the changing up and down of the outage capacity. The following analysis consists of two parts. The first analysis focuses on the best receiving antenna space for the second receiving antenna. In this analysis, carrier frequency, inter-vehicle distance, the height of a transmitting antenna, and the height of the first receiving antenna are given. The second analysis focuses on the relation between a communication range and the number of receiving antennas. This analysis firstly focuses on the difference of the phase difference between the direct wave path and the reflected wave path. When the height diversity works well, this phase difference is around π as the following formula.

$$\frac{2\pi}{\lambda}\{(r_{\mathrm{d}2} - r_{\mathrm{r}2}) - (r_{\mathrm{d}1} - r_{\mathrm{r}1})\} \equiv \pi \pmod{2\pi}, \tag{3.19}$$

where $r_{\mathrm{d}1}$ ($r_{\mathrm{d}2}$), $r_{\mathrm{r}1}$ ($r_{\mathrm{r}2}$) are the length of the direct and reflected paths from the transmitter whose height is h_{tv} to the lower (upper) receiver whose height is $h_{\mathrm{rv}1}$ ($h_{\mathrm{rv}2}$) in Eq. (3.17). Using the approximation of $\sqrt{1+x} \approx 1 + x/2 \quad (1 \gg |x|)$, Eq. (3.19) can be described as follows.

$$\begin{aligned}
&\frac{2\pi}{\lambda}\{(r_{\mathrm{d}2} - r_{\mathrm{r}2}) - (r_{\mathrm{d}1} - r_{\mathrm{r}1})\} \\
&\approx -\frac{4\pi}{d\lambda} h_{\mathrm{tv}} (h_{\mathrm{rv}2} - h_{\mathrm{rv}1}) \\
&= -\frac{4\pi}{d\lambda}(h_{\mathrm{t}} + \delta_{\mathrm{t}}) (h_{\mathrm{r}2} - h_{\mathrm{r}1}) \quad (= \Phi(\delta_{\mathrm{t}})),
\end{aligned} \tag{3.20}$$

where d is the inter-vehicle distance. From the above approximation, it is shown that variables in the difference are only δ_{t}. This difference is expressed as $\Phi(\delta_{\mathrm{t}})$. When there is no vibration, which is $\delta = 0$, the solutions h_{n} of Eq. (3.20) are described as follows.

$$h_{\mathrm{n}} = h_{\mathrm{r}2\mathrm{n}} - h_{\mathrm{r}1\mathrm{n}} \quad \text{such that} \quad \Phi(0 \mid h_{\mathrm{n}}) = -\frac{4\pi}{d\lambda}(h_{\mathrm{t}} + 0)h_{\mathrm{n}} = (2n+1)\pi. \tag{3.21}$$

To choose the best solution $h_{\mathrm{n}}^{\mathrm{best}}$ among the solutions h_{n}, it is necessary to estimate Φ where δ_{t} ranges from $-3\sigma_0$ to $3\sigma_0$, which falls within around 99.7%. This is because, recalling that the

goal is to solve the changing up and down of the outage capacity due to the antenna vibration, it is necessary to select one solution that the phase difference Φ does not change more than $\pm\pi/2$ with a large possibility. Since $\Phi(0 \mid h_{\mathrm{n}}) - \Phi(-3\sigma_0 \mid h_{\mathrm{n}})$ and $\Phi(3\sigma_0 \mid h_{\mathrm{n}}) - \Phi(0 \mid h_{\mathrm{n}})$ are same, the $h_{\mathrm{n}}^{\mathrm{best}}$ is chosen by solving $\Phi(0 \mid h_{\mathrm{n}}) - \Phi(-3\sigma_0 \mid h_{\mathrm{n}})$.

The second analysis is about the communication range. In the first analysis, the best receiving antenna space under the fixed inter-vehicle distance has been analyzed. However, it is not realistic to equip receiving antennas for each inter-vehicle distance, which will require too many antennas. In order to solve this problem, the second analysis derived the range of the inter-vehicle distance where the height diversity works well and minimized the number of receiving antennas. Under the $h_{\mathrm{n}}^{\mathrm{best}}$, the valid communication range R is defined as the range that the difference of Φ is from 115° to 245° as follows. The reason of choosing this range comes from $(1 + \cos(\pm 65°)) = 1/2$.

$$
\begin{aligned}
R_{\mathrm{min}} &= \frac{4\pi}{2\pi\frac{180+65}{360}\lambda} h_{\mathrm{t}} h_{\mathrm{n}}^{\mathrm{best}} \\
&= \frac{144}{49\lambda} h_{\mathrm{t}} h_{\mathrm{n}}^{\mathrm{best}}. \qquad (3.22) \\
R_{\mathrm{max}} &= \frac{4\pi}{2\pi\frac{180-65}{360}\lambda} h_{\mathrm{t}} h_{\mathrm{n}}^{\mathrm{best}} \\
&= \frac{144}{23\lambda} h_{\mathrm{t}} h_{\mathrm{n}}^{\mathrm{best}}. \qquad (3.23)
\end{aligned}
$$

From Eq. (3.22) and (3.23), it shows that, as the antenna space $h_{\mathrm{n}}^{\mathrm{best}}$ gets large, the minimum and maximum effective communication distance get large. Furthermore, as the wavelength λ gets short, these distances get also large.

For example, Fig. 3.15 plots the several cases of the 0.01% outage capacity at 60 GHz. The black line shows the outage capacity without height diversity. The red and blue lines show the outage capacity with 10 and 20 cm antenna space. The red and blue two-headed arrows show the effective communication range in the case of 10 and 20 cm antenna space. Fig. 3.15 shows that the outage capacity in the effective range is better than the outside. Although there are several solutions to Eq. (3.19) at 10 cm antenna space in $d < 22$ m and at 20 cm antenna space in $d < 48$ m, rapid fluctuation of the difference of the phase difference degrades the outage capacity. On the other hand, since the difference gets stable at more than π in $d > 48$ m at 10 cm antenna space and in $d > 95$ m at 20 cm antenna space, the improvement from no height diversity gradually decreases.

The above analysis concludes that the antenna space determines short-range or long-range communication. The statistics show that the average speed on highways is about 70 km/h and on prefectural roads is about 30 km/h [82]. Moreover, the two-second rule is adopted to decide the average V2V distance. This rule derives an average distance on prefectural roads which is 17 m, and on highways which is 39 m. Based on these average distances, this thesis proposed two additional receivers for height diversity that support the above two

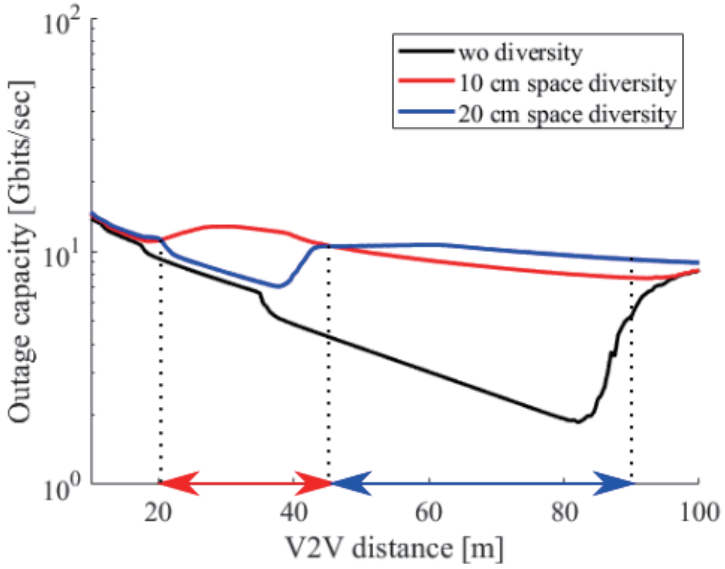

Figure 3.15: The 0.01% outage capacity with height diversity under h_{t1}, h_{r1} = 0.38 m, h_{r2} = 0.48 m and h_{r2} = 0.58 m, and without diversity at 60 GHz.

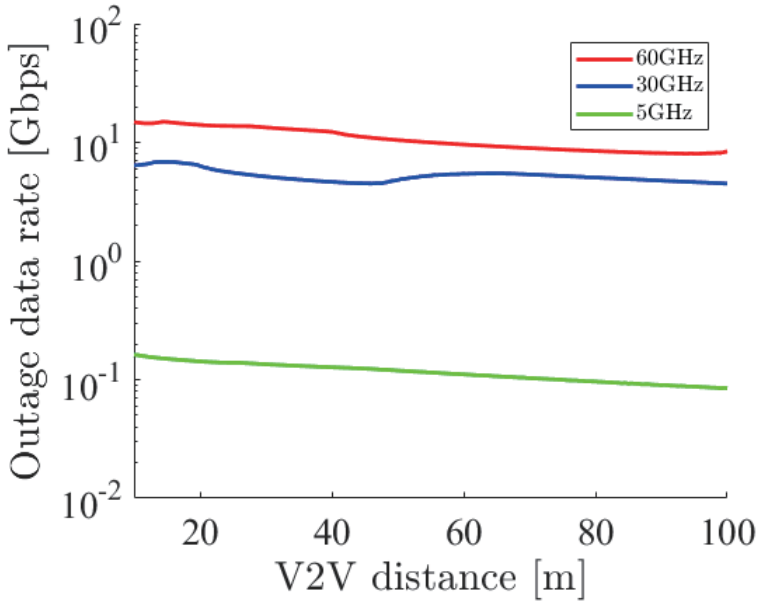

Figure 3.16: The 0.01% outage capacity with height diversity for 5, 30 and 60 GHz.

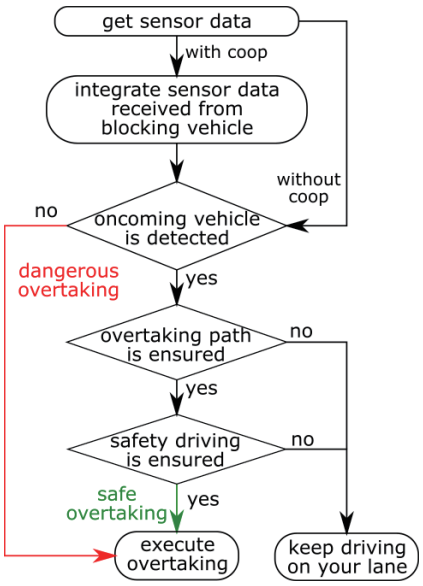

(a) Block diagram of safe overtaking.

Algorithm 1 Safe overtaking

1: initialize the point cloud buffer PC_{buffer}.
2: set the resolution $(r_\phi,\ r_\theta)$ of LiDAR sensors.
3: calculate sensor data rate R_{sensor} by using $F_{\text{scan}},\ D_{\text{symbol}}$.
4: set d_{be}, d_{oe}, and V.
5: calculate a outage capacity C_{out} under d_{be}.
6: **if** $C_{\text{out}} > R_{\text{sensor}}$ **then**
7: $\quad f_{\text{coop}} = \text{true}$
8: **else**
9: $\quad f_{\text{coop}} = \text{false}$
10: **end if**
11: calucalte LiDAR sensor data PC_{ego} obtained by the ego vehicle.
12: **if** $f_{\text{coop}} == \text{true}$ **then**
13: $\quad$ calucalte LiDAR sensor data PC_{blocking} obtained by the blocking vehicle.
14: $\quad$ add to the buffer $PC_{\text{buffer}} \mathrel{+}= PC_{\text{blocking}}$.
15: **end if**
16: calculate the recognition score $S(PC_{\text{buffer}})$.
17: **if** $S > 0.9$ **then**
18: $\quad$ **if** $d_{\text{req}} < d_{\text{oe}}$ **then**
19: $\quad\quad$ execute safe overtaking.
20: $\quad$ **else**
21: $\quad\quad$ keep driving on the lane due to the risk of a collision.
22: $\quad$ **end if**
23: **else**
24: $\quad$ execute a dangerous overtaking.
25: **end if**

(b) Algorithm of safe overtaking.

Figure 3.17: Description of the whole process in the simulation.

values, which means that there are three receivers. At 60 GHz, the first receiver is set at 5 cm space whose effective range is from 11 m to 24 m, and the second receiver is set at 12 cm space whose effective range is from 27 m to 57 m. In the case of 30 GHz, 10 cm and 24 cm of space are necessary. Finally, in the case of 5 GHz, 60 cm and 144 cm of space are necessary. Fig. 3.16 shows the outage capacity at 5, 30, and 60 GHz with height diversity. Note that 5, 30, and 60 GHz use three receivers as proposed in the above discussion. The figure shows that all outage capacities have no sharp drop, and decrease linearly.

3.5 Performance of millimeter-wave V2V communications to support safe overtaking

To estimate the amount of the minimum required sensor data for the safe overtaking, the simulation is performed. The required sensor data rate is derived with each d_{be} and d_{oe}. Fig. 3.17a shows the process flow of the simulation and Fig. 3.17b shows the algorithm. Firstly, the output of the LiDAR sensors on the blocking vehicle and the ego vehicle is simulated. When the ego vehicle uses cooperative perception, it can use not only its sensor data but also the sensor data of the blocking vehicle for the recognition process. The recognition process defines that, if the recognition score described in Eq. (3.12) is more than 0.9, the ego vehicle recognizes the oncoming vehicle. The recognition score is calculated under the prepared LiDAR sensor

resolution sets of (r_ϕ, r_θ). If the ego vehicle fails to recognize the oncoming vehicle, it believes that there are no vehicles on the oncoming lane. Since the ego vehicle does not know exactly whether there are vehicles on the oncoming lane or not, this misunderstanding leads to a collision. If the ego vehicle recognizes the oncoming vehicle, then it additionally checks two factors. One is ensuring a comfortable braking distance for preventing a collision. The other is ensuring the driving path for overtaking. In this simulation, the required time for overtaking is set to 5 sec. If the ego vehicle does not pass either, it will stay on the lane. If it passes, it can overtake the blocking vehicle.

Fig. 3.18, 3.19, and 3.20 show the simulation result of $d_{\mathrm{be}} = 5,\ 10,\ 15$ m under the parameters of Table. 3.1. The horizontal axis denotes the velocity of the ego vehicle, and the vertical axis denotes the sensor data rate required for the safe overtaking and the outage capacity of each carrier frequency. The black solid and dotted lines with markers show the required sensor data rate with and without cooperative perception. Since the calculation time grows drastically at more than 8 Gbps, extrapolation is used. The green, red, and blue solid lines show the realized 0.01% outage data rate for each d_{be} at 5, 30, and 60 GHz. Fig. 3.21 shows the result of $d_{\mathrm{be}} = 10$ m with using non-linear spacing LiDAR sensors.

Considering the realized data rate and the required sensor data rate using cooperative perception, the figure shows that the maximum velocity for safe overtaking under $d_{\mathrm{be}} = 5,\ 10,\ 15$ m at 60 GHz is 66, 64, 67 km/h, at 30 GHz is 51, 49, 54 km/h. Since the realized data rate at 5 GHz is too small, the maximum velocity for safe overtaking is less than 20 km/h in all cases. In all d_{be} cases, cooperative perception using 60 GHz constantly ensures around 65 km/h for safe overtaking. In the case of using non-linear spacing LiDAR sensors, when 5, 30, 60 GHz is used for cooperative perception, the ego vehicle can safely overtake 0, 9, 7 km/h faster than using linear spacing LiDAR sensors. Although non-linear spacing LiDAR sensors improve the overtaking, the effect of providing sparse information about near objects should be noticed, especially in other driving scenarios.

For the final discussion, these results are compared with the current requirements for cooperative perception. In [7], 1 Gbps and 10 ms of max end-to-end latency are required for a higher degree of automation to prevent an imminent collision by extended sensors, or cooperative perception, which allows the maximum sensor data rate at 100 Mbps. On the other hand, in [9], 1 Gbps and 3 ms of end-to-end latency are required for collective perception of the environment, or cooperative perception, which allows the maximum sensor data rate at 3 Mbps. In our analysis, even if an automated vehicle drives at around 30 km/h, around 1 Gbps sensor data rate is required to realize safe automated driving by sharing raw sensor data. From the above comparison, although only LiDAR sensors are considered for recognition, it is shown that considering safety affects the requirements.

These results show that millimeter-wave communication has a big potential to contribute to safe overtaking and smooth traffic. Although the actual data rate will be lower than these outage data rates, millimeter-wave communication especially on 60 GHz has a large margin. Therefore, these results conclude that millimeter-wave communication had an ability to perform the safe overtaking with high velocity, and, considering the actual data rate, 60 GHz would be the promising frequency.

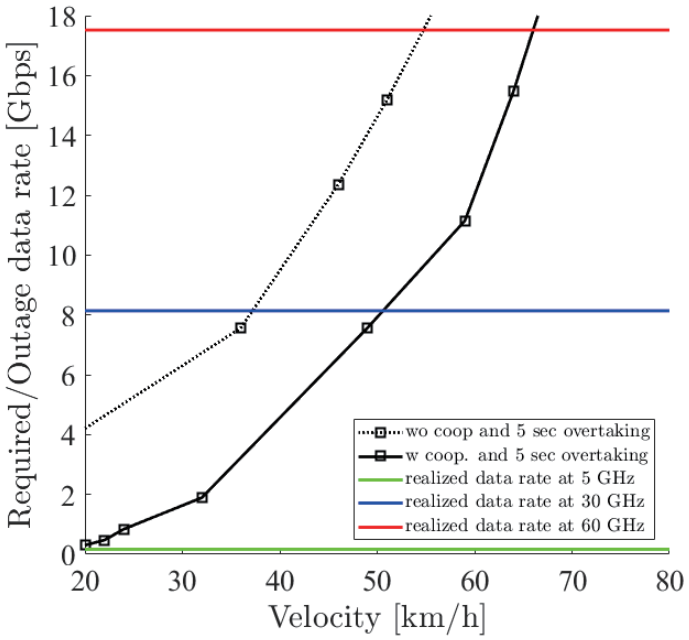

Figure 3.18: Required data rate and 0.01% outage data rate realized by 5, 30 and 60 GHz bands under $d_{\text{be}} = 5$ m.

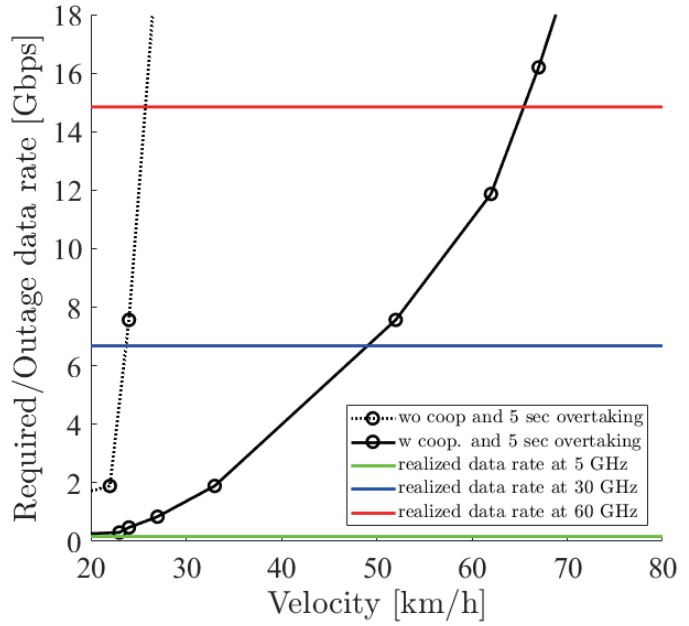

Figure 3.19: Required data rate and 0.01% outage data rate realized by 5, 30 and 60 GHz bands under $d_{\text{be}} = 10$ m.

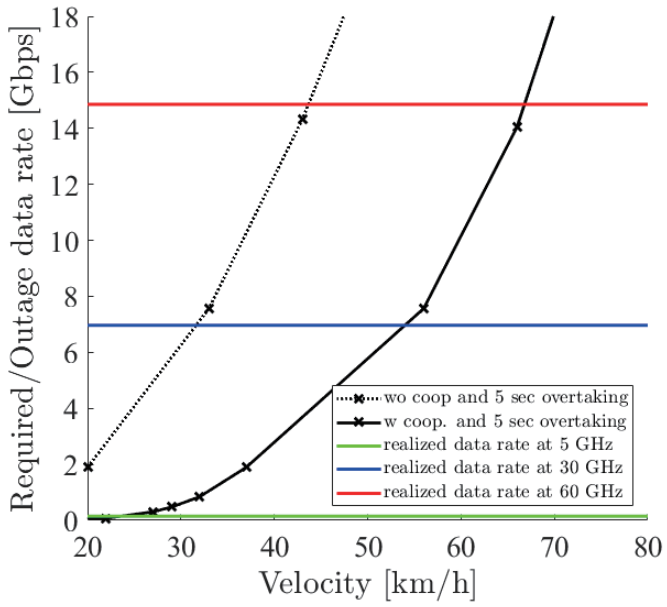

Figure 3.20: Required data rate and 0.01% outage data rate realized by 5, 30 and 60 GHz bands under $d_{\text{be}} = 15$ m.

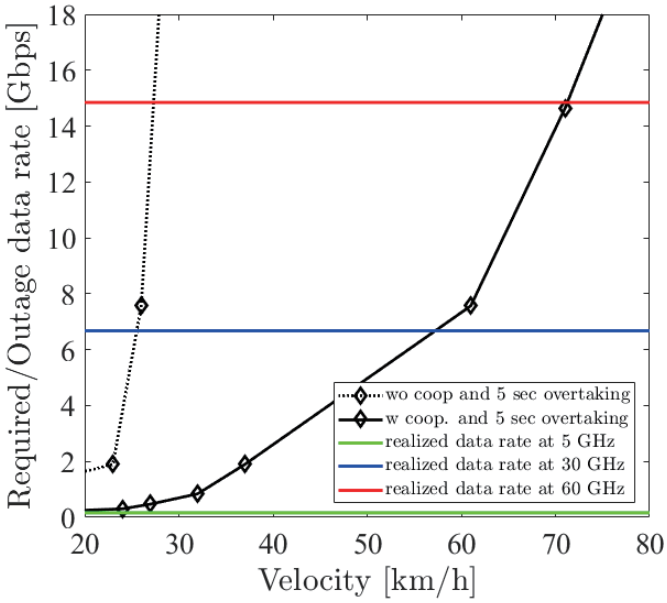

Figure 3.21: Required data rate using a non-linear spacing LiDAR sensor and 0.01% outage data rate realized by 5, 30 and 60 GHz bands under $d_{\text{be}} = 10$ m.

Table 3.1: Simulation Parameters

LiDAR Parameters	
Parameter	**Value**
Location	Vehicle's roof +20 cm
Range	200 m
Elevation Angle Range	±15°
Elevation Angle Resolution (r_ϕ)	[0.2°, 0.1°, 0.08°, 0.06°, 0.04°, 0.02°]
Azimuth Angle Range	180°
Azimuth Angle Resolution (r_θ)	[0.2°, 0.1°, 0.08°, 0.06°, 0.04°, 0.02°]
Non Linear Spacing	dense spacing (−7.5°-7.5°) sparse spacing (otherwise)
Return Mode	Strongest
Scan Period	20 Hz
Data Size of One Point	16 bit (coordinate) + 12 bit (power)

V2V System Parameters in [5, 30, 60] GHz Bands	
Parameter	**Value**
Height of Tx(h_t)	38 cm
Height of Rx1(h_{r1})	38 cm
Height of Rx2(h_{r2})	[98, 48, 43] cm
Height of Rx3(h_{r3})	[182, 62, 50] cm
Transmitted Power	10 dBm
Boresight Gain	[4.3, 20, 26] dB
Antenna Aperture Size	2.6 cm × 2.6 cm
Polarization	vertical
Vertical Antenna Vibration Model	Gaussian(σ =3.2 cm)
Bandwidth	[10, 500, 1000] MHz
Antenna Diversity	selection diversity
Noise Figure	10 dB

Chapter 4

Required and achievable data rate for V2I in intersection scenario

In this chapter, analysis of safety in the intersection scenario is performed and cooperative perception is considered for improving safety. As performed in the overtaking scenario, cooperative perception is based on sending raw sensor data. The overtaking scenario derives the requirements of sensor data rate for safe passing through an intersection with and without cooperative perception. This scenario analyzes safe automated driving from the viewpoint of vehicle dynamics and recognition process as same as in the overtaking scenario. There are two important factors in this scenario. The first factor is that the recognition process is improved by adopting Clustered Viewpoint Feature Histogram (CVFH). The second factor is that not only safety but also traffic efficiency is considered to alleviate traffic congestion.

4.1 Scenario description

Before introducing the intersection scenario, this section starts by showing the works relating to signalized and unsignalized intersections and automated driving. In the case of automated driving vehicles, intersection managers are basically planned to prevent traffic accidents. The role of the intersection manager can be separated into several factors such as V2X interfaces, conflict detection, and vehicle dynamics [83]. There are two architectures for V2X interfaces that are centralized and decentralized approaches. The main advantage of decentralized approaches is that infrastructures are not required so that they can scale easily and be used in uncrowded intersections. On the other hand, centralized approaches follow a server-client scheme. Although the reliability of centralized approaches deeply depends on infrastructures, these approaches can reduce network overheads due to their centralized information. In this analysis, an intersection manager is not considered explicitly, but a simple intersection manager that handles the geographical location of the vehicle is assumed to establish a connection of V2I communications, which can be implemented by centralized or decentralized approaches. Therefore, the control of vehicle behavior such as velocity is performed by the vehicle itself. For example, in the proof-of-concept, we adopted dynamic network management based on the geographical location of a vehicle [18]. Since this analysis focuses on the relation between the performance of wireless communications and safe automated driving,

the same simple communication rule is assumed as the above work.

For vehicle behavior, vehicle dynamics and conflict detection are related to intersection management. Models of vehicle dynamics can be classified into three models. The difference among these models is the dimension of vehicle movement and whether the surrounding environment such as road slope is considered or not. To detect conflict, or collision, grid maps or predefined paths are basically used. In grid maps, the location of a vehicle in each time step is expressed as a grid, and conflict or collision occurs when two vehicles occupy the same grid at the same time. On the other hand, the expected paths are used to check conflict in predefined paths. In this analysis, conflict decision is based on comparing the predefined paths and vehicle dynamics on the path is described as a one-dimension model as follows.

$$\dot{x} = v,$$
$$\dot{v} = a,$$

where x and v are the longitudinal position and velocity of the vehicle and a is the acceleration input to the vehicle. Considering that there are works about speed estimation based on only LiDAR sensors, it is assumed that LiDAR sensors can obtain vehicle velocity [84].

The traffic environment at the intersection is also an important factor. This is because it takes a long time to change all driving vehicles to automated driving vehicles. Therefore, a hybrid environment that both human and automated driving vehicles exist at the intersection should be considered. Related works about managing intersections under the mixture traffic environment can be classified into signalized and unsignalized intersection models. In the case of signalized intersections, basically traffic lights and the intersection manager cooperate on preventing collision at the intersection. In [85], management of a signalized intersection is analyzed and traffic lights at the intersection are controlled by a connected vehicle center. The control is based on the information obtained from traffic detection devices such as radar or LiDAR sensors on roadside units.

On the other hand, in [86, 87], decision making for automated driving at an unsignalized intersection is analyzed by processing sensor data and the experiment of the decision making is performed. In [87], the authors analyze a safe merging at an unsignalized intersection by using probabilistic functions. Both works consider not only the mixture traffic environment but also the incomplete installation of V2X communications, that is, all vehicles cannot necessarily use V2X communications.

Since our analysis focuses on the contribution to safe automated driving with V2I communications, it is assumed that a RSU is set at the intersection and can always send sensor data to the ego vehicle. Namely, the ego vehicle that starts to enter into the intersection can always receive the cooperative perception service. Cooperative perception shares sensor data obtained from different locations and perspectives in the driving environment so that blind spots can be visualized. Using the received sensor data, the ego vehicle tries to pass through an unsignalized intersection under the mixture traffic environment. However, there are no managers that send cooperative control messages to automated driving vehicles.

From the above discussion, this analysis focuses on safe passing through an unsignalized intersection under the presence of a human driving vehicle. Fig. 4.1 shows the assumed

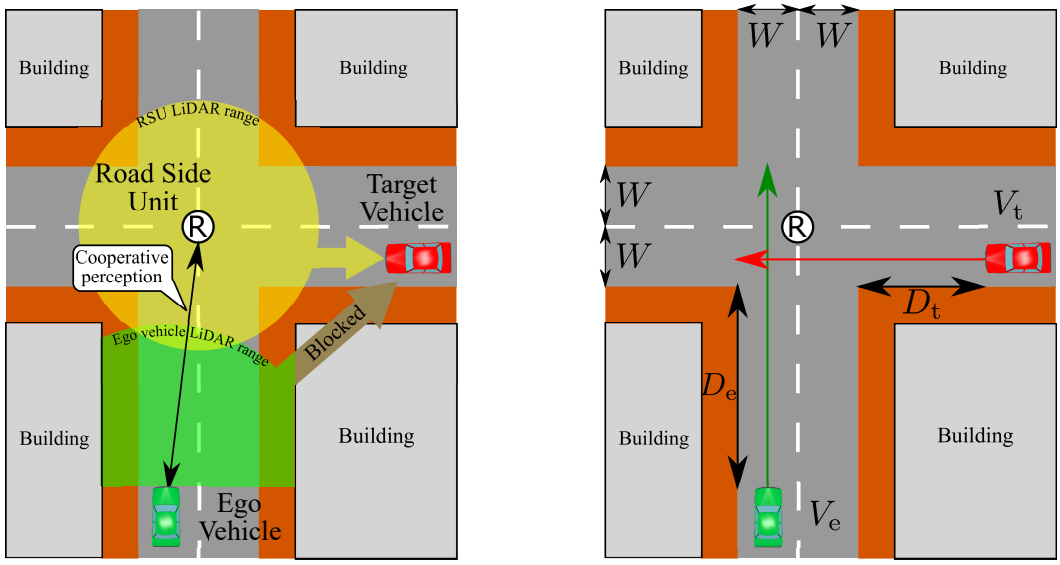

(a) The location and the range of LiDAR sensors. (b) The driving pattern of both ego and target vehicle.

Figure 4.1: Overview of LiDAR sensors and the driving pattern at the unsignalized intersection.

intersection scenario. The green ego vehicle is an automated driving vehicle and the red vehicle is a human driving vehicle. The goal of the ego vehicle is to pass safely through the intersection. However, the red vehicle also tries to pass through the unsignalized intersection at the same time, which will lead to a collision at the intersection. From this assumption, the red vehicle becomes an important recognition target so that the red vehicle is called a target vehicle. For simplicity, the velocity of both vehicles is assumed as constant velocity. Since the target vehicle is a human driving vehicle and there are no intersection managers, the ego vehicle has to recognize the target vehicle and decide whether the safe crossing is possible or not by itself. The other conditions such as weather are the same as the overtaking scenario. In order to accomplish this goal, a RSU is located at the intersection and can be used for cooperative perception. Namely, the ego vehicle receives raw LiDAR sensor data from the RSU and can use it for the recognition process with the sensor data obtained from the ego vehicle. The reason why raw sensor data is chosen is the same as the overtaking scenario. Since the ego vehicle can know the location of the RSU by dynamic maps, it is assumed that the sensor data receiving from the RSU is automatically transformed into the ego vehicle coordinate, which means that the RSU data can be used in the ego vehicle coordinate. When the ego vehicle succeeds to recognize the target vehicle, one of the simplest responses is always applying the brakes even if the collision does not occur at the intersection. However, this simple response will lead to traffic congestion at the intersection. Therefore, the ego vehicle should identify whether the collision will occur or not and apply the brakes in the collision case, which can alleviate traffic congestion. Other conditions such as weather are the same as the overtaking scenario.

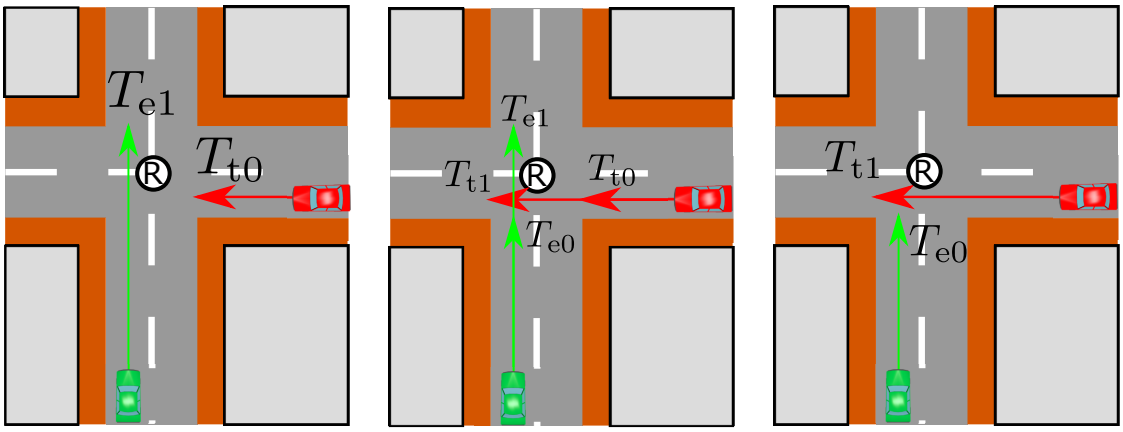

(a) The driving pattern that the ego vehicle crosses first.

(b) The driving pattern that both vehicles are about to pass through the intersection.

(c) The driving pattern that the target vehicle crosses first.

Figure 4.2: The classified three driving patterns.

4.2 Vehicle behavior in the intersection

In order to realize a safe and efficient crossing, the emergency cases where braking is necessary to prevent the collision should be specified. Moreover, this analysis helps to determine a required recognition range to prevent a traffic accident. Since driving at constant velocity is assumed, it is possible to specify the collision cases by considering an arrival time and a leaving time at the intersection that depend on the initial positions of the vehicles. Therefore, the collision cases and the other cases are classified by these time parameters as shown in Fig. 4.2. Fig. 4.2a (Fig. 4.2c) is the driving pattern that the ego (target) vehicle passes first through the intersection. T_{e0} (T_{t0}) is the time for the ego (target) vehicle to arrive to the intersection. T_{e1} (T_{t1}) is the time for the ego (target) vehicle to leave the intersection. In the case of Fig. 4.2a (Fig. 4.2c), the relation of the time parameters is $T_{e1} \leq T_{t0}$ ($T_{t1} \leq T_{e0}$). On the other hand, Fig. 4.2b is the driving pattern that the collision occurs and the relations of the time parameters are $T_{t0} \leq T_{e1} \wedge T_{e0} \leq T_{t1}$. From the above classification, braking is only needed in the Fig. 4.2b case.

From the assumption of constant velocity driving, these time parameters can be described by V_e, V_t, D_e, D_t and the relations of the time parameters in the collision cases can be described as follows.

$$\frac{D_t}{V_t} \leq \frac{D_e}{V_e} + \frac{2W}{V_e}, \tag{4.1}$$

$$\frac{D_e}{V_e} \leq \frac{D_t}{V_t} + \frac{2W}{V_t}, \tag{4.2}$$

where W is the width of the road as shown in Fig. 4.1. Adopting comfortable braking to stop in front of the intersection, the following relation is used for simplifying Eq. 4.1 and Eq. 4.2 [68].

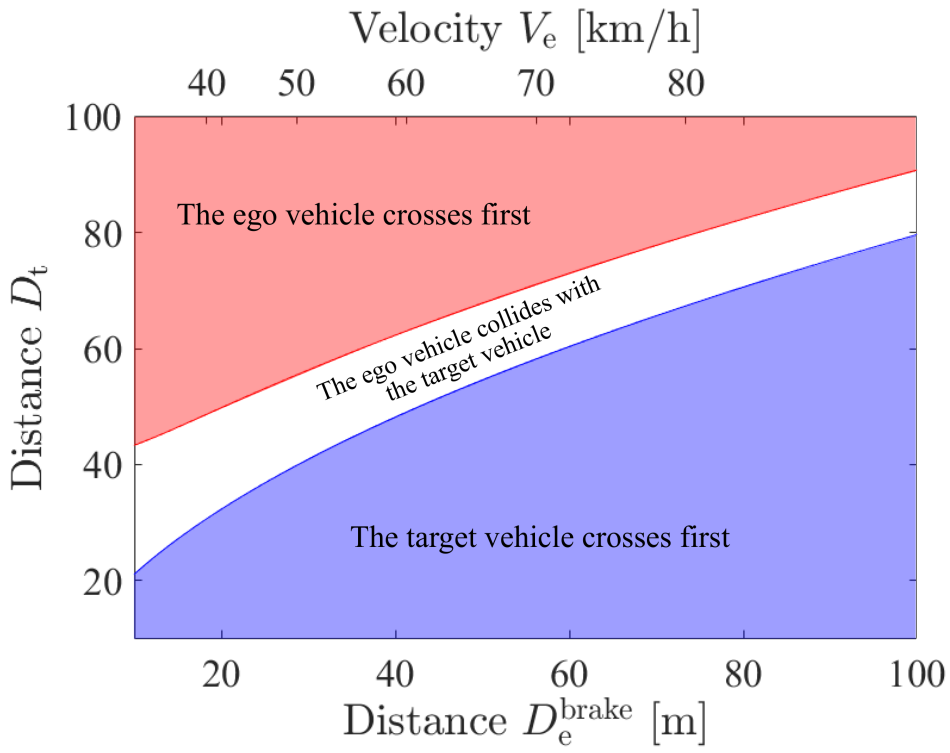

Figure 4.3: The visualized three driving patterns at $V_t = 80$ km/h with comfortable braking.

$$D_e^{brake} = 0.039 \times \frac{V_e^2}{3.4}. \tag{4.3}$$

Using the simplified inequalities, the three driving patterns with comfortable braking under $V_t = 80$ km/h can be visualized as shown in Fig. 4.3. Notice that D_e and V_e have the relation of Eq. 4.3, which shown by D_e^{brake}-axis and V_e-axis in the figure. Since D_e is related to both braking distance and the performance of wireless communications, superscript is used to show the main role of D_e in each analysis. Fig. 4.3 shows that the relation between the driving patterns and the initial locations of the ego vehicle and the target vehicle under the fixed velocity of the target vehicle. Namely, when the ego vehicle places at D_e^{brake} and start to drive at the corresponding V_e, the decision making of the ego vehicle depends on the location and velocity of the target vehicle. When the initial location D_t gets very small (large) under fixed V_t, the target vehicle (the ego vehicle) pass through the intersection first so that it does not have to apply the brakes, which corresponds to the blue (red) area. On the other hand, when the distance and the velocity parameters of the ego and the target vehicle meet Eq. 4.1 and Eq. 4.2, the collision occurs at the intersection, which corresponds to the white area. Therefore, when the parameters of the ego and the target vehicle belong to the white area, the ego vehicle has to perform comfortable braking to prevent the collision and stop in front of

the intersection.

In order to perform the braking only at the collision cases, the ego vehicle has to recognize the target vehicle not in all cases but in the collision cases. This means that at least the ego vehicle has to recognize the target vehicle that is on the upper boundary of the white area. Therefore, the required recognition range D_t^{req} becomes the upper boundary of the white area and it depends on D_e, V_t as shown in the figure. From the above discussion, D_t^{req} for comfortable braking is obtained by substituting Eq. 4.3 for Eq. 4.1 as follows.

$$D_t^{req} = V_t \sqrt{\frac{0.039 D_e}{3.4}} + 2W \cdot V_t \sqrt{\frac{0.039}{3.4 D_e}}. \tag{4.4}$$

As introduced before, a constant velocity is assumed in this scenario, but there are many types of velocity scenarios of the ego vehicle such as driving with acceleration or deceleration. This paragraph discusses this topic. When V_e, D_e, and V_t is given, driving with acceleration (deceleration) makes T_{e0} in Fig. 4.2b small (large) so that the required recognition range becomes short (long). Although a short recognition range requires a smaller sensor data rate than a long recognition range, entering into the intersection with acceleration is dangerous. On the other hand, driving with deceleration is safer than acceleration, but the required recognition range becomes large, which will get far from tight requirements. Since this analysis focuses on not only safe automated driving but also tight requirements, it chooses driving at a constant velocity that can be regarded as the average performance of driving with acceleration and deceleration.

4.3 Object recognition using CVFH

Since the ego vehicle has to recognize the target vehicle to decide whether comfortable braking is needed or not, a recognition process in the ego vehicle is necessary. In general, there are two ways to recognize an object, which is specific object recognition and general object recognition as beforementioned. As shown in the overtaking scenario, specific object recognition using edge points is performed to recognize a vehicle. Since the recognition target is only a vehicle in this analysis as same as the overtaking scenario, specific object recognition is adopted. However, a more practical feature point than an edge point is used for the recognition, and this improvement will provide a tight data rate requirement. Feature descriptors include information about the surrounding surface and meet three characteristics, that is, robustness to rigid transformations, robustness to noise, invariance to the density of point cloud data. Since feature descriptors tell more information than edge points that tell only 3D coordinate information, feature descriptors can recognize the object with fewer points. In general, feature descriptors can be classified into local and global feature descriptors. Local feature descriptors are computed for individual points in a clustered point cloud and tell local geometry for each point. On the other hand, global feature descriptors are computed for a whole clustered point cloud. This means that both global and local feature descriptors require a preprocessing such as segmentation to a source point cloud. In this recognition process, CVFH

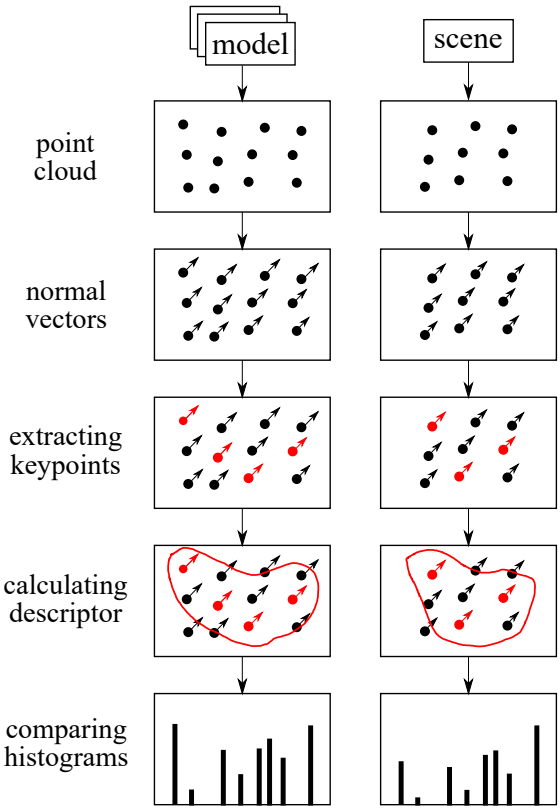

Figure 4.4: The process flow of object recognition.

which is one of the global feature descriptors is adopted and CVFH functions implemented in Point Cloud Library (PCL) are used [88]. The reason for this adoption is that CVFH is robust to occlusions that often occur by vehicles or buildings [89].

A process flow of vehicle recognition is shown in Fig. 4.4. This object recognition process consists of four processes and these processes are performed to both model and scene point cloud data. Since model base recognition is adopted, the model point cloud data is prepared for the object recognition process. In this recognition, the ego vehicle does not only recognize whether the obtained point cloud data is a vehicle or not but also the direction of the vehicle. The driving direction is specified for how the vehicle drives on a road and this check helps to guarantee that the traffic environment matches with one of the classified driving patterns. The model point cloud data is generated by sensing a 3D vehicle model and a rectangular model under no obstacles in the assumed traffic environment. This data generation provides the maximum information for each model from the ego vehicle under the fixed locations of the vehicles. The rectangular model is prepared to check whether the ego vehicle has enough point cloud data to recognize the object or not and avoid fortunate recognition. On the other hand, the scene point cloud data is obtained by LiDAR sensors in the assumed traffic environment.

The object recognition starts from preparing a clustered point cloud. In this analysis, all points obtained by ray-trace simulation have a tag that tells which objects each point is on

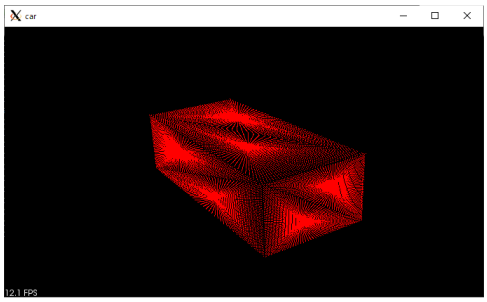

(a) Model data of the front of the rectangular.

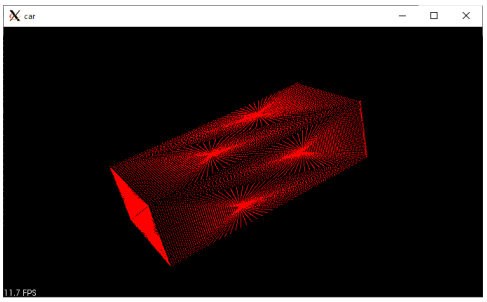

(b) Model data of the side of the rectangular.

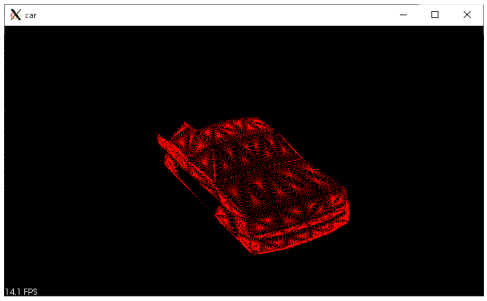

(c) Model data of the front of the vehicle.

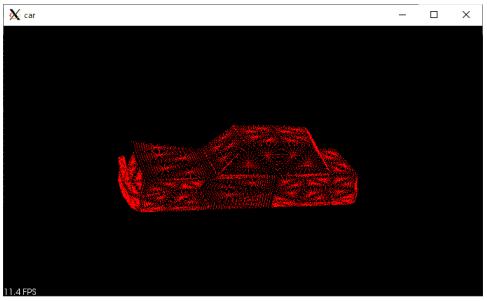

(d) Model data of the left of the vehicle.

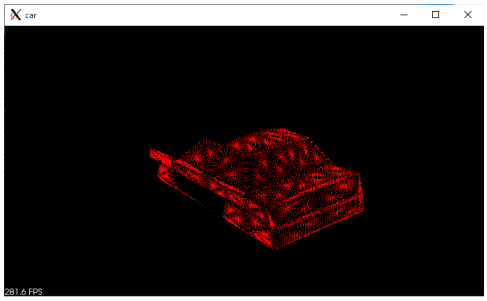

(e) Model data of the rear of the vehicle.

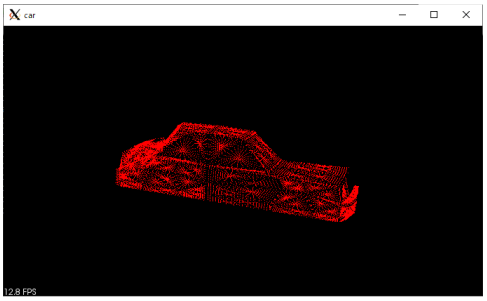

(f) Model data of the right of the vehicle.

Figure 4.5: Examples of model point cloud data.

as same as the overtaking scenario. Collecting points on the target vehicle, ideal clustering can be performed. The next process is the calculation of a normal vector for each point to calculate CVFH. After preparing the clustered point cloud with normal vectors, keypoints are extracted from the clustered point cloud. In PCL, keypoints are explained as points that are stable, distinctive, and can be identified by using a well-defined detection criterion. The main advantage of using keypoints is that selecting points from the clustered points reduces the calculation time. Actually, instead of using keypoints modules, a voxel grid filter is often used to just reduce the number of points for convenience. The extracted keypoints are used to calculate CVFH and this calculation outputs histogram data. Finally, histograms calculated from the scene and the model point cloud are compared and object and direction recognition is performed by choosing the nearest histogram. Since a large part of sensor data is obtained from the RSU, the histograms are made from the viewpoint of the RSU.

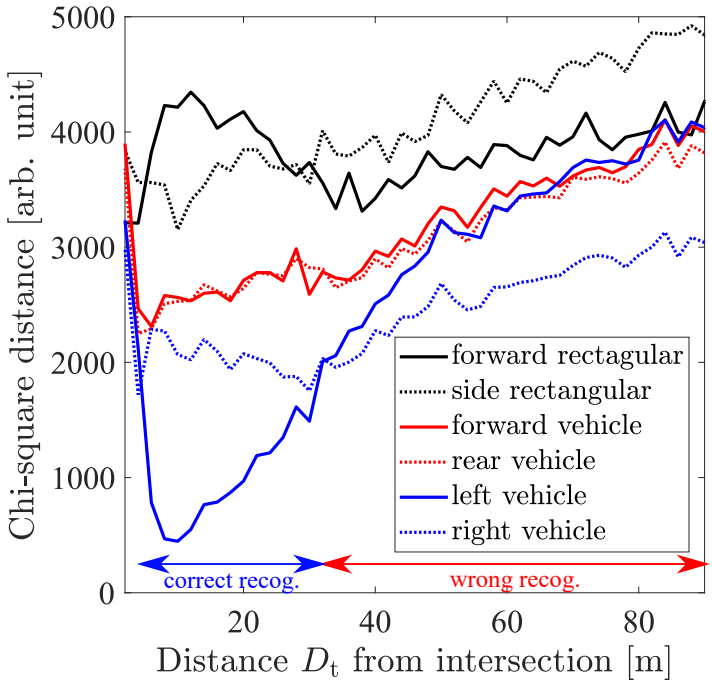

Figure 4.6: Transition of chi-square distance calculated by comparing CVFH histograms.

In order to choose the nearest histogram, the quantity that describes the similarity among histograms has to be defined. There are several ways to compare histograms such as using correlation, chi-square distance, and intersection. Since chi-square distance is used to compare histograms generated by feature descriptors in the examples of PCL, chi-square distance is adopted as shown in the following equation.

$$d_{\mathrm{chi}}(H_1, H_2) = \sum_i \frac{(H_1(i) - H_2(i))^2}{H_1(i) + H_2(i)}. \tag{4.5}$$

The idea of chi-square distance comes from regarding the difference between small bins as important.

There are six models prepared for recognizing the object and the direction by comparing the histograms. The visualized parts of the target vehicle are defined from the viewpoint of the ego vehicle. Fig. 4.5 shows examples of compared point cloud data. As shown in the figures, there are two models of the rectangular model and four models of the vehicle model. Firstly, the ego vehicle decides whether the object is the vehicle model or the rectangular model. When the ego vehicle does not have enough data, it recognizes the point cloud as the rectangular model. Secondly, the ego vehicle determines which direction the object faces among the four directions. Since the rectangular has symmetries, there are only two models for the rectangular model.

Fig. 4.6 shows examples of the transition of chi-square distance between the model histogram and the obtained histogram. The transition of chi-square distance without cooperative

perception is omitted because the buildings block almost all lasers from the LiDAR sensor on the ego vehicle to the target vehicle. In this scenario, when the ego vehicle recognizes the obtained point cloud as the left side of the vehicle shown in Fig. 4.5d, the ego vehicle recognizes the correct traffic environment, which will lead to the correct braking decision. This is because all LiDAR sensor data is transformed into the ego vehicle coordinate as assumed in this scenario and the left side of the target vehicle can be visualized from the ego vehicle under the intersection with no obstacles. From the figure, when the ego vehicle uses cooperative perception, it recognizes correctly the target vehicle in the range from $D_\mathrm{t} = 5$ m to 32 m. Since the LiDAR sensor on the RSU does not see directly below the RSU, the recognition range does not start from 0 m.

One way to define the recognition range d_recog is to choose the maximum D_t where the ego vehicle can recognize the target vehicle correctly. From Fig. 4.6, when the wrong recognition range around 0 m is regarded as negligible, the maximum value is read as 32 m and the recognition range becomes 32 m. Although the maximum D_t becomes the recognition range d_recog in this case, there are no guarantees that the ego vehicle can continuously recognize the target vehicle in general under this d_recog definition. Since the recognition range should guarantee the correct result within the range, the recognition range d_recog is defined as follows.

$$
\begin{aligned}
d_\mathrm{recog}(r_\phi,\ r_\theta) &= \max d_0(r_\phi,\ r_\theta), \\
\text{s.t.} \quad \forall d < d_0,\ \ \underset{m \in M}{\arg\min}\, d_\mathrm{chi}\left(H_\mathrm{scene}(r_\phi,\ r_\theta),\ H_\mathrm{m} \mid d_\mathrm{recog}^\mathrm{min} + d\right) &= m_\mathrm{l},
\end{aligned}
\tag{4.6}
$$

where m_l describes the left side of the vehicle model that is the correct model as explained before, $r_\phi,\ r_\theta$ are the LiDAR sensor resolutions of azimuth and elevation angle that are used to calculate point cloud and histograms.

4.4 Derivation of required sensor data rate

In order to derive the required sensor data rate R_req, it is important to know how LiDAR sensors output sensor data. In this simulation, assumed LiDAR sensors scan the surrounding environment by spinning lasers at a certain frequency. Therefore, scanning frequency, the number of points per scan, and the data size of one point give the sensor data rate of the LiDAR sensor. Considering the mechanism of the assumed LiDAR sensor, the required sensor data rate R_req to prevent the collision is formulated as follows.

$$
\begin{aligned}
R_\mathrm{req} &= \left(\left\lfloor \frac{A_\theta}{\widehat{r_\theta}} \right\rfloor + 1\right) \times \left(\left\lfloor \frac{A_\phi}{\widehat{r_\phi}} \right\rfloor + 1\right) \times F_\mathrm{scan} \times D_\mathrm{symbol}, \\
\text{where } \{\widehat{r_\phi},\ \widehat{r_\theta}\} &= \underset{\{r_\phi,\ r_\theta\}}{\arg\min}\, d_\mathrm{recog}(r_\phi,\ r_\theta) > D_\mathrm{t},
\end{aligned}
\tag{4.7}
$$

where A_ϕ and A_θ are the scanning range in the azimuth and elevation angle (degree), F_scan is scan frequency (Hz) of the LiDAR sensor, and D_symbol is the amount of information per one laser point (bits).

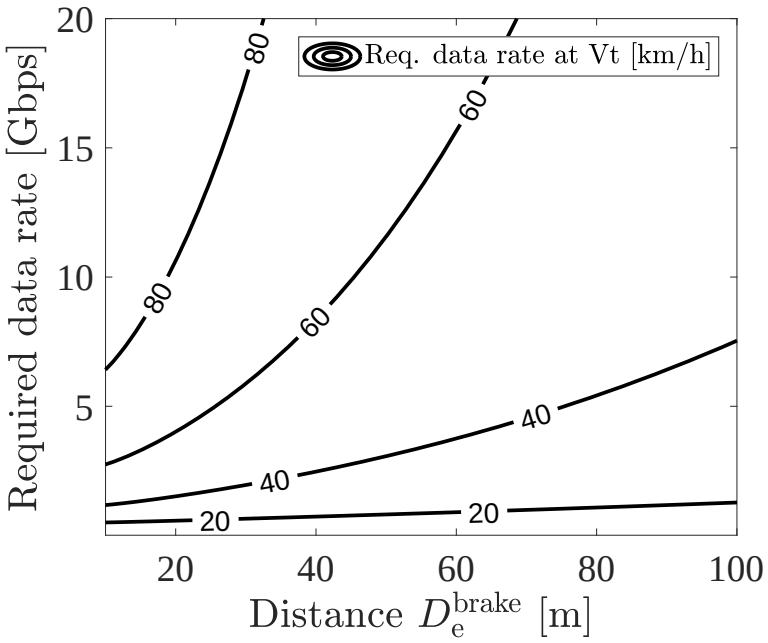

Figure 4.7: The sensor data rate required for the ego vehicle placed at D_{e} to avoid a collision with the target vehicle driving at V_{t}.

Summarizing the analysis until now, two relations are obtained. The first relation is between D_{e} and D_{t}, which tells the recognition range d_{recog} required for the ego vehicle placed at D_{e} to prevent the collision with the target vehicle driving at V_{t}. The second relation is between d_{recog} and the required sensor data rate R_{req}, which tells the required sensor data rate R_{req} to realize the required recognition range d_{recog}. Therefore, the sensor data rate required for the ego vehicle placed at D_{e} can be obtained from the above two relations. However, in order to obtain the required sensor data rate for each D_{e}, many resolution sets of LiDAR sensors have to be calculated. Therefore, a fitting curve is used to calculate the required sensor data rate for each D_{e}.

Fig. 4.7 shows the required sensor data rate to avoid a collision with the target vehicle driving at V_{t} from the ego vehicle driving from D_{e}. From the figure, as the target vehicle velocity V_{t} becomes high under a fixed D_{e}, the required sensor data rate gets rapidly high. This is because the collision with the high-velocity target vehicle occurs in the case where the target vehicle drives from a far place. This means that the ego vehicle needs high-resolution LiDAR sensors to realize a long recognition range.

4.5 Millimeter-wave V2I communications

Since this analysis focuses on the relation between the performance of wireless communication and safe crossing, it compares the cooperative perception for safe crossing realized by the conventional and the millimeter-wave V2I communications as same as the overtaking

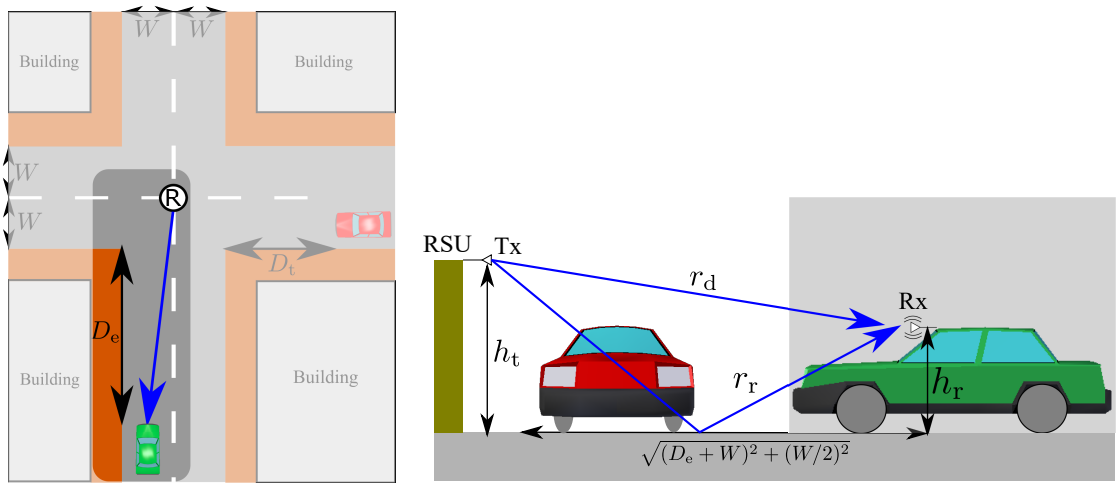

Figure 4.8: The two-ray ground reflection model with receiver vibrating.

scenario. The analysis is performed by comparing the sensor data rate and outage capacity calculated by the assumed channel model. In general, there are deterministic path loss models, statistical models, tapped delay line models, and geometry-based stochastic models to describe channel models for the 5.9 GHz frequency band [90]. In [91], the authors used two-ray ground reflection models to compare V2I measurements in the 5.9 GHz frequency band. The results show that the model can properly represent the received power in LOS and NLOS environments. In [92], the authors analyzed millimeter-wave V2I communications and showed that two-ray channel models well represent millimeter-wave communications with highly directional antennas. Considering the above works, V2I propagation model is also assumed as a two-ray ground reflection model that is one of the deterministic path loss models, which will reduce calculation time.

Fig. 4.8 shows the assumed V2I propagation model. In this model, the receiver on the vehicle is vibrating due to a driving motor while the transmitter on the RSU is not vibrating [77]. Moreover, since automated driving vehicles can know the locations of RSUs by dynamic maps, the ideal beam alignment is assumed.

The received power is formulated as follows.

$$P_{\mathrm{r}} = \frac{P_{\mathrm{t}}}{L(r_{\mathrm{d}})}\left|\sqrt{G_{\mathrm{d}}}\left(\frac{c}{4\pi f_{\mathrm{c}} r_{\mathrm{d}}}\right) + \sqrt{G_{\mathrm{r}}}\left(\frac{c}{4\pi f_{\mathrm{c}} r_{\mathrm{r}}}\right)\Gamma \mathrm{e}^{-\mathrm{j}\{k(r_{\mathrm{d}}-r_{\mathrm{r}})\}}\right|^2, \tag{4.8}$$

where P_{t} is transmission power, G_{d} and G_{r} are the antenna gains for direct and reflected wave, r_{d} and r_{r} are the optical path length for direct and reflected waves, $L(r_{\mathrm{d}})$ is the absorption factor at 60 GHz by oxygen as 15 dB/km, c is the speed of light, f_{c} is a carrier frequency, k is $2\pi/\lambda$, Γ is the complex reflection coefficient. Basic analysis about the effect of vibration on fading and height diversity has been already performed in the overtaking scenario. Therefore, this analysis focuses on the effect of height diversity in the case V2I communications.

Fig. 4.9 shows 0.01% outage capacities using height diversity and not using height diversity and the average of channel capacity. Since the same parameters are used in the simulation, the parameters used in this calculation are summarized in Table. 4.1. 0.01% is based

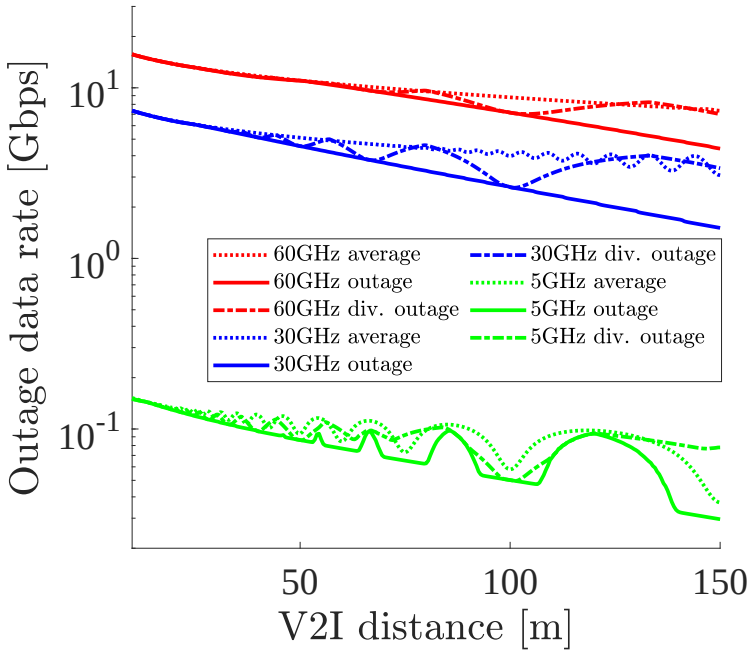

Figure 4.9: 0.01% outage capacity with and without height diversity and the average capacity without height diversity.

on the requirements for the reliability of transmitting raw sensor data published by 3GPP [9]. The 0.01% outage capacity is calculated by the following formula.

$$P(c(h_{\mathrm{r}} \mid D_{\mathrm{e}},\ f_{\mathrm{c}}) < C_{\mathrm{out}}(h_{\mathrm{r}} \mid D_{\mathrm{e}},\ f_{\mathrm{c}})) = 0.01\%, \tag{4.9}$$

where the function P is the probability function about the capacity c of the V2I communication, and the capacity c stochastically changes due to the vibrating receiver h_{r} under the fixed D_{e} and the carrier frequency f_{c}. From the figure, it is shown that height diversity certainly improves the outage capacity, but the increased amount of the outage capacity is not drastically large.

This height diversity performance difference can be discussed from two aspects. The first aspect is antenna vibration that cause dynamic change of phase difference. Since no vibration at the receiver is assumed, a large phase difference between the direct path and the reflected path rarely occurs so that the improvement gets small. The second aspect is the beamwidth of the antenna. Since millimeter-wave communications have a large path loss, its antenna needs strong directivity to realize long-range communications. In [77, 93], narrow beamwidth such as 10 degrees is used for outdoor measurement of millimeter-wave communications. On the other hand, the narrow beamwidth is also adopted in our analysis to not only realize long-range communication but also utilize spatial diversity, or spatial channel reuse, in dense traffic. Using such narrow beamwidth in V2I communication, the difference in the angle of departure between the direct path and the reflected path becomes large so that

Table 4.1: Simulation Parameters

LiDAR Parameters	
Parameter	**Value**
Location	Vehicle's roof +20 cm
Range	200 m
Elevation Angle Range	$-25^\circ \sim +15^\circ$
Elevation Angle Resolution (r_ϕ)	[0.2°, 0.1°, 0.09°, 0.08°, 0.07°, 0.06°, 0.05°, 0.04°, 0.03°, 0.02°]
Azimuth Angle Range	360°
Azimuth Angle Resolution (r_θ)	[0.2°, 0.1°, 0.09°, 0.08°, 0.07°, 0.06°, 0.05°, 0.04°, 0.03°, 0.02°]
Return Mode	Strongest
Scan Period	20 Hz
Data Size of One Point	16 bit (coordinate) + 12 bit (power)
V2I System Parameters in [5, 30, 60] GHz Bands	
Parameter	**Value**
Height of Tx(h_t)	5.0 m
Height of Rx(h_r)	1.8 m
Transmitted Power	10 dBm
Boresight Gain	[4.3, 20, 26] dB
Antenna Aperture Size	2.6 cm × 2.6 cm
Polarization	vertical
Vertical Antenna Vibration Model	Gaussian(σ =3.2 cm)
Bandwidth	[10, 500, 1000] MHz
Noise Figure	10 dB

the reflected path does not depart from a high gain of the main lobe. Therefore, the effect of the destructive interference becomes small due to the small power of the reflected wave. However, the effect of the constructive interference also becomes small so that the outage capacity does not rapidly decrease.

4.6 Theoretical speed limitation

From the above discussion, the safe crossing can be formulated as follows.

$$\begin{aligned} \text{safe passing: } & V_\mathrm{t} \leq V_\mathrm{t}^\mathrm{max}(V_\mathrm{e}^\mathrm{safe},\ f_\mathrm{c}), \\ & \text{where } V_\mathrm{t}^\mathrm{max} = \max V_\mathrm{t}^\mathrm{safe}(V_\mathrm{e}^\mathrm{safe},\ f_\mathrm{c}), \\ \text{dangerous passing: } & \text{otherwise}, \end{aligned}$$

where a pair of $\{V_\mathrm{e}^\mathrm{safe},\ V_\mathrm{t}^\mathrm{safe}\}$ is the velocity that ensures no collision at the intersection, and $V_\mathrm{t}^\mathrm{max}$ is the maximum velocity of $V_\mathrm{t}^\mathrm{safe}$ under the given $V_\mathrm{e}^\mathrm{safe}$. $V_\mathrm{t}^\mathrm{max}$ also depends on the carrier frequency f_c because it relates to the recognition range that becomes the basis of the safe crossing. The details of $\{V_\mathrm{e}^\mathrm{safe},\ V_\mathrm{t}^\mathrm{safe}\}$ is shown as follows.

$$\{V_\mathrm{e}^\mathrm{safe},\ V_\mathrm{t}^\mathrm{safe}\} \quad \text{s.t. } C_\mathrm{out}(f_\mathrm{c},\ D_\mathrm{e}(V_\mathrm{e}^\mathrm{safe})) > R_\mathrm{req}(D_\mathrm{e}(V_\mathrm{e}^\mathrm{safe}),\ V_\mathrm{t}^\mathrm{safe},\ D_\mathrm{t}).$$

From the assumption, $\{V_\mathrm{e}^\mathrm{safe},\ V_\mathrm{t}^\mathrm{safe}\}$ has to meet the relation that the outage capacity C_out is higher than the required sensor data rate R_req to prevent the collision by cooperative perception.

In this scenario, a single target vehicle is assumed so far, but multiple target vehicles on the left and the right lanes should also be discussed. Therefore, this paragraph expands to multiple target vehicles and discuss this scenario. Firstly, the criterion for safe crossing should be formulated. The key factor is that the two inequalities for the passing through the intersection in Eq. 4.1 and Eq. 4.2 only depend on the distance and velocity. Therefore, the superposition of this criterion to all target vehicles ensures the safe crossing with no collision, and it is formulated as follows.

$$\begin{aligned} \text{safe passing: } & \forall V_\mathrm{t}^i \in \mathcal{V}_\mathrm{t},\ \text{s.t. } V_\mathrm{t}^i \leq V_\mathrm{t}^\mathrm{max}(V_\mathrm{e}^\mathrm{safe},\ f_\mathrm{c}), \\ \text{dangerous passing: } & \text{otherwise}, \end{aligned}$$

where $\mathcal{V}_\mathrm{t}$ is the set of velocity of all target vehicles, and V_t^i is the velocity of the ith target. From this formula, $V_\mathrm{t}^\mathrm{max}$ can be used as same as a single vehicle scenario, and $V_\mathrm{t}^\mathrm{max}$ is regarded as the speed limitation for the safe crossing.

4.7 Performance of millimeter-wave V2I communications to support safe crossing

To estimate the safe crossing realized by conventional V2I communications and millimeter-wave communications, the simulation is performed. Fig. 4.10a and Fig. 4.10b show the

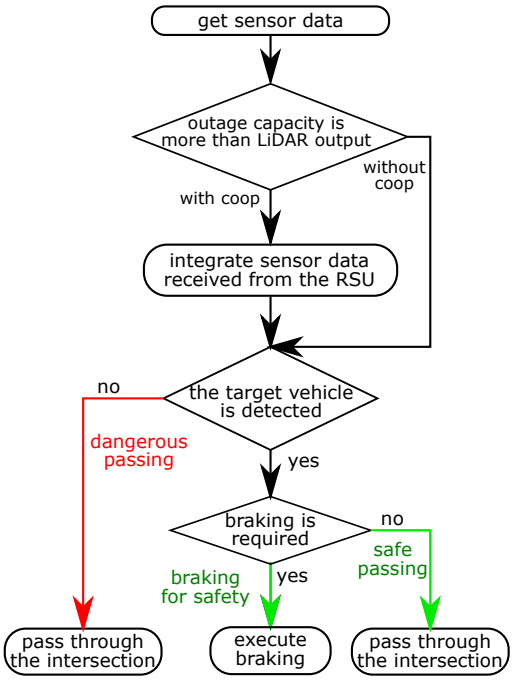

(a) Block diagram of safe crossing.

Algorithm 1 Safe crossing

initialize the point cloud buffer PC_{buffer}.
set the resolution $(r_\phi,\ r_\theta)$ of LiDAR sensors.
calculate sensor data rate R_{sensor} by using $F_{\text{scan}},\ D_{\text{symbol}}$.
set D_{e}, D_{t}, and V_{t}.
calculate V_{e} from D_{e}.
calucalte LiDAR sensor data PC_{ego} obtained by the ego vehicle.
calucalte LiDAR sensor data PC_{rsu} obtained by the RSU.
add to the buffer PC_{buffer} += PC_{ego}.
calculate the outage capacity C_{out} under D_{e}.
if $C_{\text{out}} > R_{\text{sensor}}$ **then**
  $f_{\text{coop}} = \text{true}$
else
  $f_{\text{coop}} = \text{false}$
end if
if $f_{\text{coop}} == \text{true}$ **then**
  add to the buffer PC_{buffer} += PC_{rsu}.
end if
perform the CVFH recognition process with PC_{buffer}.
if $\arg\min_{m \in M} d_{\text{chi}}\left(H_{\text{scene}},\ H_{\text{m}} \mid D_{\text{t}}\right) = m_{\text{l}}$ **then**
  if braking is required **then**
    execute braking and stop in front of the intersection.
  else
    execute a safe crossing.
  end if
else
  execute a dangerous crossing.
end if

(b) Algorithm of safe crossing.

Figure 4.10: Description of the whole process in the simulation.

process flow of the simulation. Firstly, the parameters such as the resolution of the LiDAR sensors, distance, and velocity are set. Then, the LiDAR sensor data obtained from the ego vehicle and the RSU is simulated. Since this LiDAR sensor simulation is the same as the overtaking scenario, it is omitted and the explanation is leaved to the overtaking scenario. The LiDAR sensor model used in this simulation is based on Velodyne VLS-128 that is a mechanical LiDAR sensor and can look downward deeper than upward. Since the RSU has to sense downward mainly, this model is appropriate for the intersection scenario. After finishing the simulation of the obtained point cloud, the point cloud receiving from the RSU is transformed into the ego vehicle coordinate as previously assumed. Moreover, considering that LiDAR sensors can estimate the velocity of a vehicle, the ego vehicle can know the velocity of the target vehicle. After this LiDAR sensor process, the outage capacity between the RSU and the ego vehicle is calculated under D_{e} to check whether the ego vehicle can use cooperative perception or not. To simplify the system, the ego vehicle can use cooperative perception when the outage capacity is more than the LiDAR sensor data rate. When the ego vehicle uses cooperative perception, it can use not only its sensor data but also the sensor data of the RSU for the recognition process. Then, the recognition process based on CVFH is performed. When the recognition result corresponds to the correct target vehicle, the ego vehicle can decide whether comfortable braking is necessary to avoid the collision. Otherwise, the ego vehicle believes that no vehicles enter into the intersection, which will lead to

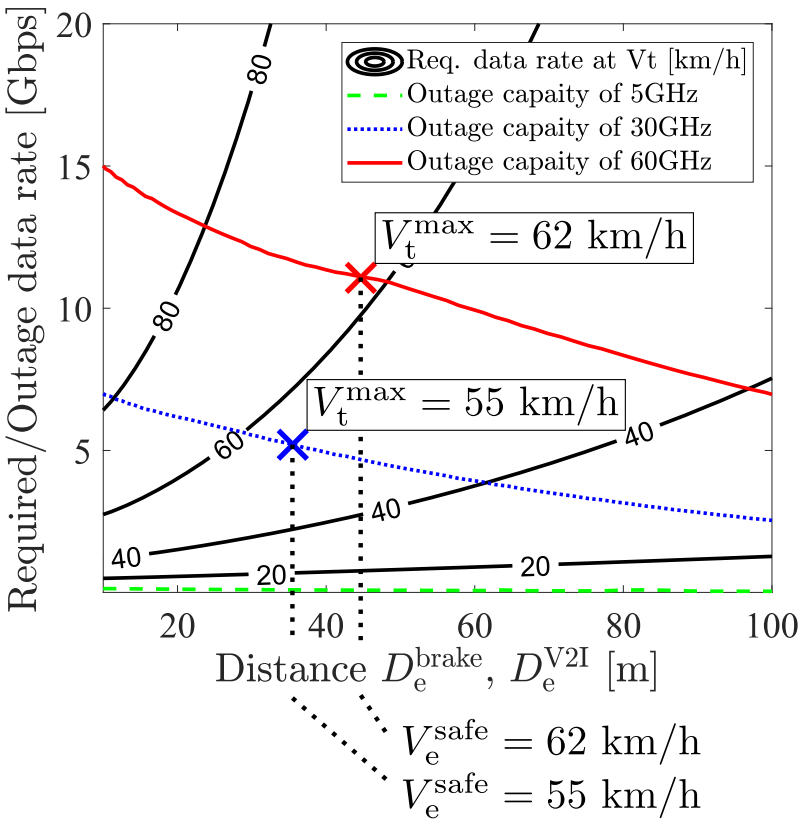

Figure 4.11: The contour plot shows the required sensor data rate at each V_{t} and the color lines show the outage capacity realized by each carrier frequency.

the collision.

Fig. 4.11 shows the result of the simulation and Table 4.1 shows the parameters used in this simulation. The x-axis describes D_{e} which relates to the braking distance and the outage capacity of the V2I communication. The contour plot shows the required sensor data rate as same as the plot in Fig. 4.7. The red, blue, and green lines show the realized outage capacity using 60, 30, and 5 GHz V2I communication.

The safe velocity pair $\{V_{\mathrm{e}}^{\mathrm{safe}},\ V_{\mathrm{t}}^{\mathrm{safe}}\}$ realized by each carrier frequency belongs to the area below each red, blue and green lines. The velocity values $V_{\mathrm{e}},\ V_{\mathrm{t}}$ are obtained by reading the contour plot and D_{e}. As D_{e} gets large, the decrease of the outage capacity and the increase of the required sensor data rate for each V_{t} are read from the figure. The decrease of the outage capacity is due to getting far from the RSU, and the increase of the required sensor data rate is due to the necessity of a long recognition range.

In order to estimate the ability of cooperative perception at each carrier frequency, this analysis focuses on the maximum velocity pair that both $V_{\mathrm{e}}^{\mathrm{safe}}$ and $V_{t}^{\max}$ are the same velocity and get maximum at the carrier frequency, which is called the maximum safe velocity set in this analysis. This estimation comes from reflecting two aspects. The first aspect is that the ego vehicle should pass through the intersection as fast as possible to alleviate traffic

congestion. The second aspect is that the ego vehicle also wants to prevent collision with the high-velocity target vehicle. By this estimation, it is shown that passing through the intersection at 62 (55) km/h requires 11 (5) Gbps which can be supported by 60 (30) GHz. On the other hand, 5 GHz does not have the ability to send raw sensor data. This result concludes that millimeter-wave V2I communications are needed to ensure safety at a realistic velocity and have a better potential for safe driving than conventional V2I.

This paragraph also discusses the recognition performance difference between edge point recognition used in the overtaking scenario and CVFH. In the case of edge point recognition, since extracting edge points is performed by principal component analysis for each keypoint, the complexity becomes $O(nk)$, where n is the number of keypoints and k is the number of neighbor points for each keypoint. On the other hand, CVFH is the combination of euclidean clustering and VFH calculation so that its complexity is near to $O(nk)$. However, CVFH has to calculate euclidean clustering additionally and the preparation of model data is more complex than edge points. Therefore, it is convenient to enable edge point recognition to realize the same recognition ability as CVFH by tuning the threshold from the viewpoint of reducing calculation time. When the threshold is changed from 0.9 to 0.8 (0.77), the maximum safe velocity at 60 (30) GHz becomes the same result as CVFH.

Chapter 5

Demonstration of cooperative perception

This chapter introduces the architecture of cooperative perception in the automated driving trial field and show the demonstration of cooperative perception.

5.1 Architecture

Fig. 5.1 shows the automated driving trial field where we performed cooperative perception. The demonstration is performed in the Tokyo Institute of Technology Ookayama campus and there are 4 RSUs. Fig. 5.1b shows the installed hardware on the RSUs. The installed hardware consists of USB cameras (Ailipu Technology ELP USBFHD05MT-DL36-J), 3D LiDAR sensors (Velodyne VLP-16), and millimeter-wave antennas (Panasonic PE710-TE6). Since measures against exposing 3D LiDAR sensors to rain are under discussion, the installed location of 3D LiDAR sensors in this demonstration is different from this figure. The hardware on the ego vehicle consists of a 3D LiDAR sensor, a camera (Point Grey Grasshopper3), and a millimeter-wave antenna (Panasonic PE710-TE6) as shown in Fig. 5.2. A 3D LiDAR sensor provided by Velodyne or Robosense can be installed on the ego vehicle, and a Velodyne LiDAR sensor is used at this time.

Velodyne VLP-16 is one of the mechanical LiDAR sensors that spin a laser transmitter and receive reflected lasers. The specification of the LiDAR sensor in this demonstration is summarized in Table. 5.1. The parameter of return mode describes how to process the reflected lasers. When a laser hits on multiple objects at one laser emission, multiple reflected lasers return to the LiDAR sensor, which often occurs in the case of emitting lasers to a tree. This parameter specifies the number of returned lasers and there are strongest return mode and dual return mode. The strongest mode only records the strongest reflected power among the reflected lasers. On the other hand, the dual return mode records the strongest and the second strongest reflected power. Once the configuration of the LiDAR sensor is set, the LiDAR sensor outputs data with the following packet structure. Velodyne LiDAR sensors broadcast position packets and data packets. Since a global positioning system is not used in this demonstration, only data packets are focused. 16 lasers are emitted for each azimuth angle and it takes 55.296 μs to charge and reemit 16 lasers in the next azimuth angle. As shown that the data of 16 lasers is saved in one block and there are 24 blocks in one packet, it takes 1.33 ms to send on one packet so that packet rate becomes 754 packet/s. The azimuth

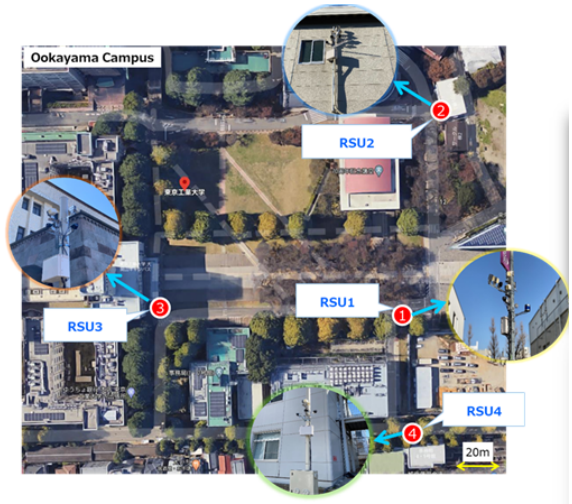

(a) The overview of the automated driving trial field.

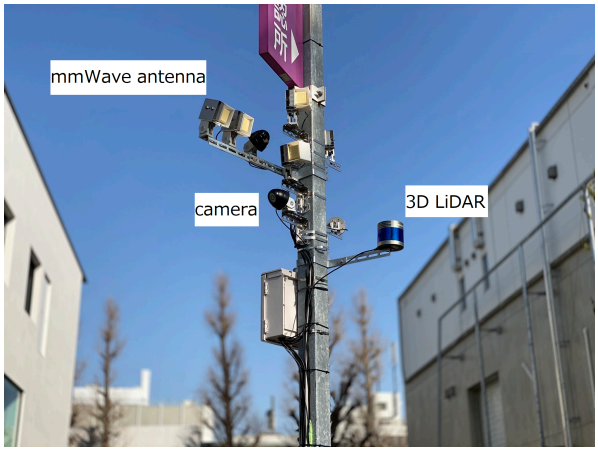

(b) The installed sensors on the RSUs.

Figure 5.1: The automated driving trial fields and the RSUs.

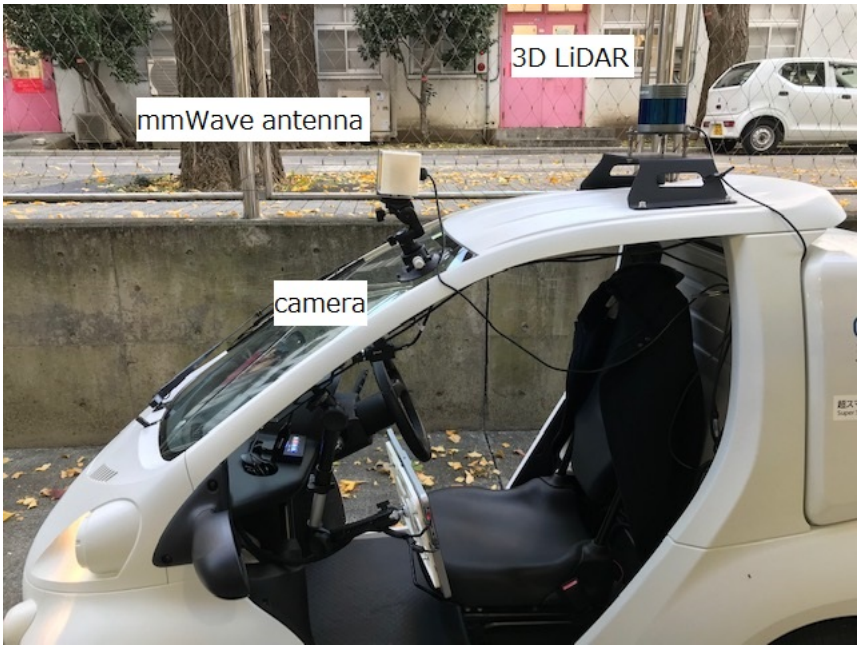

Figure 5.2: The hardware installed on the ego vehicle.

Table 5.1: Specification of the Velodyne LiDAR sensor.

Parameter	Value
Laser range	100 m
Error	±3 cm
Elevation angle range	$-15^\circ \sim +15^\circ$
Resolution of elevation angle	2°
Azimuth angle range	360°
Resolution of azimuth angle	$0.1^\circ \sim 0.4^\circ$
Scanning frequency	10 Hz
Return mode	strongest
Wavelength	903 nm

angle is explicitly recorded for every two groups of 16 lasers. The azimuth angle of the second group is calculated by using the recorded angle and the next azimuth angle.

Fig. 5.4 shows the scenario of the driving path and the communication links in this demonstration. The yellow circles show the coverage of the LiDAR sensors, the red dotted lines show the communication links. The ego vehicle starts from the near RSU3 in Fig 5.1a, passes through the RSU1, and arrives at RSU4. Since the ego vehicle wants to know whether there are obstacles on the driving path in advance, cooperative perception with the RSU1 and the RSU4 is performed. When the ego vehicle locates between the RSU3 and RSU1, it receives LiDAR sensor data from the RSU1 and RSU4 to visualize blind spots as shown in Fig. 5.4a. After the ego vehicle passer through the RSU1, it receives LiDAR sensor data only from RSU4 because it does not need the information about a backward view as shown in Fig. 5.4b.

In order to realize this scenario, we construct a network as shown in Fig. 5.5. The solid lines show wired connections, the dotted lines show wireless connections, the green lines show packet flows at the first phase of the driving phase, and the red lines show packet flows at the second phase of the driving phase. As explained in the driving scenario, the ego vehicle driving between the RSU3 and the RSU1 receives the LiDAR sensor data from the RSU1 and RSU4. The gree lines from the two LiDAR sensors reflect this scenario. When the ego vehicle is between the RSU1 and the RSU4, it receives the LiDAR sensor data only from the RSU4 as shown by the red lines. The Next Unit of Computing (NUC) that directly connects to the LiDAR sensor in the RSU4 has to output the LiDAR sensor data from the two interfaces. In order to achieve this function, Open Virtual Switch (OVS) is installed in the NUC and duplicates the sensor data packets for multiple outputs.

After receiving multiple LiDAR sensor data, the ego vehicle has to enter the sensor data into Robot Operating System (ROS) for automated driving applications such as perception and navigation. Fig. 5.6 shows the interface between hardware and ROS applications. Basically, One LiDAR sensor needs one driver to use in ROS applications. When multiple LiDAR sensors are set as the default configuration and are connected to one device, running the same number of drivers is not enough. Using the default configuration leads to all data packets

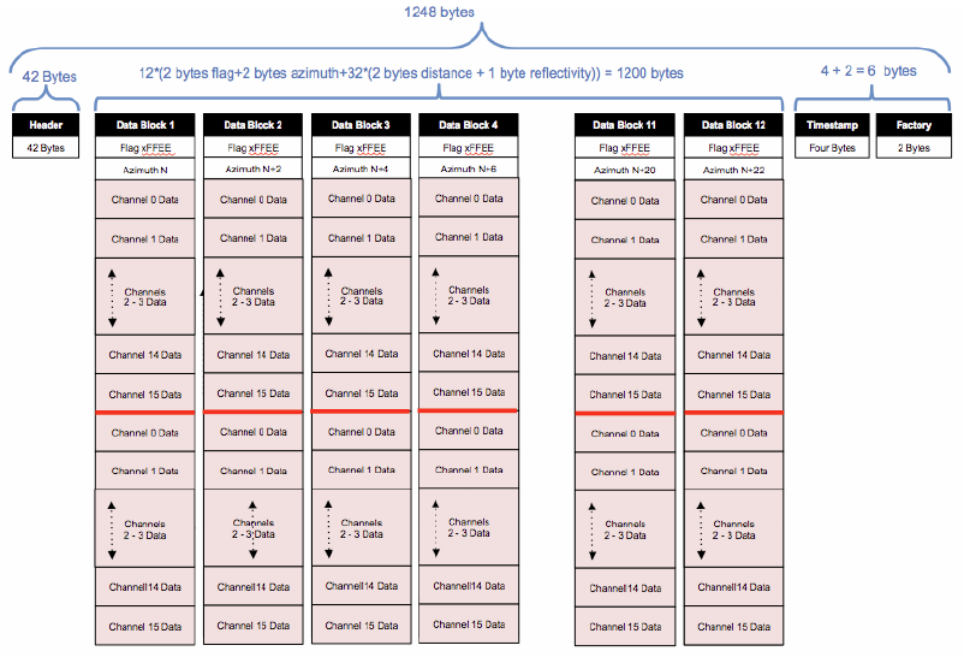

Figure 5.3: The structure of packets from a Velodyne LiDAR sensor cited from VLP-16 user manual.

(a) The first phase of the driving path and the communication links.

(b) The second phase of the driving path and the communication links.

Figure 5.4: The driving scenario of cooperative perception.

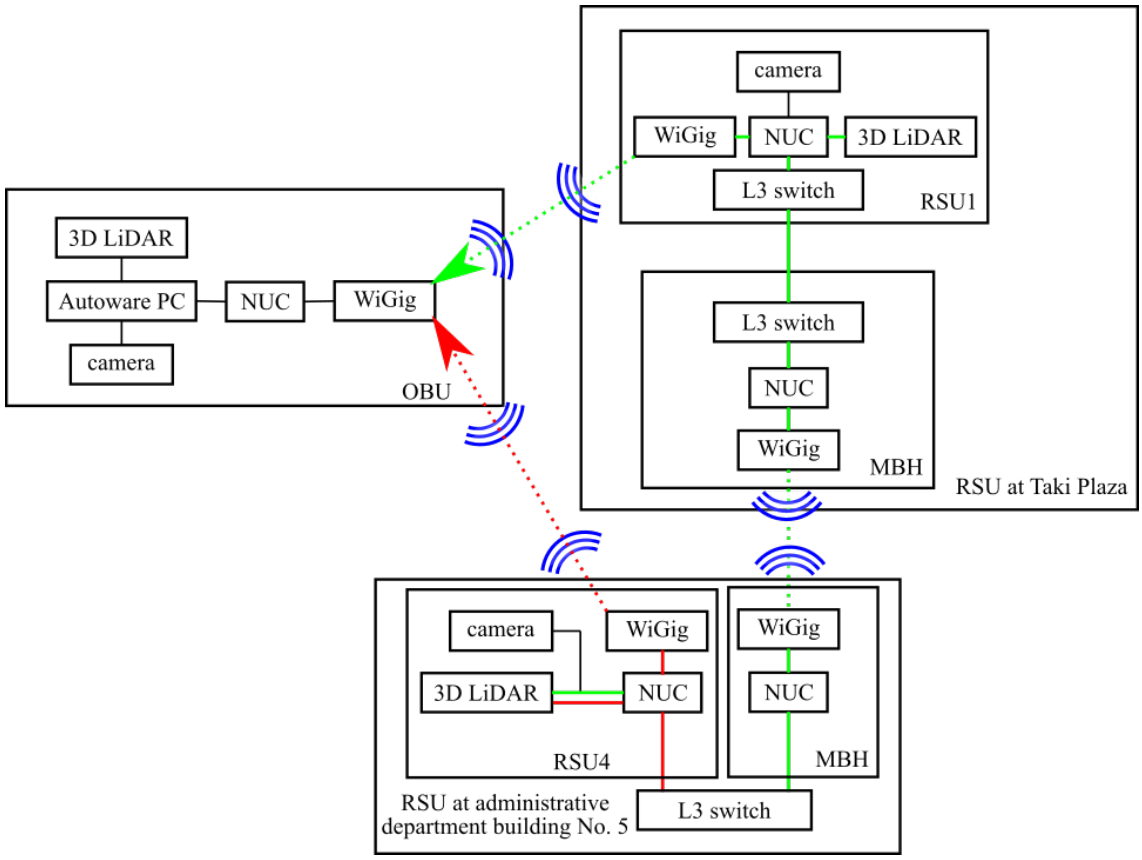

Figure 5.5: The network architecture used in the automated driving trial field.

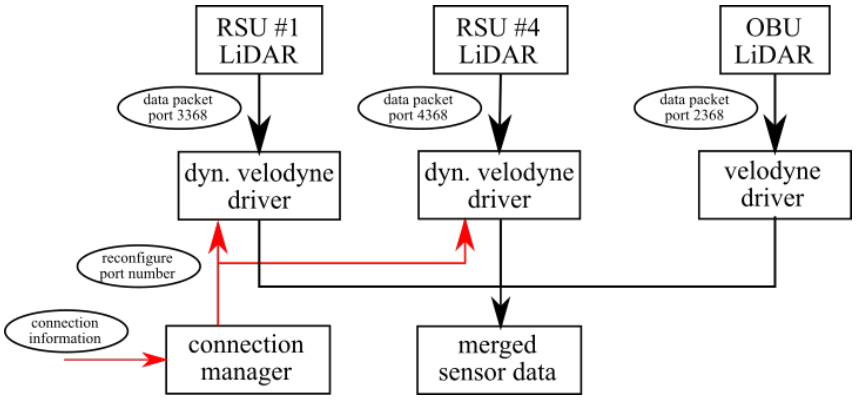

Figure 5.6: The interface between hardware and ROS applications.

with the same IP addresses and port numbers so that the drivers cannot identify each LiDAR sensor. Therefore, OVS in each NUC changes the IP addresses and the port numbers of the sensor data packets and the combination of the IP address and the port number is unique to each LiDAR sensor. On the other hand, the drivers specify the IP address and the port number by receiving reconfigure messages.

5.2 Results

Fig. 5.7 and Fig. 5.8 show the obtained sensor data in the ego vehicle and established connections. The ego vehicle has the color points and the infrastructures have green points. The white dotted lines show the established connections in each scene. Fig. 5.7 shows the scene where the ego vehicle approaches the RSU1. In this phase, the RSU4 sends its sensor data to the RSU1, and the RSU1 sends both its and obtained sensor data to the ego vehicle as shown in the white dotted lines. Fig. 5.8 shows the scene where the ego vehicle passes through the RSU1 and approaches the RSU4.

We measured the established connections in these scenes by using iperf3. The measurement is performed between the WiGig interfaces. When the ego vehicle starts to establish the connection, the ego vehicle has to turn right to approach the goal. This movement makes the received signal strength weak due to the strong directivity of the millimeter-wave antenna. Therefore, the average capacity during communicating with the RSU1 is from 1.8 Gbps to 2.1 Gbps. On the other hand, when the ego vehicle communicates with the RSU4, the direction to the RSU4 is stable so that the average capacity is about 2.1 Gbps. Considering that a Velodyne LiDAR sensor sends the sensor data at 754 packet/s $\times$ 1200 bytes $\simeq$ 7.2 Mbps, these capacities can send the sensor data within about 10 msec delay even if the RSU sends two sensor data, which can support automated driving systems processing at 100Hz.

Since the simulation has derived the required sensor data rate at the intersection in Fig. 4.11, it is possible to derive the driving speed that ensures safe automated driving. In Tokyo Institute of Technology campus Ookayama campus, it does not allow to drive at more than 20 km/h so that the driving speed of the ego vehicle is set to 20 km/h. The combination of the throughput measurement at 60 GHz and the fixed driving speed of the ego vehicle derives the maximum velocity of the target vehicle that the ego vehicle can avoid. Fig. 5.9 shows the areas that become targets of deriving the maximum velocity. This separation is based on which antenna the ego vehicle communicates with. From the Fig. 4.11, the ego vehicle can drive safely at 42-45 km/h (45 km/h) in the area1 (area2). This discussion shows that the ego vehicle can avoid a collision with a vehicle that exceeds about 25 km/h from the rule.

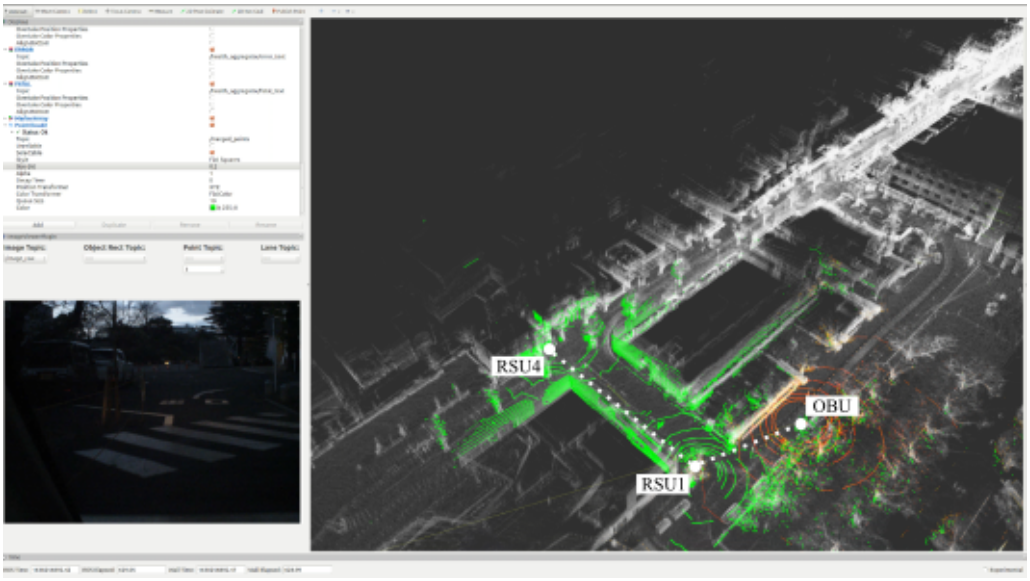

Figure 5.7: The scene where the ego vehicles drives between the RSU3 and the RSU1.

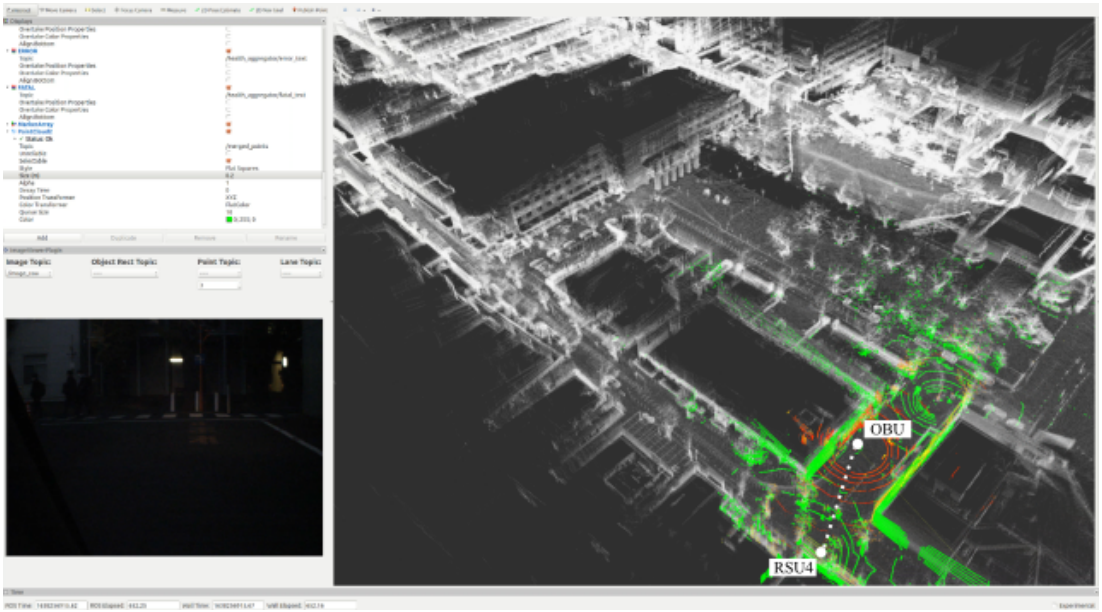

Figure 5.8: The scene where the ego vehicles drives between the RSU1 and the RSU4.

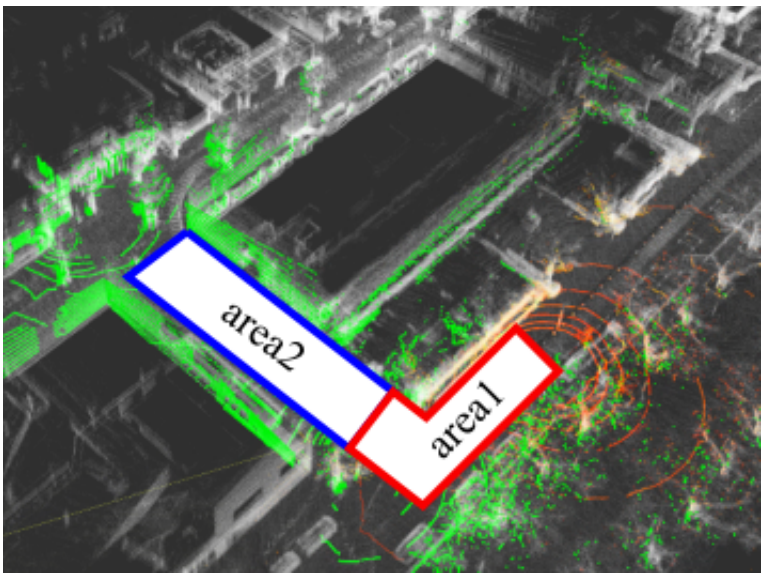

Figure 5.9: The areas separated by the established connections.

Chapter 6

Conclusion

This chapter concludes this thesis and presents future prospects. Chapter 2 shows the technologies that are used for cooperative perception. Moreover, the current status of cooperative perception for safe automated driving and the works about the requirements are also introduced. It shows that cooperative perception using processed sensor data is mainly analyzed due to using the current V2X communications as wireless interfaces. Although the works about cooperative perception using raw sensor data are less than using processed sensor data, its necessity is widely understood so that its use case is included in cooperative perception. The concept and the framework of safe automated driving are also introduced and they show that safety is mainly discussed from the viewpoint of vehicle control.

Chapters 3 and 4 tackle the goal of this thesis and derive the sensor data rate required for safe automated driving and the realized safe automated driving for each V2X communication system. The key points of this analysis are that both the vehicle behavior and the recognition process are comprehensively considered to derive realistic requirements, which is not achieved in the current research. Based on the traffic fatalities on two-lane roads that often occur and the expected vehicle behavior, chapter 3 particularly analyzes the overtaking scenario. This analysis fixes weather conditions and assumes no delay among the processes and no failure of automotive sensors and vehicle components. Since cooperative perception can be performed by sending raw sensor data from the blocking vehicle to the ego vehicle, whether the ego vehicle uses cooperative perception or not has an effect on the recognition process and the requirements. Firstly, the results show that, as the velocity becomes higher, the required sensor data rate increases drastically. In detail, the effect of considering the driving path becomes dominant at low velocity, and the comfortable braking becomes dominant at high velocity. Secondly, cooperative perception realized by the conventional and millimeter-wave communications is discussed. Techniques of cooperative perception using 30 and 60 GHz millimeter-wave communications make it possible to safely overtake at around 50 and 65 km/h under $d_{\mathrm{be}} = 10$ m due to the availability of sharing large sensor information. The derived requirements and the comparison will help to utilize cooperative perception using millimeter-wave communications in terms of improving safety and reducing the cost of installing automotive sensors on automated driving vehicles. Moreover, it will help to design the specification of V2X communication that considers how fast automated driving vehicles want to drive.

Chapter 4 changes the focus to intersections. From the statistics of traffic fatalities, pass-

ing through an unsignalized intersection is selected. This analysis also fixes weather conditions and assumes no delay among the processes and no failure of automotive sensors and vehicle components as the overtaking scenario. As vehicle behavior and recognition process are considered in the overtaking scenario, both factors are also considered in this scenario. Moreover, this scenario considers an additional factor that the ego vehicle decides whether braking has to be performed or not to reduce unnecessary braking and alleviate traffic congestion at the intersection. Firstly, the results show that as the velocity V_{t} becomes higher, the required sensor data rate also increases drastically under using CVFH. Secondly, it is shown that cooperative perception realized by 30 and 60 GHz millimeter-wave communications can support the safe crossing at 55 and 62 km/h while it is hard for the conventional 5 GHz communications to support sharing raw sensor data to realize the safe crossing. These results conclude that, considering the outage capacity, using 60 GHz for cooperative perception is a promising way to perform safe automated driving. These results will help to give great motivation to install millimeter-wave V2I communications to intersections so that automated driving vehicles do not have to drive too carefully and can improve safety.

Chapter 5 shows the demonstration of cooperative perception using millimeter-wave V2I communications. The vehicle drives through the RSU and receives multiple LiDAR sensor data via V2I millimeter-wave communications. Once the vehicle establishes a connection, obstacles in blind spots can be recognized by the vehicle. The combination with the results of chapter 4 shows that the vehicle that follows the rule can avoid a collision with a vehicle that exceeds 20 km/h from the maximum allowed velocity. These results will help to utilize millimeter-wave communications for avoiding collisions, which is hard for conventional V2X communications to do.

The end of this chapter discusses the extension to different scenarios and future works as future perspectives and finishes the thesis. Although these simulations assume very fundamental scenarios, they can be utilized for different foreseeable and preventable scenarios, and this topic is discussed from the macro perspective. The different cases can be divided into extending the traffic environment and considering more realistic conditions. In the case of extending traffic environment, since most traffic roads consist of intersections and straight roads and the above chapters analyze the driving scenarios that often cause traffic fatalities, these results can be used to estimate the required sensor data in a macro driving scenario. Realistic conditions relate to many disciplines such as wireless communications, traffic environment, vehicle behavior, and recognition process. Since our results are based on very basic scenarios, it is possible to compare these results and the results that consider more realistic conditions. This comparison will give us which condition is critical to the required sensor data rate and tell the priority of conditions. The cases other than foreseeable and preventable cases may need processes of other disciplines. The following bullets explain each case.

- Foreseeable and unpreventable cases
  These cases relate to a compromise to safety. Excessive safety will lead to a high charge to users and a high cost to manufacturers, and excessive safety is not equal to no traffic fatalities. Therefore, insurance for automated driving will be added to the simulations

- Unforeseeable and preventable cases

These cases have to be changed to foreseeable cases at the next time. Therefore, learning systems have to be added.

- Unforeseeable and unpreventable cases
  These cases are hard for automated driving vehicles to prevent traffic accidents by themselves. Therefore, these cases will also additionally consider insurance for automated driving vehicles.

Future works that should be prioritized from the micro perspective consist of two works. The first work is the sophistication of the requirements by considering the results of outdoor experiments. Using recognition packages in outdoor experiments will help to improve the derived requirements and can show the improvement of recognition rate due to cooperative perception. The second work relates to the wireless communication part. For example, the delay of transmitting sensor data is not considered for simplicity in this analysis, and multiple connections are not considered in the intersection scenario. A large delay will lead to a misalignment of the point clouds so that the recognition rate will get degraded. Multiple connections to a RSU will lead to allocating fewer radio resources to the ego vehicle than our intersection. These two works will help to get close to a realistic environment.

References

[1] S. Singh, "Critical Reasons for Crashes Investigated in the National Motor Vehicle Crash Causation Survey," National Highway Traffic Safety Administration, Rep. No. DOT HS 812 115, Feb. 2015.

[2] "Road safety white papaer in the 1st year of the Reiwa period," Cabient of office. Accessed: Nov. 22, 2021. [Online]. Available: https://www8.cao.go.jp/koutu/taisaku/r01kou_haku/index_zenbun_pdf.html

[3] "Road traffic injuries," World Health Organization, June 2021. Accessed: Nov. 22, 2021. [Online]. Available: https://www.who.int/news-room/fact-sheets/detail/road-traffic-injuries

[4] "Toward realization of connected car society," Ministry of Internal Affairs and Communications, July 2017. Accessed: Sept. 9, 2021. [Online]. Available: https://www.soumu.go.jp/main_content/000501374.pdf

[5] "Taxonomy and Definitions for Terms Related to Driving Automation Systems for On-Road Motor Vehicles," SAE J3016_201806, Apr. 2021.

[6] "Preparing for the Future of Transportation: Automated Vehicles 3.0," U.S. Department of Transportation, Oct. 2018.

[7] "TS 22.186: Technical Specification Group Services and System Aspects, Enhancement of 3GPP Support for V2X Scenarios, Stage1 (v16.2.0, Release 16)," 3GPP, 2019. Accessed: Mar. 18, 2021. [Online]. Available: https://portal.3gpp.org/desktopmodules/Specifications/SpecificationDetails.aspx?specificationId=3180

[8] "TR 103 562: Intelligent Transport Systems (ITS), Vehicular Communicatioins, Basic Set of Applications, Analysis of the Collective Perception Service (CPS) (v2.1.1 Release 2)," ETSI, 2019. Accessed: Mar. 18, 2021. [Online]. Available: https://www.etsi.org/deliver/etsi_tr/103500_103599/103562/02.01.01_60/tr_103562v020101p.pdf

[9] "TR 22.886: Technical Specification Group Services and System Aspects, Enhancement of 3GPP Support for 5G V2X Services (v16.2.0, Release 16)," 3GPP, 2018. Accessed: Mar. 18, 2021. [Online]. Available: https://portal.3gpp.org/desktopmodules/Specifications/SpecificationDetails.aspx?specificationId=3108

[10] "C-V2X Use Cases, Methodology, Examples and Service Level Requirements," 5GAA, June 2019. Accessed: Mar. 18. [Online]. Available: https://5gaa.org/wp-content/uploads/2019/07/5GAA_191906_WP_CV2X_UCs_v1-3-1.pdf

[11] "C-V2X Use Cases Volume (II): Examples and Service Level Requirements," 5GAA, Oct. 2020. Accessed: Mar. 18. [Online]. Available: https://5gaa.org/wp-content/uploads/2020/10/5GAA_White-Paper_C-V2X-Use-Cases-Volume-II.pdf

[12] M.H.C. Garcia, A. Molina-Galan, M. Boban, J. Gozalvez, B. Coll-Perales, T. Sahin, A. Kousaridas, "A Tutorial on 5G NR V2X Communications," IEEE Commun. Surv. Tutorial 2021, 2, 1978–1979, doi: 10.1109/COMST.2021.3057017.

[13] M. Shan, K. Narula, Y.F. Wong, S. Worrall, M. Khan, P. Alexander, E. Nebot, "Demonstrations of Cooperative Perception: Safety and Robustness in Connected and Automated Vehicle Operations." Sensors 2021, 21, 200, doi: 10.3390/s21010200.

[14] M. Tsukada, T. Oi, M. Kitazawa, H. Esaki, "Networked Roadside Perception Units for Autonomous Driving," Sensors 2020, 20, 5320, doi: 10.3390/s20185320.

[15] P. Dhawankar, P. Agrawal, B. Abderezzak, O. Kaiwartya, K. Busawon, M.S. Raboac, "Design and Numerical Implementation of V2X Control Architecture for Autonomous Driving Vehicles," Mathematics 2021, 9, 1696, doi: 10.3390/math9141696.

[16] S. Kim et al., "Cooperative perception for autonomous vehicle control on the road: Motivation and experimental results," 2013 IEEE/RSJ International Conference on Intelligent Robots and Systems, 2013, pp. 5059-5066, doi: 10.1109/IROS.2013.6697088.

[17] H. Qiu, F. Ahmad, F. Bai, M. Gruteser, R. Govindan, "AVR: Augmented Vehicular Reality," In Proceedings of the 16th Annual International Conference on Mobile Systems, Applications, and Services (MobiSys '18), Munich, Germany, June 2018, 10–15, pp. 8195, doi: 10.1145/3210240.3210319.

[18] Z. Li, T. Yu, R. Fukatsu, G.K. Tran, K. Sakaguchi, "Proof-of-Concept of a SDN Based mmWave V2X Network for Safe Automated Driving," In Proceedings of the 2019 IEEE Global Communications Conference (GLOBECOM), Waikoloa, HI, USA, 9–13 December 2019, 1–6, doi: 10.1109/GLOBECOM38437.2019.9014261.

[19] Z. Li, T. Yu, R. Fukatsu, G.K. Tran, K. Sakaguchi, "Towards Safe Automated Driving: Design of Software-Defined Dynamic MmWave V2X Networks and PoC Implementation," IEEE Open J. Veh. Technol., Jan. 2021, vol. 2, 78–93, doi: 10.1109/OJVT.2021.3049783.

[20] R. Fukatsu, K. Sakaguchi, "Automated Driving with Cooperative Perception Using Millimeter-Wave V2V Communications for Safe Overtaking," Sensors 2021, 21, 2659, doi 10.3390/s21082659.

[21] R. Fukatsu, K. Sakaguchi, "Automated Driving with Cooperative Perception Based on CVFH and Millimeter-Wave V2I Communications for Safe and Efficient Passing through Intersections," Sensors 2021, 21, 5854, doi 10.3390/s21175854.

[22] H. Shimada, A. Yamaguchi, H. Takada, and K. Sato, "Implementation and Evaluation of Local Dynamic Map in Safety Driving Systems," Journal of Transportation Technologies, Apr. 2015, 5, pp.102-112, doi: 10.4236/jtts.2015.52010.

[23] "TR 102 863; Intelligent Transport Systems (ITS); Vehicular Communicatioins; Basic Set of Applications; Local Dynamic Map (LDM); Rationale for and guidance on standardization (v1.1.1)," ETSI, June 2011.

[24] Yeong, De J., Gustavo Velasco-Hernandez, John Barry, and Joseph Walsh. 2021. "Sensor and Sensor Fusion Technology in Autonomous Vehicles: A Review," Sensors 21, no. 6, 2140, doi: 10.3390/s21062140.

[25] M. S. S. Kumar, K. S. Vimala and N. Avinash, "Face distance estimation from a monocular camera," 2013 IEEE International Conference on Image Processing, 2013, pp. 3532-3536, doi: 10.1109/ICIP.2013.6738729.

[26] H. Rashed et al., "Generalized Object Detection on Fisheye Cameras for Autonomous Driving: Dataset, Representations and Baseline," 2021 IEEE Winter Conference on Applications of Computer Vision (WACV), 2021, pp. 2271-2279, doi: 10.1109/WACV48630.2021.00232.

[27] B. Hadji, "Understanding wavelength choice in LiDAR systems," June 2015. Accessed: Sept. 7, 2021. [Online]. Available: https://www.embedded.com/understanding-wavelength-choice-in-lidar-systems/

[28] M. Kutila, P. Pyyknen, W. Ritter, O. Sawade, B. Schufele, "Automotive LIDAR sensor development scenarios for harsh weather conditions," 2016 IEEE 19th International Conference on Intelligent Transportation Systems (ITSC), 2016, pp. 265-270, doi: 10.1109/ITSC.2016.7795565.

[29] F. Roos, J. Bechter, C. Knill, B. Schweizer, C. Waldschmidt, "Radar Sensors for Autonomous Driving: Modulation Schemes and Interference Mitigation," in IEEE Microwave Magazine, Sept. 2019, vol. 20, no. 9, pp. 58-72, doi: 10.1109/MMM.2019.2922120.

[30] "Systems characteristics of automotive radars operating in the frequency band 76-81 GHz for intelligent transport systems application," ITU-R, M.2057, Jan. 2018.

[31] S. Heinrich, "Flash Memory in the emerging age of autonomy," Flash Mem. Summit 2017, 8, 1–10.

[32] R. Fukatsu, K. Sakaguchi, "Millimeter-Wave V2V Communications with Cooperative Perception for Automated Driving," 2019 IEEE 89th Vehicular Technology Conference (VTC2019-Spring), Apr. 2019, pp. 1-5, doi: 10.1109/VTCSpring.2019.8746344.

[33] R. Fukatsu, K. Sakaguchi, "Automated Driving with Cooperative Perception Using Millimeter-wave V2I Communications for Safe and Efficient Passing Through Intersections," In Proceedings of the 2021 IEEE 93rd Vehicular Technology Conference (VTC2021-Spring), Helsinki, Finland, 25–28 April 2021, pp. 1–5, doi: 10.1109/VTC2021-Spring51267.2021.9449017.

[34] "ETC handbook," ITS Technology Enhancement Association, Sept. 2018.

[35] "Usage situation and introduction effect of ETC," Ministry of Land Infrastructure Transport and Tourism. Accessed: Sept. 14, 2021. [Online]. Available: https://www.mlit.go.jp/road/ir/ir-council/pdf/7.pdf

[36] "Case studies of the effect of VICS," Ministry of Land Infrastructure Transport and Tourism. Accessed: Sept. 14, 2021. [Online]. Available: https://www.mlit.go.jp/road/ITS/j-html/ITSCaseStudies/ITSCaseStudies2007_j.pdf

[37] "Concept and Roadmap 2020 of Government and People ITS," Prime Minister of Japan and His Cabinet, IT Strategic Headquarters, Tokyo, Japan, June 2021.

[38] K. Abboud, H. A. Omar, W. Zhuang, "Interworking of DSRC and Cellular Network Technologies for V2X Communications: A Survey," in IEEE Transactions on Vehicular Technology, Dec. 2016, vol. 65, no. 12, pp. 9457-9470, doi: 10.1109/TVT.2016.2591558.

[39] R. Molina-Masegosa, J. Gozalvez, "LTE-V for Sidelink 5G V2X Vehicular Communications: A New 5G Technology for Short-Range Vehicle-to-Everything Communications," in IEEE Vehicular Technology Magazine, Dec. 2017, vol. 12, no. 4, pp. 30-39, doi: 10.1109/MVT.2017.2752798.

[40] K. Kiela, V. Barzdenas, M. Jurgo, V. Macaitis, J. Rafanavicius, A. Vasjanov, L. Kladovscikov, R. Navickas, "Review of V2XIoT Standards and Frameworks for ITS Applications," Appl. Sci. 2020, 10, 4314, doi: 10.3390/app10124314.

[41] G. Naik, B. Choudhury, J. Park, "IEEE 802.11bd & 5G NR V2X: Evolution of Radio Access Technologies for V2X Communications," in IEEE Access, 2019, vol. 7, pp. 70169-70184, doi: 10.1109/ACCESS.2019.2919489.

[42] "TS 36.213: Technical Specification Group Radio Access Network; Evolved Universal Terrestrial Radio Access (E-UTRA); Physical layer procedures (v16.0.0, Release 16)," 3GPP, Dec. 2019.

[43] A. Bazzi, B. M. Masini, A. Zanella, I. Thibault, "On the Performance of IEEE 802.11p and LTE-V2V for the Cooperative Awareness of Connected Vehicles," in IEEE Transactions on Vehicular Technology, Nov. 2017, vol. 66, no. 11, pp. 10419-10432, doi: 10.1109/TVT.2017.2750803.

[44] R. Molina-Masegosa, J. Gozalvez, "LTE-V for Sidelink 5G V2X Vehicular Communications: A New 5G Technology for Short-Range Vehicle-to-Everything Communications," in IEEE Vehicular Technology Magazine, Dec. 2017, vol. 12, no. 4, pp. 30-39, doi: 10.1109/MVT.2017.2752798.

[45] M. Shi, C. Lu, Y. Zhang and D. Yao, "DSRC and LTE-V communication performance evaluation and improvement based on typical V2X application at intersection," 2017 Chinese Automation Congress (CAC), 2017, pp. 556-561, doi: 10.1109/CAC.2017.8242830.

[46] H. Z. B. Sun, "IEEE 802.11-18/0861r9: 802.11 NGV proposed PAR," presented at the IEEE 802.11 NGV Meeting, Nov. 2019.

[47] W. Anwar, A. Tral, N. Franchi, G. Fettweis, "On the Reliability of NR-V2X and IEEE 802.11bd," 2019 IEEE 30th Annual International Symposium on Personal, Indoor and Mobile Radio Communications (PIMRC), 2019, pp. 1-7, doi: 10.1109/PIMRC.2019.8904104.

[48] "Summary of Coexistence Aspects in NR-V2X Study," document R1- 1812000, 3GPP TSG RAN WG1 94b, Qualcomm Inc., Chengdu, China, 2018.

[49] "Traffic Fatalities and Enforcing Road Traffic Law Situation in 30th Years of The Heisei Period," National Police Agency Traffic Bureau, Feb. 2019.

[50] "About Intersection Safety," U.S. Department of Transportation Federal Highway Administration, Mar. 2021. Accessed: Nov. 1, 2021. [Online]. Available: https://safety.fhwa.dot.gov/intersection/about/

[51] M. Wisch et al., "Car-to-car accidents at intersections in Europe and identification of Use Cases for the test and assessment of respective active vehicle safety systems," 26th International Technical Conference on the Enhanced Safety of Vehicles (ESV): Enabling a Safer Tomorrow, June 2019.

[52] R. Lohmann, S. van der Zwaan, "Regulations required: safety drives autonomous vehicles market. ," A 2getthere white paper, 2018. Accessed: Nov. 1, 2021. [Online]. Available: http://www.advancedtransit.org/wp-content/uploads/2018/04/2getthere-whitepaper-Regulations-Required-Safety-drives-\autonomous-vehicles-market.pdf

[53] "ASSESSING RISK AND SETTING TARGETS IN TRANSPORT SAFETY PROGRAMMES," European Transport Safety Council, 2003.

[54] "SAFETY FIRST FOR AUTOMATED DRIVING," Daimler, July 2019. Accessed: Nov. 5, 2021. [Online]. Available: https://www.daimler.com/documents/innovation/other/safety-first-for-automated-driving.pdf

[55] "ETHICS COMMISSION AUTOMATED AND CONNECTED DRIVING," Federal Ministry of Transport and Digital Infrastructure, June 2017. Accessed: Nov. 5, 2021. [Online]. Available: https://www.bmvi.de/SharedDocs/EN/publications/report-ethics-commission.pdf?__blob=publicationFile

[56] "Automated Driving Safety Evaluation Framework Ver.1.0," Japan Mobile Manufacturers Association Inc., AD Safety Assurance Expert Group, Oct. 2020.

[57] "Revised Framework document on automated/autonomous vehicles," Economic Commission for Europe, Inland Transport Committee, World Forum for Harmonization of Vehicle Regulations 178th session, Sept. 2019. Accessed: Nov. 7, 2021. [Online]. Available: https://unece.org/DAM/trans/doc/2019/wp29/ECE-TRANS-WP29-2019-34-rev.1e.pdf

[58] E. Thorn, S. Kimmel, M. Chaka, "A Framework for Automated Driving System Testable Cases and Scenarios," NHTSA, DOT HS 812 623, Sep. 2018.

[59] S. Dimce, M. S. Amjad, F. Dressler, "mmWave on the Road: Investigating the Weather Impact on 60 GHz V2X Communication Channels," 2021 16th Annual Conference on Wireless On-demand Network Systems and Services Conference (WONS), 2021, pp. 1-8, doi: 10.23919/WONS51326.2021.9415572.

[60] E. Arnold, O. Y. Al-Jarrah, M. Dianati, S. Fallah, D. Oxtoby and A. Mouzakitis, "A Survey on 3D Object Detection Methods for Autonomous Driving Applications," in IEEE Transactions on Intelligent Transportation Systems, Oct. 2019, vol. 20, no. 10, pp. 3782-3795, doi: 10.1109/TITS.2019.2892405.

[61] D. Dai, Z. Chen, P. Bao, J. Wang, "A Review of 3D Object Detection for Autonomous Driving of Electric Vehicles," World Electr. Veh. J., Aug. 2021, 12, 139, doi: 10.3390/wevj12030139.

[62] X. Chen, H. Ma, J. Wan, B. Li, T. Xia, "Multi-view 3D Object Detection Network for Autonomous Driving," 2017 IEEE Conference on Computer Vision and Pattern Recognition (CVPR), 2017, pp. 6526-6534, doi: 10.1109/CVPR.2017.691.

[63] K. Żywanowski, A. Banaszczyk, M. R. Nowicki, "Comparison of camera-based and 3D LiDAR-based place recognition across weather conditions," 2020 16th International Conference on Control, Automation, Robotics and Vision (ICARCV), 2020, pp. 886-891, doi: 10.1109/ICARCV50220.2020.9305429.

[64] E. E. Aksoy, S. Baci and S. Cavdar, "SalsaNet: Fast Road and Vehicle Segmentation in LiDAR Point Clouds for Autonomous Driving," 2020 IEEE Intelligent Vehicles Symposium (IV), Oct. 2020, pp. 926-932, doi: 10.1109/IV47402.2020.9304694.

[65] X. Xie, L. Bai, X. Huang, "Real-Time LiDAR Point Cloud Semantic Segmentation for Autonomous Driving," Electronics 11, Nov. 2022, doi: 10.3390/electronics11010011.

[66] S. Chen, D. Tian, C. Feng, A. Vetro and J. Kovačevič, "Fast Resampling of Three-Dimensional Point Clouds via Graphs," in IEEE Transactions on Signal Processing, Feb. 2018, vol. 66, no. 3, pp. 666-681, doi: 10.1109/TSP.2017.2771730.

[67] "Safety Technology Guideline for Automated Driving," Ministry of Land Infrastructure Transport and Tourism, Sept. 2018.

[68] P. Greibe, "Braking Distance, Friction and Behaviour," Trafitec, Scion-DTU, July 2007, pp. 6-8.

[69] "Policy on Geometric Design of Highways and Streets," American Association of State Highway and Transportation Officials, Washington, 2001, pp. 110-111.

[70] G. Johansson, K. Rumar, "Drivers' Brake Reaction Times," Human Factors, Feb. 1971, vol. 13, no. 1, doi: 10.1177/001872087101300104.

[71] "Report of the Massachusetts Highway Accident Survey," Massachusetts Institute of Technology, CWA and ERA project, Cambridge, Mass.: Massachusetts Institute of Technology, 1935.

[72] O.K. Norman, "Braking Distances of Vehicles from High Speeds," Proceedings HRB, Highway Research Board, 1953, vol. 32, pp. 421-436.

[73] "Road design standards," Ministry of Land Infrastructure Transport and Tourism. Accessed: Nov. 14, 2021. [Online]. Available: https://www.mlit.go.jp/road/sign/pdf/kouzourei_full.pdf

[74] W. Ben-Messaoud, M. Basset, J. Lauffenburger, R. Orjuela, "Smooth Obstacle Avoidance Path Planning for Autonomous Vehicles," IEEE International Conference on Vehicular Electronics and Safety (ICVES), Madrid, Sept. 2018, pp. 1-6, doi: 10.1109/ICVES.2018.8519525.

[75] D. Bazazian, J. R. Casas, J. Ruiz-Hidalgo, "Fast and Robust Edge Extraction in Unorganized Point Clouds," 2015 International Conference on Digital Image Computing: Techniques and Applications (DICTA), Adelaide, SA, Nov. 2015, pp. 1-8, doi: 10.1109/DICTA.2015.7371262.

[76] J. Karedal, N. Czink, A. Paier, F. Tufvesson, A. F. Molisch, "Path Loss Modeling for Vehicle-to-Vehicle Communications," in IEEE Transactions on Vehicular Technology, Jan. 2011, vol. 60, no. 1, pp. 323-328, doi: 10.1109/TVT.2010.2094632.

[77] A. Kato, K. Sato, M. Fujise, S. Kawakami, "Propagation Characteristics of 60GHz Millimeter Waves for ITS Inter-Vehicle Communications," IEICE Transactions on Communications, Sept. 2001, vol. E84B, no.9, pp.2530-2539, NAID: 110003219226.

[78] S. Oh, S. Kaul, M. Gruteser, "Exploiting vertical diversity in vehicular channel environments," 2009 IEEE 20th International Symposium on Personal, Indoor and Mobile Radio Communications, Sept. 2009, Tokyo, pp. 958-962, doi: 10.1109/PIMRC.2009.5449728.

[79] O. Andrisano, M. Chiani, M. Frullone, C. Moss, V. Tralli, "Propagation effects and countermeasures analysis in vehicle-to-vehicle communication at millimeter waves," [1992 Proceedings] Vehicular Technology Society 42nd VTS Conference - Frontiers of Technology, May 1992, vol. 1, pp. 312-316, doi: 10.1109/VETEC.1992.245415.

[80] Y. Karasawa, "Multipath fading due to road surface reflection and fading reduction by mean of space diversity in ITS vehicle-to- vehicle communications at 60 GHz," IEICE Trans. Commun., 2000, Vol.J83-B, No.4, pp.518-524, doi: 10.1002/ecja.1065.

[81] A. N. Uwaechia, N. M. Mahyuddin, "A Comprehensive Survey on Millimeter Wave Communications for Fifth-Generation Wireless Networks: Feasibility and Challenges," in IEEE Access, Mar. 2020, vol. 8, pp. 62367-62414, doi: 10.1109/ACCESS.2020.2984204.

[82] "Transportation Census in 27th Years of The Heisei Period," Ministry of Land Infrastructure Transport and Tourism, June 2017. Accessed: Nov. 15, 2021. [Online]. Available: https://www.mlit.go.jp/road/census/h27/

[83] M. Khayatian, M. Mehrabian, E. Andert, R. Dedinsky, S. Choudhary, Y. Lou, A. Shirvastava, "A Survey on Intersection Management of Connected Autonomous Vehicles," ACM Trans. Cyber-Phys. Syst. 4, Aug. 2020, 4, Article 48, 27 pages, doi: 10.1145/3407903.

[84] J. Zhang, W. Xiao, B. Coifman, J. P. Mills, "Vehicle Tracking and Speed Estimation From Roadside Lidar," in IEEE Journal of Selected Topics in Applied Earth Observations and Remote Sensing, Sept. 2020, vol. 13, pp. 5597-5608, doi: 10.1109/JSTARS.2020.3024921.

[85] P. Lin, J. Liu, P. J. Jin, B. Ran, "Autonomous Vehicle-Intersection Coordination Method in a Connected Vehicle Environment," in IEEE Intelligent Transportation Systems Magazine, Oct. 2017, vol. 9, no. 4, pp. 37-47, doi: 10.1109/MITS.2017.2743167.

[86] D. Kye, S. Kim, S. Seo, "Decision making for automated driving at unsignalized intersection," 2015 15th International Conference on Control, Automation and Systems (ICCAS), Dec. 2015, pp. 522-525, doi: 10.1109/ICCAS.2015.7364974.

[87] V. Sezer, T. Bandyopadhyay, D. Rus, E. Frazzoli, D. Hsu, "Towards autonomous navigation of unsignalized intersections under uncertainty of human driver intent," 2015 IEEE/RSJ International Conference on Intelligent Robots and Systems (IROS), Sept. 2015, pp. 3578-3585, doi: 10.1109/IROS.2015.7353877.

[88] R. B. Rusu, S. Cousins, “3D is here: Point Cloud Library (PCL),” 2011 IEEE International Conference on Robotics and Automation, Shanghai, China, May 2011, pp. 1-4, doi: 10.1109/ICRA.2011.5980567.

[89] A. Aldoma et al., “CAD-model recognition and 6DOF pose estimation using 3D cues,” 2011 IEEE International Conference on Computer Vision Workshops (ICCV Workshops), Barcelona, Spain, Nov. 2011, pp. 585-592, doi: 10.1109/ICCVW.2011.6130296.

[90] “TR 103 257-1; Intelligent Transport Systems (ITS); Access Layer; Part 1: Channel Models for the 5,9 GHz frequency band (v1.1.1),” ETSI, May 2019.

[91] B. Aygun, M. Boban, J. P. Vilela A. M. Wyglinski, “Geometry-Based Propagation Modeling and Simulation of Vehicle-to-Infrastructure Links,” 2016 IEEE 83rd Vehicular Technology Conference (VTC Spring), May 2016, pp. 1-5, doi: 10.1109/VTCSpring.2016.7504262.

[92] S. Schwarz, E. Zchmann, M. Mller, K. Guan, “Dependability of Directional Millimeter Wave Vehicle-to-Infrastructure Communications,” in IEEE Access, Mar. 2020, vol. 8, pp. 53162-53171, doi: 10.1109/ACCESS.2020.2981166.

[93] I. A. Hemadeh, K. Satyanarayana, M. El-Hajjar, L. Hanzo, “Millimeter-Wave Communications: Physical Channel Models, Design Considerations, Antenna Constructions, and Link-Budget,” in IEEE Communications Surveys & Tutorials, Dec. 2018, vol. 20, no. 2, pp. 870-913, doi: 10.1109/COMST.2017.2783541.

Acknowledgments

I would like to acknowledge and give my warmest thanks to my supervisor Kei Sakaguchi who made this work possible. His guidance and advice carried me through all the stages of writing my project. I would also like to thank my committee members for letting my defense be an enjoyable moment, and for your brilliant comments and suggestions, thanks to you. I would also like to give special thanks to my family as a whole for their continuous support and understanding when undertaking my research and writing my project.